ENHANCED INTERPRETATION MODELS FOR IMPEDANCE OF LITHIUM ION BATTERIES

By

NELLIANN PEREZ-GARCIA

A DISSERTATION PRESENTED TO THE GRADUATE SCHOOL
OF THE UNIVERSITY OF FLORIDA IN PARTIAL FULFILLMENT
OF THE REQUIREMENTS FOR THE DEGREE OF
DOCTOR OF PHILOSOPHY

UNIVERSITY OF FLORIDA

2006

I dedicate this work to my grandparents. These people are my heroes and I feel very proud to be part of their family.

ACKNOWLEDGMENTS

The author wishes to express her sincere gratitude and appreciation to various individuals who helped in the development of this work. To my advisor, Dr. Mark E. Orazem, goes my appreciation for his guidance, patience, and discussions related to the analysis of this work. I am very grateful that he believed in me and gave me the opportunity to develop my experimentation and modeling skills. I thanks my committee and group members for all their help and input in the development of this work. Special thanks go to Vicky Huang and Shirley Kelly for all their support.

Also I wish to acknowledge the University of Florida Graduate Minority Fellowship and the National Aeronautics and Space Administration (NASA) for funding this project. Special thanks go to William Bennett, Michelle Manzo, and Marla Perez-Davis for all their help in this project.

Finally, and most important, I would like to thank my parents, Oscar and Carmen, for all the sacrifices they made to support me in this project; and my sister, Maricarmen, for motivating me along this journey. I would like to thank my husband, Jose, for his support and love. These people gave me the courage to pursue my dreams, and I am always going to be grateful for having them by my side.

TABLE OF CONTENTS

page

ACKNOWLEDGMENTS iii

LIST OF TABLES vi

LIST OF FIGURES viii

ABSTRACT xiii

CHAPTER

1 INTRODUCTION 1

2 CHARACTERISTICS OF LITHIUM–BASED BATTERIES 3

2.1 History of Batteries 3
2.2 Characteristics of Lithium-Based Batteries 5
2.2.1 Anode Materials 7
2.2.2 Cathode Materials 8
2.2.3 Electrolyte 9
2.2.4 Electrode–Electrolyte Interface 12

3 ELECTROCHEMICAL IMPEDANCE SPECTROSCOPY THEORY . . 15

3.1 Impedance Response of Electrical Circuits 16
3.2 Experimental Considerations 17
3.3 Error Structure 19
3.3.1 Kramers–Kronig Relations 19
3.3.2 Measurement Model Approach 19
3.4 Impedance Spectroscopy Data Analysis 20
3.5 Impedance Response Models 23

4 EXPERIMENTAL DESIGN AND ERROR ANALYSIS 26

4.1 Experimental System 26
4.2 Experiment Design 29
4.3 Measurement Model Analysis 30
4.3.1 Steady State Experiments at Constant Temperature 31
4.3.2 Steady State Experiments at Increasing Temperatures . . . 33
4.3.3 Transient Experiments at Constant Temperature 37
4.3.4 Blocking Electrodes 38

5 EXPERIMENTAL RESULTS AND PRELIMINARY ANALYSIS 40

5.1 Steady State Experiments at Constant Temperature 41
5.2 Steady State Experiments at Increasing Temperatures 44
5.3 Transient Experiments at Constant Temperature 49
5.4 Conclusions 54

6 BLOCKING ELECTRODE ANALYSIS 57

6.1 Experimental Results 57
6.2 Graphical Analysis 57
6.3 Comparison to Disk Electrode 61
6.4 Conclusions 63

7 MODEL DEVELOPMENT 64

7.1 Chemistry 64
7.2 Physics 67
7.3 Model Development 69
7.3.1 Steady State 74
7.3.2 Sinusoidal Steady State 75
7.3.3 Mass Transfer 76
7.3.4 Impedance Expressions 79
7.4 Results 80
7.5 Conclusions 85

8 CONCLUSIONS 86

8.1 Experiments 86
8.2 Model 87

REFERENCES 88

BIOGRAPHICAL SKETCH 94

LIST OF TABLES

Table page

2–1 Chemical composition of passivation films formed on lithium metal surface in contact with different electrolytes. 13

2–2 Chemical composition of passivation films on the Li metal in contact with additives used to enhance the cycling efficiency. 14

4–1 Summary of the experimental design. The number of sequential measurements is presented. 30

4–2 Error structure models determined for Cell UF-CTe. This cell was exposed to a temperature range varying from 60°C to 85°C. 35

4–3 Error structure models determined for Cell NA–AB. This cell was exposed to a temperature range varying from 80°C to 100°C at 10°C intervals. 39

5–1 Average α values obtained using graphical techniques at the intermediate frequency range for Cell NA–ATi through NA–DTi. Six replicates were used to calculate the average parameters 44

5–2 Average values of the parameters obtained using graphical techniques at the high frequency range for Cell NA–ATi trough NA–DTi. Six replicates were used to calculate the average parameters 44

5–3 Average values of the low frequency tail slopes from cells UF–BTe, UF–CTe, and UF–FTe. Six replicates were used to calculate the average parameters. 46

5–4 Slopes obtained using graphical techniques at the intermediate frequency range from cells UF–BTe, UF–CTe, and UF–FTe. Six replicates were used to calculate the average parameters 47

5–5 Average values of the parameters obtained using graphical techniques at the high frequency range from cells UF–BTe, UF–CTe, and UF–FTe. Six replicates were used to calculate the average parameters . 50

5–6 Values of the low frequency tail slopes from Cell UF–DTr and UF–ETr. 53

5–7 Values of the low and intermediate frequency tail slopes obtained from Cell UF–DTr and UF–ETr. 53

5–8 Average values of the parameters obtained using graphical techniques at the high frequency range for Cell UF–DTr. 55

6–1 Parameter values extracted from Figures 6–2 and 6–3 for Cell NA-BB. 61

7–1 Reaction mechanisms of common lithium battery contaminants. Water was the only contaminant considered in this work. 65

7–2 Summary of the parameters used to calculate the impedance response of the models presented in Section 7. 81

LIST OF FIGURES

Figure page

2–1 Schematic of the "artificial electrical organ" or the "Pile" developed by Alessandro Volta in 1799. 4

2–2 Schematic of a rechargeable lithium battery. 6

2–3 Schematic representation of the lithium–polymer electrolyte interphase.(a) Overall interphase (b) Small segment of the interphase. . 13

3–1 Passive elements that serve as a component for an electrical circuit. . 16

3–2 Small signal analysis of an electrochemical non–linear system. 18

3–3 Electrode configuration in an electrochemical cell. 18

3–4 Impedance–plane or Nyquist representation of impedance data for Cell NA–ATi. The open symbols represent measurements taken 15 hour after the cell preparation. The half–full symbols represent measurements taken approximately 48 hours after the cell preparation. 21

3–5 Schematic representation of a simple reactive system. 21

3–6 Bode representation of impedance data, magnitude and phase angle, for Cell NA–ATi, respectively. The open symbols represent measurements taken 15 hour after the cell preparation. The half–full symbols represent measurements taken approximately 48 hours after the cell preparation. 22

3–7 Plots of the real and imaginary part of the impedance as a function of frequency for Cell NA–ATi. The open symbols represent measurements taken 15 hour after the cell preparation. The half–full symbols represent measurements taken approximately 48 hours after the cell preparation. 22

4–1 Schematic of the cell sandwich. The cell was build using a thin, insulating mask to separate the electrodes. The mask was intended to prevent short circuit. 27

4–2 Schematic of the experimental setup used for the electrochemical impedance tests. 28

4–3 Schematic representation of a Voigt circuit used as a measurement model. 31

4–4 Measurement model prediction of impedance data for Cell NA–ATi. The open symbols represent measurements taken 15 hours after their preparation. The half-full symbols represent measurements taken approximately 48 hours after the cell preparation. The solid line represents the measurement model fit. 32

4–5 Error structure for Cell NA–ATi measurements taken 15 and 48 hours after their preparation, respectively. The open symbols represent the real part of the impedance. The half-full symbols represent imaginary part of the impedance. The solid line represents the error structure model fit. 33

4–6 Measurement model fit of the imaginary part of the impedance data for Cell NA–ATi. The open symbols represent measurements taken 15 hours after their preparation. The half-full symbols represent measurements taken approximately 48 hours after the cell preparation. The solid line represents the measurement model fit and the dashed lines represent the 95.4% confidence interval. 34

4–7 Measurement model prediction of the real part of the impedance data for Cell NA–ATi. The open symbols represent measurements taken 15 hours after their preparation. The half-full symbols represent measurements taken approximately 48 hours after the cell preparation. The solid line represents the measurement model prediction and the dashed lines represent the 95.4% confidence interval. 35

4–8 Error structure for Cell UF–CTe measurements (a)60°C (b)65°C (c)70°C (d)75°C (e)80°C (f)85°C. The open symbols represent the real part of the impedance. The half-full symbols represent imaginary part of the impedance. The solid line represents the error structure model fit. 36

4–9 Error structure for Cell NA–ATi measurements taken 15 and 48 hours after their preparation, respectively. The open symbols represent the real part of the impedance. The half-full symbols represent imaginary part of the impedance. The solid line represents the error structure model fit. 37

4–10 Error structure for Cell NA–AB measurements (a)80°C (b)90°C (c)100°C. The open symbols represent the real part of the impedance. The half-full symbols represent imaginary part of the impedance. The solid line represents the error structure model fit. 38

5–1 Equivalent circuit model used to fit the impedance data obtained from the Li|PEO-LiTFSI system. Figure reproduced from: R. Bouchet, S. Lascaud, and M. Rosso. An EIS Study of the Anode Li|PEO-LiTFSI of a Li Polymer Battery. Journal of Electrochemical Society. Vol. 150, No. 10, pp.A1385–A1389, 2003. 40

5–2 Effective CPE coefficient defined by equation (5.1) for Cell NA–ATi. The open symbols represent measurements taken approximately 15 hours after the cell preparation. The half–full symbols represent measurements taken approximately 48 hours after the cell preparation. 42

5–3 IR-corrected Bode plots for Cell NA–ATi; a) phase angle, b) modulus. The open symbols represent measurements taken approximately 15 hours after the cell preparation. The half–full symbols represent measurements taken approximately 48 hours after the cell preparation. 43

5–4 Impedance-plane or Nyquist representation of impedance data for Cell UF–CTe with temperature as a parameter. Six replicates of each measurement are presented for each temperature. 45

5–5 Bode Representation of impedance data for phase angle and magnitude for Cell UF–CTe, respectively, with temperature as a parameter. Six replicates of each measurement are presented for each temperature. 45

5–6 Plots of the imaginary and real part of the impedance as functions of frequency for Cell UF–CTe with temperature as a parameter. Six replicates of each measurement are presented for each temperature. 46

5–7 Average values of the low frequency tail slopes from cells UF–BTe, UF–CTe, and UF–FTe. Six replicates were used to calculate the average parameters. 47

5–8 Average values of the intermediate frequency tail slopes from cells UF–BTe, UF–CTe, and UF–FTe. Six replicates were used to calculate the average parameters. 48

5–9 Average values of the high frequency tail slopes from cells UF–BTe, UF–CTe, and UF–FTe. Six replicates were used to calculate the average parameters. 48

5–10 Effective CPE coefficient defined by equation (5.1) for Cell UF–CTe. Six replicates of each measurement are presented for each temperature. 49

5–11 IR-corrected Bode plots for Cell UF–CTe; (a) phase angle, (b) modulus. Six replicates of each measurement are presented for each temperature. 50

5–12 Impedance-plane or Nyquist representation of impedance data for Cell UF–DTr with temperature as a parameter. Impedance spectra were taken every 30 seconds for 48 hours, it took approximately two hours to complete one spectrum. 51

5–13 Bode Representation of impedance data for phase angle and magnitude for Cell UF–DTr, respectively. Impedance spectra were taken every 30 seconds for 48 hours, it took approximately two hours to complete one spectrum. 51

5–14 Plots of the imaginary and real part of the impedance as functions of frequency for Cell UF–DTr. Impedance spectra were taken every 30 seconds for 48 hours, it took approximately two hours to complete one spectrum. 52

5–15 Effective CPE coefficient defined by equation (5.1) for Cell UF–DTr. . 54

5–16 IR-corrected Bode plots for Cell UF–DTr; a) phase angle, b) modulus. 56

6–1 Complex impedance plane or Nyquist representation for the response of a 430 Stainless Steel disk in PEO/LiTSFI electrolyte with concentration as a parameter. Six replicates of each measurement are presented for each temperature. 58

6–2 Plots of the imaginary and real part of the impedance as functions of frequency for Cell NA-BB with temperature as a parameter. Six replicates of each measurement are presented for each temperature. 59

6–3 Effective CPE coefficient defined by equation (6.3) for Cell NA-BB. Six replicates of each measurement are presented for each temperature. 60

6–4 Dimensionless analysis for the impedance response of a stainless steel disk in PEO/LiTFSI electrolytes with temperature as a parameter. 62

6–5 Dimensionless imaginary part of the impedance as a function of dimensionless frequency for a disk electrode with local capacitance dispersion. 62

7–1 Impedance-plane or Nyquist representation of impedance data for Cell UF-DTr. Very large impedance at low frequencies can be observed suggesting that a disconnection of the system which may be attributed to gas evolution. 66

7–2 Cell UF-ATe lithium electrode surface. The surface of the electrode was almost completely covered with a white to blue oxide layer. . . 67

7–3 Cell UF-BTe lithium electrode surface. The edges of the electrode were covered with a white to blue oxide layer, while the inner surface kept a much brighter metallic lustre. 68

7–4 Scanning electron micrographs of Cell UF-ATe lithium electrode surface. (a) Magnification = 35. (b) Magnification = 200. 70

7–5 Scanning electron micrographs of Cell UF-BTe lithium electrode surface. Magnification = 350. 71

7–6 Commercial lithium foil native layer composition. 71

7–7 Schematic of the simplified system. Two surfaces were identified in which the reactions take place. The lithium oxidation/reduction reaction take place at the lithium metal surface and the LiOH and Li_2O formation reactions take place in the oxide layer surface. . . . 72

7–8 Schematic of the simplified system. Two surfaces were identified in which the reactions take place. The lithium oxidation/reduction reaction take place at the lithium metal surface only, but the LiOH and Li_2O formation reactions can take place in both the lithium metal surface and the oxide layer surface. 73

7–9 Impedance–plane or Nyquist representation of impedance data of a symmetric cell. (a) Experimental Result. (b) Model 1. (c) Model 2. 82

7–10 Imaginary plots of impedance data of a symmetric cell. (a) Experimental Result. (b) Model 1. (c) Model 2. 83

7–11 Imaginary representation of impedance data of a symmetric cell. (a) Experimental Result. (b) Model 1. (c) Model 2. 84

Abstract of Dissertation Presented to the Graduate School
of the University of Florida in Partial Fulfillment of the
Requirements for the Degree of Doctor of Philosophy

ENHANCED INTERPRETATION MODELS FOR IMPEDANCE OF LITHIUM ION BATTERIES

By

Nelliann Perez-Garcia

May 2006

Chair: Mark E. Orazem
Major Department: Chemical Engineering

Electrochemical impedance spectroscopy experiments and models were used to facilitate an in-depth understanding of the physical processes that control symmetric lithium coin cells. The experimental component was intended to obtain good quality data to guide in the model development. The quality of the results obtained were tested using the measurement model approach developed in our group.

Experiments performed on symmetric lithium coin cells, with time and temperature as the tested variables, showed that more than one time constant can be identified in the system. The decrease of the impedance response with time is consistent with dissolution of native oxide layers on the lithium surface, as proposed in the literature. The results showed that the time required for complete dissolution of the oxide layers was on the order of several days. As the temperature of the cells was increased the impedance response decreased. This result is consistent with two hypotheses, that the high-frequency capacitive loop is due to reactions at the lithium metal surface or that the loop is due to a dielectric behavior of the electrolyte.

Experiments using 430 stainless steel electrodes were performed to test the hypothesis that the loop was associated with a dielectric behavior of the electrolyte. The results obtained proved that the high-frequency capacitive loop is associated instead with reactions at the lithium electrode and not with a dielectric behavior of the electrolyte. The low-frequency behavior was consistent with that expected for blocking electrodes. However, at high frequencies, the impedance was influenced by a non-uniform current distribution.

The objective of the modeling work was to find a bridge between easily-used circuit models and more complex physico-chemical models. EIS is not a stand-alone technique, and additional information was needed to develop such a model. An extensive literature review was done to investigate the reactions and mechanisms of transport that control the symmetric lithium coin cells. A simplified set of reactions, which include the oxidation reduction reaction of lithium and the reactions due to the presence of water as a contaminant, was chosen. The products of the reactions chosen include LiOH, LiO_2, and H_2. Independent observations supported the choice of reactions. The impedance data and broken seals in the cells provide evidence of hydrogen evolution. Microscopic and Scanning Electron Microscope (SEM) micrographs provided evidence of the formation of solid films on the lithium surface, consistent with the formation of LiOH and LiO_2. Also, the micrographs showed that the film formed at the perimeter of the cell which is evidence of a non-uniform current distribution.

Two possible mechanisms of transport were modelled. Both models provided evidence that the distribution of time constants observed in the high-frequency capacitive loop can be attributed to reactions at the lithium electrode. The models developed are consistent with the impedance response and are supported by independent observations.

CHAPTER 1
INTRODUCTION

Rechargeable lithium batteries are a promising energy source for consumer, industrial, and military applications. Lithium batteries are appealing for these applications because lithium metal offers a low weight anode (6.99 g mol-1) with high negative potential (-3.05 V/NHE) and high specific capacity (3.76 A h g-1).[1] The overall performance of a lithium rechargeable battery depends on the choice of cathode, anode, electrolyte, and the electrode-electrolyte interfacial properties.[2]

Solid polymer electrolytes (SPEs) offer improved lithium battery safety as compared to liquid electrolytes, since SPEs do not contain any volatile or reactive components. On the other hand, SPEs are known to result in batteries with insufficient performance, suffering from large voltage losses in the electrolyte during passage of a current.[3] For this reason, new materials are being developed for the next generation of lithium-based batteries.[4] The search for optimal chemistry and battery design for a given application can be costly and time-consuming. Mathematical modeling can achieve many of these goals as well as improve the fundamental understanding of the processes inside the battery.[5]

Electrochemical Impedance Spectroscopy (EIS) is an attractive experimental technique to study lithium batteries because it is non–destructive and a variety of capacitive and resistive properties of the material can be determined in a single brief experiment. Interpretation of impedance data is generally guided by use of equivalent electrical circuits. Both simple lumped-parameter circuits and more complex finite-transmission-line circuits have been used. The formulation of the overall circuit network involves the semi-empirical addition of circuit elements until the model provides an adequate description of the impedance response.

Upon the establishment of an appropriate network, a deductive process is used to relate the properties of the system to the individual circuit elements, which comprise the overall network. One limitation of such electric circuit models is that an unambiguous interpretation of the data is not possible. For particular impedance spectra, more than one circuit network can be constructed which would provide equivalent statistically valid fits, and each of these models can arise from extremely different interpretations. This reduces the efficacy of circuit networks for interpretation of the physical properties and the kinetic processes of the system. A less ambiguous approach for interpreting impedance data is to develop physico-chemical deterministic models based on the governing equations, which describe the physics and chemistry of the system and that can be regressed to the experimental data.

The objective of this work was to find a bridge between the complex physico-chemical models with more commonly used equivalent circuit models. The work combined experiments with the development of models that could be applied to lithium-based battery systems.

This investigation was performed as part of NASA's Polymer Energy Rechargeable Systems (PERS) program. The program was established to develop the next generation of lithium-based, polymer electrolyte batteries for aerospace applications. The goal of the program is to develop a space-qualified, advanced battery system embodying a solid polymer electrolyte and lithium-based electrode technologies and to establish world-class domestic manufacturing capabilities for advanced batteries with improved performance characteristics that address NASA's future aerospace battery requirements.[6]

CHAPTER 2
CHARACTERISTICS OF LITHIUM–BASED BATTERIES

Lithium–based batteries have been the focus of research for the last decades. These batteries offer significant advantages such as reduced weight and volume of the energy storage system, improved reliability, lower power system life cycle costs, higher energy density, and a more benign environmental impact.[2] For these reasons they are considered for diverse applications that include portable electronic devices, such as cellular phones and laptops computers, electric vehicles, space explorations, uninterrupted power supplies, and medical devices. Lithium-ion batteries have replaced lead-acid, nickel-metal, and nickel-cadmium battery systems for several applications.

2.1 History of Batteries

The first battery reported in history was invented by Alessandro Volta in the year 1799.[7] He first named it "artificial electrical organ," because he was trying to reproduce the behavior of the *torpedo* fish. His invention was later known as the "Pile." The "artificial electrical organ" was the result of a controversy between Volta and his colleague Luigi Galvani, a medical doctor at Bologna University.[7,8] Galvani observed that he obtained muscular contraction in a frog by touching one end of the leg with one metal and the other end with a different metal. He concluded that the "animal electric fluid" was the source of the contraction. Volta, on the other hand, believed that the contact of dissimilar metals was the true source of stimulation. To test his hypothesis, he built the "artificial electrical organ." The apparatus consisted of a moistened porous pad sandwiched between two dissimilar metals. A detailed sketch of it is presented in Figure 2–1. The metals used were silver and zinc, and the disk was moistened with water for some

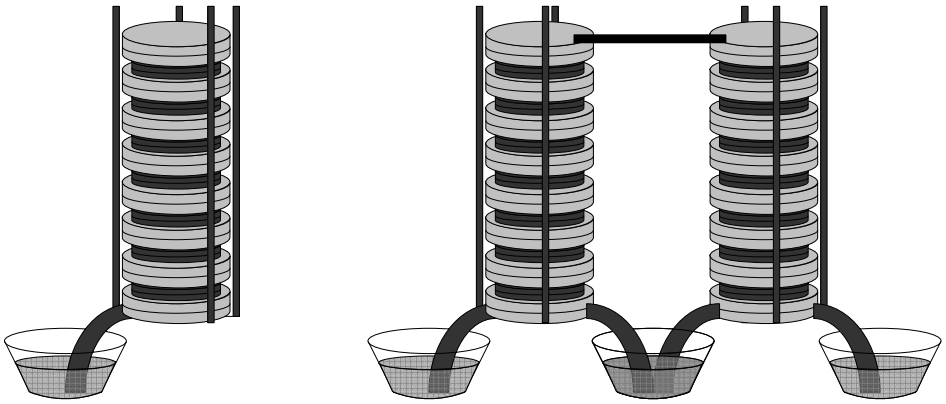

Figure 2–1: Schematic of the "artificial electrical organ" or the "Pile" developed by Alessandro Volta in 1799. Figure reproduced from A.P. Chagas, "The 200 Years of the Electric Pile," *Quimica Nova*, 23 (2000) 427–429.[7]

cells and a saline solution for others. Volta observed and reported that the saline solution worked better than pure water in the moistened disks, but he showed no interest in exploring the role of the electrolyte since he believed that the metal–metal interface was the source of electricity.[8]

In the years that followed, other means of producing electricity were invented. The British researcher John Frederich Daniell developed an arrangement in which a copper plate was located at the bottom of a wide–mouthed jar, and a cast zinc piece was located at the top. Two electrolytes were employed. A saturated copper sulphate solution covered the copper plate and extended halfway up the remaining distance toward the zinc piece. Then a zinc sulphate solution was carefully poured above the copper sulphate and immersed the zinc. The two solutions were separated by a porous clay cylinder separator. It was one of the earliest practical "laboratory" electrical sources, but it was not much used outside the laboratory.[8,9] Among all the systems invented, the most successful were the ones developed by Grove in 1839 and Bunsen in 1842. Grove added an oxidizing agent to prevent accumulation of hydrogen at the cathode where it reduced the

voltage the cell produced. Bunsen improved Groves cell by substituting cheap carbon for the expensive platinum cathode.[9]

None of these technologies survives today. The first enduring invention came from Raymond Gaston Planté, who developed the lead-acid cell in 1859. The next major development was the wet cell by the French engineer Georges Laclanché. He used a cathode of manganese dioxide mixed with carbon and an anode of zinc in the form of a rod. The electrolyte was a solution of ammonium chloride. This chemical system is used in flashlight batteries.[9]

The production of batteries was greatly increased during the First World War as a means of powering torches and field radios. Other milestones in battery production include the widespread radio broadcasting, which brought battery–operated wireless into many homes. During the inter–war years, battery performance was greatly enhanced through better selection of materials and methods of manufacture. Batteries have now become an essential part of everyday life. They are power sources for millions of consumer, business, medical, military and industrial appliances worldwide.

2.2 Characteristics of Lithium-Based Batteries

Lithium is the most chemically reactive metal and provides the basis for today's most compact power systems. Nearly all high–density storage systems use lithium because it has a specific capacity of 3860 Ampere–hour per kilogram of mass (Ah/kg) compared to 820 Ah/kg for zinc and 260 Ah/kg for lead. Depending on the cathode, cells with lithium anodes can produce 1.5 volts to 3.6 volts per cell.

The three primary components of any battery are the cathode, the electrolyte, and the anode. One problem with using lithium metal as the electrode is that it is too reactive. It reacts violently with water and can ignite into flame. Also, as a consequence of the reaction, a film is formed on the metallic lithium. This, in turn, results in continuously increasing electrode surface area and more extensive

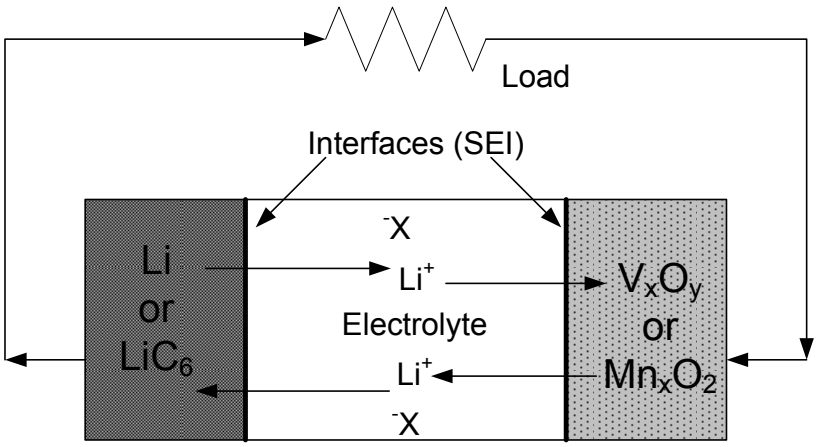

Figure 2–2: Schematic of a rechargeable lithium battery. Figure reproduced from: G.Nazri and G. Pistoia, *Lithium Batteries: Science and Technology*, (Norwell,MA: Kluwer Academic Publishers, 2004).

surface reactions. The insulating, complex deposits that build up on the surface of the electrode lead to the growth of uneven dendrites. To prevent problems caused by the reactivity of lithium, battery makers replace lithium metal with lithium in its ionic state. In this cell, lithium–ions are intercalated into the active material of the electrode rather than being plated out as a metal. At the beginning of discharge, the negative electrode is charged with lithium ions (Li^+) while the positive electrode is ready to accept lithium ions. During discharge, the lithium ions leave the negative electrode and enter the solution phase, while in the positive electrode region lithium ions in the solution phase intercalate into the active material. This behavior results in a concentration gradient, which drives lithium ions from the negative to the positive electrode.[10,11] A schematic representation of a typical Li–ion cell is shown in Figure 2–2. Much effort has been expended in the last decade to improve these batteries, with research devoted to all three components of the cell. These have resulted in significant improvements in the performance and cost.

The newest battery technology is the lithium solid polymer cell, in which the electrolyte is integrated into a polymer plastic separator between the anode and the cathode. The electrolyte is a polymer composite containing a lithium salt. Although the energy density of the solid polymer electrolyte can be similar to that of the ordinary lithium cells, they have the advantage that they can be shaped to fit the space available. In addition, solid polymer batteries are environmentally friendly, lighter because they have no metal shell and safer because they contain no flammable solvent. However, the overall performance of a lithium rechargeable battery depends on the choice of positive electrode, negative electrode, electrolyte, and the electrode–electrolyte interfacial properties.[2]

2.2.1 Anode Materials

The essential reaction of metallic lithium anode is very simple

$$\mathrm{Li} \leftrightarrow \mathrm{Li}^{+} + \mathrm{e}^{-} \tag{2.1}$$

but, in spite of this simplicity, the practical application of Li metal to rechargeable anode has been very difficult because Li metal tends to deposit as dendritic structure during charge, and the disordered metallic deposit gives rise to a poor coulombic efficiency. Extensive research has been dedicated to obtain better anodes.[12–16] The research has concentrated in three areas: improvements of carbonaceous materials; utilization of metallic lithium with stable electrolytes; and search for new materials.[10]

Most of the improvements in anodes actually implemented over the last decade have involved carbonaceous materials, in concert with layered oxides. The reasons that lie behind the commercial success of carbon–based negative electrodes include the relatively low inherent cost of carbon, its excellent reversibility for lithium insertion, and the formation of a protective surface film with many electrolyte

solutions. The choice of anode is based on the need for fast insertion kinetics and a redox potential vs. lithium which provides a sufficiently large cell voltage.

Despite the advances made in carbons, it has been recognized for some years that new anode materials are needed. An increase in the operating voltage above current values for carbonaceous materials is highly desirable to inhibit lithium metal deposition that can occur at fast rates. A large number of alternative possibilities for negative electrodes have been recently reported in the literature that may lead to new directions in meeting the anode challenge.

The goal of developing rechargeable batteries with a metallic Li anode has become more definite. One of the fields in which a Li metal anode is attracting much interest is that of polymer battery systems. To obtain a satisfactory performance from metallic Li anode it is necessary to optimize chemically and physically the interfacial structure between Li anode and the electrolyte. It is necessary to choose appropriate electrolytes to promote the formation of a passivating layer that will protect against side reactions, but that do not impede the diffusion of Li ions across the interface during cycling. Another approach to the improvement of Li cycling efficiency is including some additives in the electrolyte formulation. This method can control or modify the thickness, morphology and chemical composition of the Li surface layer.[10] A detailed description is provided in Subsection 2.2.4. Besides the chemical factors such as electrolytes and additives, some physical factors have an influence on the Li interface structure. The temperature and stacking pressure on the anode have an influence in the surface morphology, which can improve the cycling efficiency.

2.2.2 Cathode Materials

Over the last decade the research on cathode materials has been intense, and remarkable success has been met at the practical and at the theoretical level.[1,17]

The classical criteria for selecting an efficient cathode are based on thermodynamic, kinetic, and practical considerations include

1. The cathode must intercalate or insert Li^+.
2. The cathode has to have low electron energy and low site energy for Li^+.
3. The electrode potential should have limited variations as a function of Li^+ content.
4. The number of sites for Li^+ has to be high and the hosting molecule has to feature low weight and high density.
5. The couple diffusion of electrons and Li^+ in the host, as a function of concentration gradient, must be fast enough to grant a good rate capability.
6. The Li^+ intercalation/insertion has to be reversible to allow cyclability.
7. The cathode must be stable towards the electrolyte over the entire operating voltage range.
8. The cathode material should be easy to synthesize, should be non toxic, and of low cost.
9. The synthesis must be reproducible and should allow the production of a material with the desired particle size.
10. The material has to be easily processed into a practical electrode.
11. A favorable interface should be formed between the cathode and the electrolyte.

2.2.3 Electrolyte

The selection of the electrolyte is determined by the electrode reactions. The basic requirements of a suitable polymer electrolyte for lithium batteries are[10]

1. High ionic conductivity to minimize the cell resistance and resistive heating of the device.
2. High chemical stability to prevent decomposition of electrolyte on the surface of a highly reducing anode material and a highly oxidizing cathode material.
3. Electrochemical stability to tolerate the high voltage difference between the anode and the cathode (> 4 V).
4. Low melting point to provide sufficient conductivity at sub–ambient temperatures and prevent solidification an phase separation.

5. High boiling point to provide safety and prevent explosions resulting from high pressure build–up in the cell.
6. Non–toxicity to be accepted environmentally for ease of handling, mass production, and waste treatment.
7. Low cost, safety, and ease of processing.

Although chemical stability of the bulk electrolyte is a requisite for long battery life, the most common electrolytes (liquids and polymer) are not stable at the open circuit potential for lithium metal. However, the formation of surface films at the electrode surface limits the extent of these reactions and reduces the rates to levels that allow the useful cycle and calendar life of the battery to be achieved.[10,18–20] But it is important to understand that these surface films provide layers with different transport properties from the bulk electrolyte and through which the lithium ions must pass (See Figure 2–2). These layers are usually referred to as the solid electrolyte interface or SEI, and they usually play a crucial role in both the cycle life and also in the rate capability of the battery. A detailed description of the SEI is presented in Section 2.2.4.

The weight of the electrolyte is a major contribution to that of the complete battery.[21] Battery–makers are interested in finding ways of packing battery power into smaller packages that enable electronics manufacturer to continue their drive for miniaturization. For this reason ionically conducting polymers have been the focus of much fundamental and applied research for many years.[2,3,18,19,22–27]

Since the introduction of polymer electrolytes in the 1970's many researchers have attempt to identify solid polymer electrolytes formulations which would combine high ionic conductivity, good mechanical properties, and good interfacial behavior with lithium metal electrodes.[2,24] The most common polymer electrolyte investigated has been based on polyethylene oxide (PEO) which is commercially available in a relatively pure state at reasonable cost.[10] The efforts were focused on the bulk properties of polymer electrolytes based on combinations of PEO with

various lithium salts and on the characteristics of electrochemical processes at the electrode–polymer electrolyte interface. This led to the development of high ionic conductivity polymer systems that are almost competitive with liquid electrolytes at elevated temperatures.

However, at elevated temperatures, PEO–based electrolytes as well as other polymer–based electrolytes are mostly in their amorphous state, in which the mechanical properties are relatively poor.[24] The addition of ceramic fillers has shown an improvement of the mechanical properties of the electrolyte. Also, the ceramic fillers induce an enhancement of the Li transference number and of the ionic conductivity.[24,28] It has also been shown that the preparation procedure of the electrolyte and the environment play a major role with respect to the addition of the filler.[24]

The implementation of polymer electrolytes in commercial batteries requires an increase in ionic conductivity at ambient temperature. A lot of research has been done to find polymer electrolytes that have high ionic conductivity at ambient temperature. For example, Kim and Smotkin studied the effect of plasticizers on transport of electrochemical properties of PEO–based electrolytes for lithium rechargeable batteries.[2] The results showed that the plasticized electrolytes have higher conductivity and higher diffusion coefficient at the selected temperatures. Also, the interfacial resistance between the polymer electrolyte and the Li metal surface decreased. But, the cationic transference number was reduced with the use of some plasticizers.

The design of polymer electrolytes for lithium batteries is a complex problem that needs to be approached with a combination of sophisticated modeling, diagnostic techniques and significantly greater synthetic effort than has been applied in the past. Only then can the rates of side reactions be related to lifetime issues.[10]

2.2.4 Electrode–Electrolyte Interface

Peled was the first to introduce and name the electronically protective, but conductive, interfacial layer as solid electrolyte interface or SEI.[18,19] According to Peled, the SEI is a heterogenous film, consisting of a mosaic of numerous individual particles of different chemical composition being in partial contact with each other at the grain boundaries. The chemical composition of these particles depends on the type of solvent, or solvent mixture, type of electrolyte salt and on the impurities. The lithium conduction through the SEI is provided by ionic transport mainly at the grain boundaries of inorganic compounds such as LiCl, LiF and Li_2O or near the surface of the particles via lattice defects. A schematic representation of the electrode–electrolyte interphase is presented in Figure 2–3. In Figure 2–3(a) a native oxide film can be observed. It is well accepted that commercial lithium foils have a native oxide layer that is composed primarily of a Li_2O layer and Li_2CO_3/LiOH layer.[10,29] The polymer electrolytes have a rough surface, and so, in contact with lithium, some spikes penetrate the oxide layer and the lithium metal such that a SEI is formed at the Li/SPE interface. In other areas, softer contacts between the SPE and lithium are formed. In these areas the SEI forms on the native oxide layer, or as a result of the retreat of lithium during corrosion, the native oxide layer breaks and the gap is filled by the formed SEI. The net result is that only a fraction of the lithium surface is in intimate contact with the polymer electrolyte. At open circuit potential, the rate limiting step for the deposition–dissolution process is Li^+ transport in the SEI.

The components of the interface layer depend on the nature of the electrolytes and the additives added to the electrolyte. Tables 2–1 and 2–2 summarize the effect of several liquid electrolytes and additives in the composition of the SEI layer.

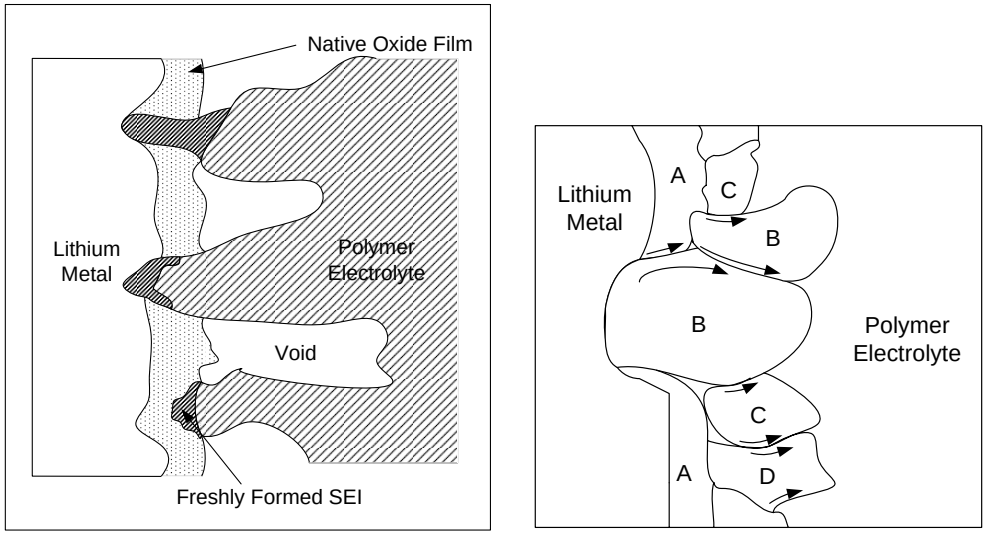

(a) (b)

Figure 2–3: Schematic presentation of the lithium–polymer electrolyte interphase.(a) Overall interphase (b) Small segment of the interphase. Figure reproduced from: E. Peled, D. Golodnitsky, G Ardel and V. Eshkenazy, *The SEI Model–Application to Lithium Polymer Electrolyte Batteries*, Solid State Ionics 40 (1995) 2197-2204.

Table 2–1: Chemical composition of passivation films formed on lithium metal surface in contact with different electrolytes.

Electrolyte	Passivation Film
Without electrolyte (native film)	LiOH, Li_2CO_3, Li_2O
General PC systems	$CH_3CH(OCO_2Li)CH_2OCO_2Li$
PC/$LiPF_6$	LiF, Li_2O, LiOH
PC/$LiClO_4$	Li_2CO_3, LiOH, Li_2O, LiCl, $ROCO_2Li$, $LiCHClCHCl$, $LiCH_2CHClCH_2Cl$
General EC systems	$(CH_2OCO_2Li)_2$
General DMC systems	CH_3OCO_2Li
General DEC systems	$CH_3CH_2OCO_2Li$, CH_3CH_2OLi
SO_2/$LiAlCl_4$	$Li_2S_2O_4$, Li_2SO_3, LiS_nO_6,$Li_2S_2O_5$

Table reproduced from: G.Nazri and G. Pistoia, *Lithium Batteries: Science and Technology*, (Norwell,MA: Kluwer Academic Publishers, 2004).

Table 2–2: Chemical composition of passivation films on the Li metal in contact with additives used to enhance the cycling efficiency.

Group	Additive	Major Acting Mechanism
Inorganic	HF	Formation of LiF layer
	AlI_3, MgI_2, SnI_2	Formation of Li-alloy layer
	S_x^{-2}	Formation of protecting film
Organic	2Me-furan, 2Me-THF, Pyridine derivatives, Sipyridyl derivatives	Surface adsorption, formation of organic protecting film, solvation of Li^+
	Cetyltrimetylammonium chloride	Electrode surface adsorption
	Nonionic surfactants, Crown Ethers	Electrode surface adsorption, solvation of Li^+
	Benzene	Electrode surface adsorption
Gas	CO_2	Formation of Li_2CO_3 layer
	N_2O, CO	Formation of protecting film

Table reproduced from: G.Nazri and G. Pistoia, *Lithium Batteries: Science and Technology*, (Norwell,MA: Kluwer Academic Publishers, 2004).

CHAPTER 3
ELECTROCHEMICAL IMPEDANCE SPECTROSCOPY THEORY

Impedance can provide valuable insights into the behavior of a large variety of substances, components and systems. In many materials the impedance response varies as the frequency of the applied voltage changes. This may be due to the physical structure of the material, to chemical processes within it, or to a combination of both. Thus, if a measurement of impedance over a suitable frequency range is made, and the results are plotted on suitable axes, it is possible to relate the results to the physical and chemical properties of the material. This technique is known as electrochemical impedance spectroscopy and is use to investigate materials and chemical mechanisms.

Electrochemical impedance spectroscopy is a measurement of the conductive and dielectric properties of electroactive systems over a wide range of frequencies. Its popularity and applicability has increased dramatically over the past 30 years with the introduction of fast–response potentiostats and frequency response analyzers. Impedance spectroscopy has been applied extensively in electrochemistry, especially in battery and sensor research.[30,31]

This chapter provides a basic understanding of the concepts that are involved in electrochemical impedance spectroscopy. Detailed discussions of the technical and theoretical issues associated with electrochemical impedance spectroscopy are available elsewhere.[30–41]

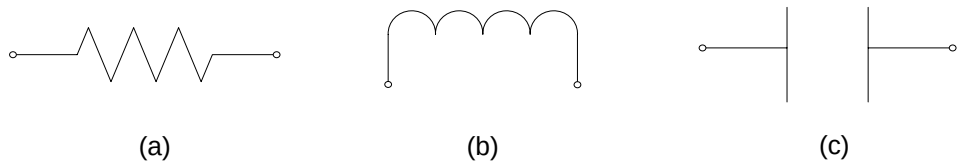

Figure 3–1: Passive elements that serve as a component for an electrical circuit.

3.1 Impedance Response of Electrical Circuits

Impedance is defined to be the ratio of the voltage phasor, V, to the current phasor, I. Ohm's law can be expressed in phasor form as[42,43]

$$Z = \frac{V}{I} \tag{3.1}$$

The impedance Z indicates opposition to current flow and it has the units of ohms. Impedance is in general a complex number and not a function of time. It completely defines the element's behavior in an ac circuit.

Electrical circuits can be constructed from the passive elements shown in Figure 3–1. For a pure resistor, as the one shown in Figure 3–1(a), the impedance response is expressed as

$$\mathrm{Z_{resistor}} = \mathrm{R} \tag{3.2}$$

for the inductor shown in Figure 3–1(b)

$$\mathrm{Z_{inductor}} = j\omega\mathrm{L} \tag{3.3}$$

and for the capacitor shown in Figure 3–1(c)

$$\mathrm{Z_{capacitor}} = \frac{1}{j\omega\mathrm{C}} \tag{3.4}$$

The impedance response of resistors, inductors, and capacitors are used to construct the impedance response of circuits.

3.2 Experimental Considerations

EIS is a small-signal technique in which a sinusoidal current or potential perturbation is imposed on the system of interest and the corresponding potential or current response is measured, Figure 3–2. Comparison of the input and output signals provides the impedance at a given perturbation frequency.

An appealing feature of EIS is that systems with characteristic time constant distributed over a wide range of time scales can be studied. A variety of capacitive and resistive properties of the material can be determined in a single brief experiment by analyzing the response over a wide frequency range. Also, EIS is a non–destructive method for the evaluation of a wide range of materials, including coatings, anodized films, corrosion inhibitors, batteries and fuel cells.[32,33]

The main difficulty in the impedance studies originate from the complexity of electrochemical systems. An important requirement for a successful performance of the investigation is that the system must be linear.[34] Electrochemical systems are usually non–linear but the requirement for linearity could be fulfilled if the amplitude of the input signal is small enough to allow linearization of the response. In addition, the input signal should be sufficiently small as to avoid irreversible changes in the system properties (See Figure 3–2). The frequency range must be wide enough to attain the high frequency limit of the impedance equal to the electrolyte resistance.

The electrochemical cell plays a major role in the success of the impedance experiments. The cell can consist of 2, 3 or 4 electrodes immersed in an electrolytic solution contained in a vessel, Figure 3–3. The electrochemical interface whose impedance is measured is generally located between the electrolyte and the working electrode.[32] The counter electrode is used to allow current to flow through the cell. It is usually a large surface area electrode with very low impedance. When concentration gradients in the electrolyte solution affect the impedance response

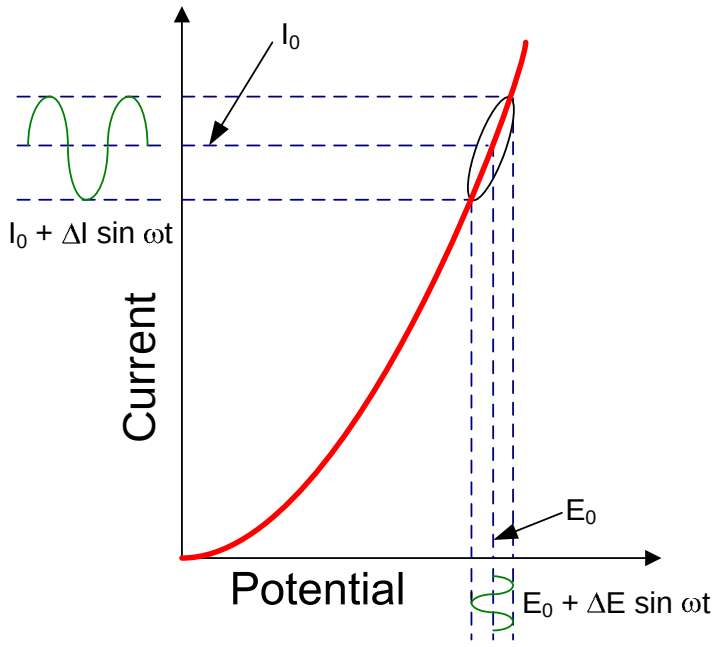

Figure 3–2: Small signal analysis of an electrochemical non–linear system.

of the system, a 3–electrode cell should be used. The reference electrode should be placed as close to the system as possible. A 4–electrode cell is used when transport through a membrane is studied. The potential difference across the membrane is measured by means of two reference electrodes, one on each side of the membrane.

The modulation technique also play an important role in the success of the experiments. There are two modulations, potentiostatic and galvanostatic. The

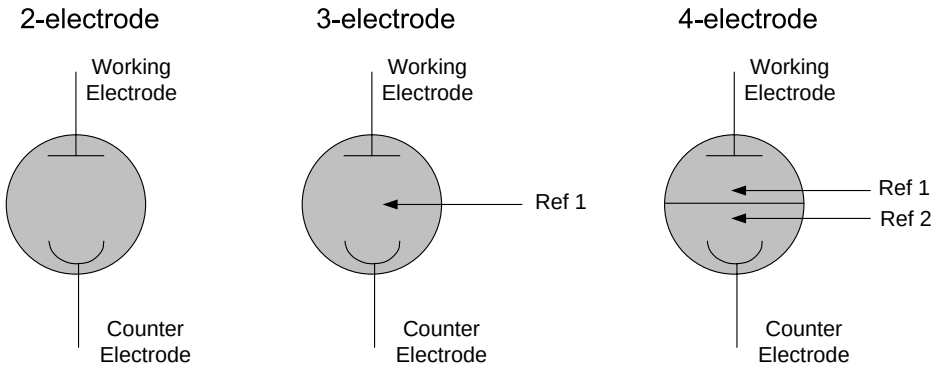

Figure 3–3: Electrode configuration in an electrochemical cell.

potentiostatic modulation is the standard approach; in this modulation linearity is controlled by the potential. The galvanostatic modulation is good for nonstationary systems, like corrosion and drug deliver. However, this modulation requires a variable perturbation amplitude to maintain linearity. Additional considerations include the use of short leads, good and shielded wires, and the use of a faradaic cage when the impedance of the system is large, resulting in small currents.

3.3 Error Structure

Interpretation of the impedance data requires a process model and a quantitative assessment of the error structure. The error structure of the measurement is used implicitly in regression analysis and has a significant influence on the quality and amount of information that can be extracted from impedance data. The stochastic errors can also influence the Kramers-Kronig relations for determining the internal consistency of the data.[40]

3.3.1 Kramers–Kronig Relations

The Kramers-Kronig relations are integral equations, which constrain the real and imaginary components of the impedance for systems that satisfy conditions of causality, linearity, and stability. This means that the system response to a perturbation cannot precede the perturbation, that the system responds linearly with respect to the perturbation, and that the perturbations to the system do not grow. In principle, the Kramers-Kronig relations can be used to determine whether the impedance spectrum of a given system has been influenced by bias caused, for example, by time-dependent phenomena or instrumental artifacts.

3.3.2 Measurement Model Approach

The measurement model approach developed by Agarwal *et al.* is used to identify the error structure of the measurements. The objective of the measurement model toolbox is to account for measurement errors in the analysis of electrochemical impedance spectroscopy. The measurement model has been used to determine

whether the residual errors in the regression are due to an inadequate model, to failure of data to conform to the Kramers-Kronig assumptions, or to noise. Since the model satisfies the Kramers-Kronig relations, it can be used to identify portions of the spectrum that were inconsistent with these relations. The measurement model provides more than a preliminary analysis of impedance data in terms of the number of resolvable time constants and asymptotic values. The measurement model can be used as a filter for lack of replicacy that allows accurate assessment of the standard deviation of impedance measurements. This information is critical for selection of weighting strategies for regression, provides a quantitative basis for assessment of the quality of fits, and can guide experimental design. The error analysis provides information to be incorporated into regression of process models. The analysis consists of two parts; the first one is a preliminary analysis to determine the error structure and the second one is to assess consistency with the Kramers-Kronig relations. A detailed description of the measurement model approach and the results obtained from the experiments are presented in Chapter 4.

3.4 Impedance Spectroscopy Data Analysis

Graphical methods provide the first step toward interpretation and evaluation of impedance data.[44] Impedance data are usually represented in impedance–plane or Nyquist format, as shown in Figure 3–4. This plot shows the impedance response of a symmetrical lithium based battery cell with electrolyte composition PEO_{16}LiTFSI. In this plot, the limits of the real part of the impedance represent the electrolyte resistance R_e at high frequency and the sum of the electrolyte resistance and the charge transfer resistance $R_e + R_f$ at low frequency. One disadvantage of this type of format is that the frequency dependence is hidden. Nyquist plots are very popular because the shape of the locus of points yields insight into possible mechanisms or governing phenomena. For example, if the locus

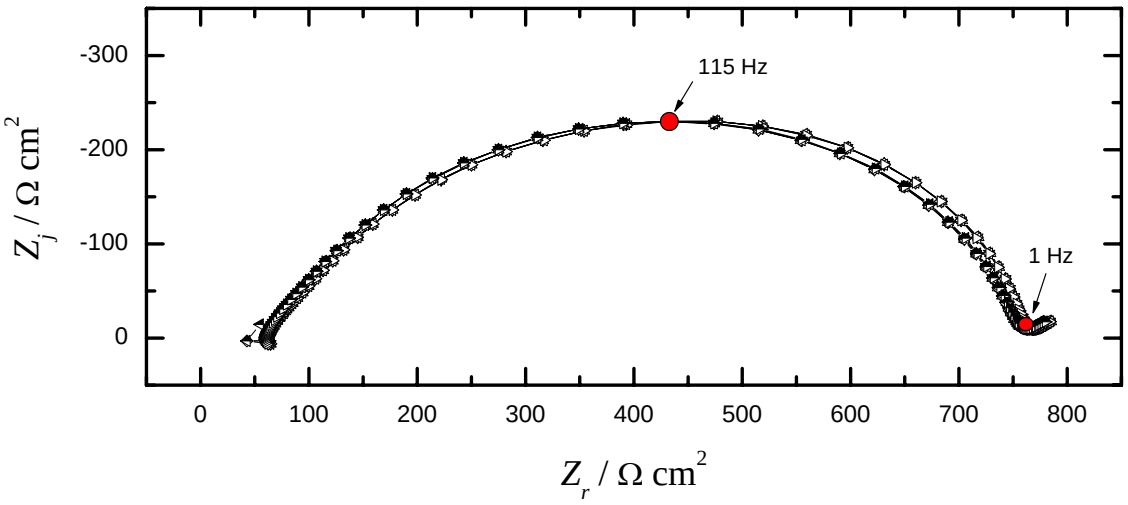

Figure 3–4: Impedance–plane or Nyquist representation of impedance data for Cell NA–ATi. The open symbols represent measurements taken 15 hour after the cell preparation. The half–full symbols represent measurements taken approximately 48 hours after the cell preparation.

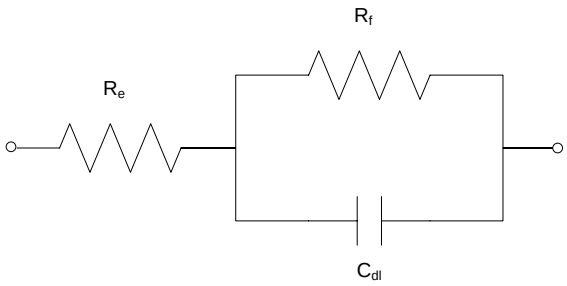

Figure 3–5: Schematic representation of a simple reactive system.

of points traces a perfect semicircle the impedance response corresponds to a single activation-energy-controlled process, such as that shown in Figure 3–5. A depressed semicircle represents a system with characteristic time constant distributed over a wide-range of time scales.

Other common representations are the Bode plots shown in Figure 3–6 and plots of the real and imaginary part of the impedance as functions of frequency shown in Figure 3–7. Bode plots have the advantage that the frequency dependence is shown in the graph. Frequency is generally presented on logarithmic scale to reveal the important behavior seen at lower frequencies. In electrochemical

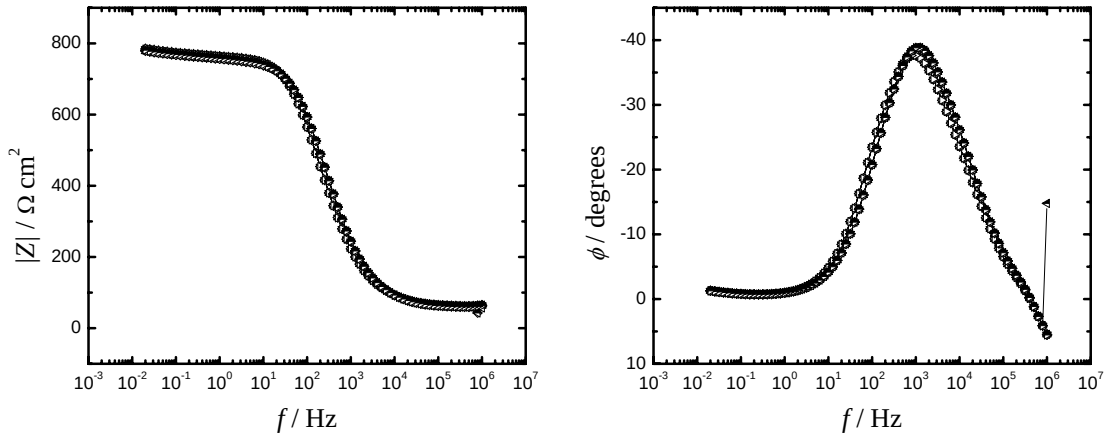

(a) (b)

Figure 3–6: Bode representation of impedance data, magnitude and phase angle, for Cell NA–ATi, respectively. The open symbols represent measurements taken 15 hour after the cell preparation. The half–full symbols represent measurements taken approximately 48 hours after the cell preparation.

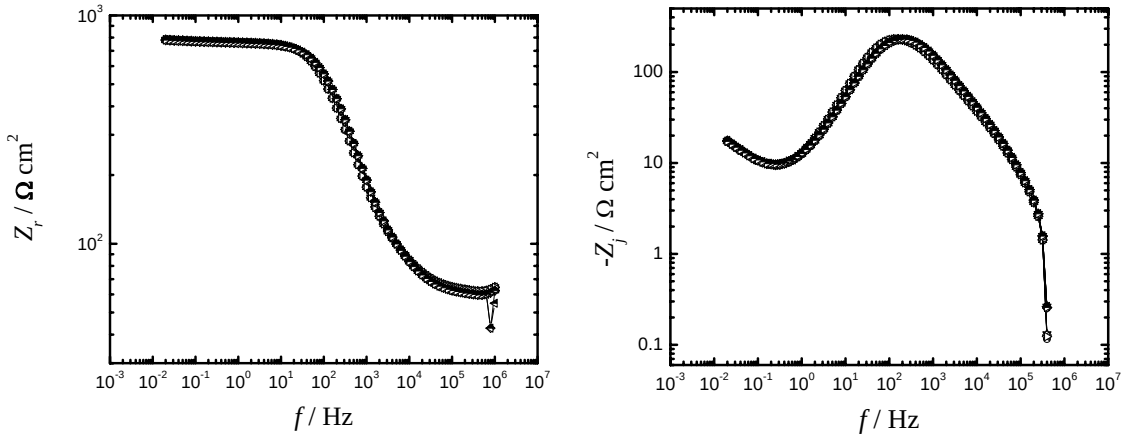

(a) (b)

Figure 3–7: Plots of the real and imaginary part of the impedance as a function of frequency for Cell NA–ATi. The open symbols represent measurements taken 15 hour after the cell preparation. The half–full symbols represent measurements taken approximately 48 hours after the cell preparation.

systems Bode representation has serious drawbacks. For example, the influence of the electrolyte resistance confounds the use of phase angle plots to estimate characteristic frequencies. However, if an accurate estimate of the electrolyte resistance is available, a modified Bode representation that can be used to avoid the drawbacks. The plots of the real and imaginary part of the impedance as functions of frequency have the advantage that the characteristic frequencies can be easily identified. When the frequency is plotted in logarithmic scale for the imaginary part of the impedance, the slopes at low and high frequency are $+1$ and -1, respectively, for a simple reactive system as the one shown in Figure 3–5. Departure from ± 1 provides an indication of distributed processes. Observation of multiple maxima shows that the data must be interpreted in terms of more than one process.

A detailed analysis of the experimental data is presented in Chapter 5.

3.5 Impedance Response Models

Interpretation of impedance data is generally guided by use of equivalent electric circuits. Both simple lumped-parameter circuits and more complex finite–transmission-line circuits have been used. The formulation of the overall circuit network involves the semi-empirical addition of circuit elements until the model provides an adequate description of the impedance response. Upon the establishment of an appropriate network, a deductive process is used to relate the properties of the system to the individual circuit elements, which comprise the overall network. A limitation of such electric circuit models is that an unambiguous interpretation of the data is not possible. For particular impedance spectra, more than one circuit network can be constructed which would provide equivalent statistically valid fits; and each of these models can arise from extremely different interpretations. This reduces the efficacy of circuit networks for interpretation of the physical properties and the kinetic processes of the system. A less ambiguous approach for interpreting impedance data is to develop physico-chemical models

based on the governing equations, which describe the physics and chemistry of the system. To develop such a refined model it is necessary to identify the reaction mechanism or if not known assume kinetic and transport mechanisms. Then, expressions for the current contributions will be written.

The faradaic current density, i_f, can be expressed in terms of a steady time-independent value and an oscillating value as

$$i_f = \bar{i}_f + R_e\{\widetilde{i}_f e^{j\omega t}\} \tag{3.5}$$

The oscillating component of the current can be calculated using a Taylor series expansion about the steady–state value as

$$\widetilde{i}_{i,f} = \left(\frac{\partial f}{\partial V}\right)_{c_i,\theta_k} \widetilde{V} + \sum \left(\frac{\partial f}{\partial c_{i,0}}\right)_{V,c_{j\neq i},\theta_k} \widetilde{c}_{i,0} + \sum \left(\frac{\partial f}{\partial \theta_k}\right)_{V,c_i,\theta_{l\neq k}} \widetilde{\theta}_k \tag{3.6}$$

where V is the interfacial potential, $c_{i,0}$ is the local concentration of the bulk species and θ_k is the surface coverage of the absorbed species. The charging current is given by

$$\bar{i} = \bar{i}_f + c_{dl}\frac{dV}{dt} \tag{3.7}$$

and

$$\widetilde{i} = \widetilde{i}_f + j\omega c_{dl}\widetilde{V} \tag{3.8}$$

To obtain an expression for impedance it is necessary to solve equation (3.6). Using the reaction mechanism or the assumed mechanisms, equations that relate concentration and surface coverage to voltage can be introduce to obtain an equation of current in terms of interfacial voltage. Then the impedance of the system is obtained by comparing the oscillating term of the cell potential, $\widetilde{V}$, and the oscillating term of the current, $\widetilde{i}$. The cell potential is defined as

$$U = iR_e + V \tag{3.9}$$

and

$$\widetilde{U} = \widetilde{i}R_e + \widetilde{V} \tag{3.10}$$

where R_e is the electrolyte resistance. The impedance of the system is defined to be

$$Z = \frac{\widetilde{U}}{\widetilde{i}} \tag{3.11}$$

Substituting equations (3.8) and (3.10) into equation (3.11), an expression for the impedance of the system in term of electrolyte resistance, interfacial potential and charging current is obtained as

$$Z = R_e + \frac{\widetilde{V}}{\widetilde{i}} \tag{3.12}$$

If the kinetic and transport mechanisms were assumed the impedance relation obtained from equation (3.12) is compared to the experimental values. If a good fit is obtained the relation is accepted as the model for the system. However, if a good fit is not obtained new kinetic and transport mechanisms are assumed and all the procedure is repeated until a good fit is obtained.

The process models developed for the experimental data is presented in Chapter 7.

CHAPTER 4
EXPERIMENTAL DESIGN AND ERROR ANALYSIS

There exists a rich literature on research of battery systems, both, experimental and modeling work. Different techniques have been used to study the mechanisms of transport inside batteries. Some of the techniques include constant current discharge, pulse discharge, cyclic voltammetry, abuse tests, and impedance spectroscopy.[1–3,5,6,11,12,14,15,17,25,26,28,45–63]

In this work EIS was used to study symmetric lithium cells. The goal was to develop a model that describes the physics and chemistry of the system, but that can be regress to the experimental data. This model would be the first step toward the development of refined equivalent circuit models for lithium-based battery systems.

Experiments were performed to provide reliable impedance data that were used to test the models. In this chapter a detailed description of the experimental component of this work is provided. It include a description of the experimental system and experimental design, as well as, a description of the method used to test the quality of the data. A detailed description of the model development is presented in Chapter 7.

4.1 Experimental System

The system used in this work was a symmetric Li|SPE|Li coin cell. All cell assembly was done in dry room atmosphere (-35°F dew point, nominal). A schematic diagram of the battery cell assemble is shown in Figure 4–1. A two lithium–metal–electrode system was used since researchers have stated that a two–electrode system will introduce much less error than what would result from an ill–placed third (reference) electrode.[2,17] The cell was built using a thin, insulating

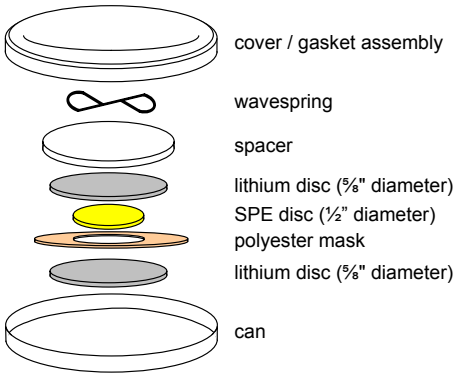

Figure 4–1: Schematic of the cell sandwich. The cell was build using a thin, insulating mask to separate the electrodes. The mask was intended to prevent short circuit.

mask to separate the electrodes and to provide a well defined reservoir for the melted electrolyte. This mask was intended to prevent short circuits that were observed in earlier coin cell work done at NASA Glen Research Center.[6] The mask was centered on top of the anode and covered with the SPE disc. The lithium electrode was then centered on top of the SPE disc before closing the cell. A wave spring provided an internal pressure of 18 psi. The mask outside diameter was oversized to assist in the alignment of the electrode sandwich in the cell can. The inside diameter established an apparent active area of 1.27 cm^2.

The electrolyte system used in this research was polyethylene oxide (PEO) plus a lithium imide salt (16 : 1 ether–oxygen:Li). PEO has a regular repeated structure $-CH_2CH_2O-$, is crystalline and has a fusion temperature T_f of 339 K. The imide salt formula is $LiN(SO_2CF_3)_2$. This salt is formally called lithium bis-(trifluoromethanesulfonyl)-imide, but most people abbreviate this to LiTFSI.

The electrolyte was prepared using PEO (Aldrich 6E5 Mv), LiTFSI (3M HQ-115) and acetonitrile as the solvent. PEO and acetonitrile were used as received. The grade of the PEO contains 200 to 500 ppm of Butyl hydroxyl toluene (BHT) as stabilizer. LiTFSI salt was dried for 4 hours under vacuum at 160°C. PEO was

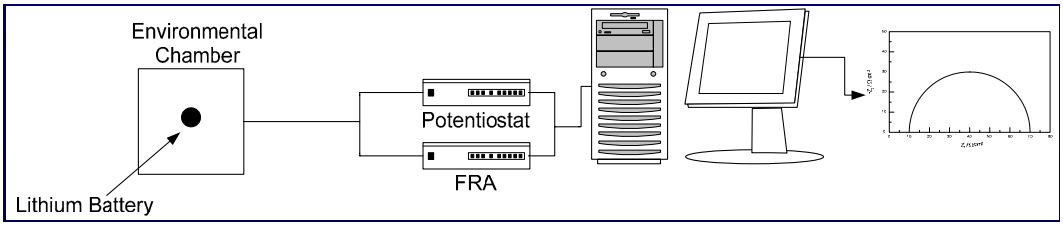

Figure 4–2: Schematic of the experimental setup used for the electrochemical impedance tests.

pre-dissolved as a 12.3 w/w solution in acetonitrile before addition of 23.4 w/w LiTFSI-acetonitrile solution. Quantities were established to provide a 16 : 1 EO:Li ratio after evaporation of the acetonitrile solvent. This is equivalent to 28.9 w/w LiTFSI in the solid electrolyte.

SPE films were routinely prepared by casting the above solution in Teflon Petri dishes and allowing the solvent to evaporate overnight. Casting and solvent evaporation steps were conducted at dry room atmosphere ($< 1\%$ RH). Cured SPE films were dried overnight under vacuum at 45°C and stored in a desiccator before use. This process produced rubbery, freestanding films with a strong self-adherent character. Dry film density at room temperature was 1.26 g/cm^3, giving a salt concentration of 1.27 mole LiTFSI/liter.[45]

Some of the experiments were conducted at NASA Glen Research Center and the others were conducted at the University of Florida Department of Chemical Engineering. A Solartron 1250 Frequency Response Analyzer interfaced with a Solartron 1286 Potentiostat was used to collect the data. For the experiments conducted at NASA facilities, Z-plot was used for experiment control and data acquisition, while software written in–house in Labview was used for the experiments conducted at the University of Florida. The battery cells were placed in a Thermal Product Solutions T-U JR environmental chamber to ensure constant temperature throughout the experiments (See Figure 4–2).

4.2 Experiment Design

The experimental work was divided into four categories. The first set of experiments were conducted at the NASA Glen Research Center. They were steady state impedance measurements that were taken approximately 15 and 48 hours after each cell was prepared. Open circuit potential measurements of four cells were made with six replicates of each scan. The cells were stored at a constant temperature of 80°C for about 10 hours. Then the temperature was decreased to 60°C and kept constant throughout the experiments. The frequency range of the measurements varied from 1 MHz to 0.02 Hz.

The second and third set of experiments were conducted at the University of Florida, Department of Chemical Engineering. The second set of experiments were steady–state impedance measurements where the temperature was increased from 60°C to 90°C in 5°C increments. Open–circuit potential measurements of four cells were performed with six to eight replicates of each scan. The frequency range of the measurements varied from 65 KHz to 0.003 Hz. The third set of experiments were transient impedance measurements performed at a fixed temperature. The measurements were taken consecutively for 48 hours. Two cells were tested. The temperatures used were 60°C and 70°C. The frequency range of the measurements varied from 65 kHz to 0.003 Hz. In these experiments, the temperature inside the environmental chamber was equilibrated to the desired value and then the cells were placed inside the chamber. Twenty–two to tweny–four sequential impedance spectra obtained at the open–circuit potential were analyzed.

The last set of experiments were conducted at NASA Glen Research Center. They were steady state impedance measurements using blocking electrodes. The experiments were designed to test the hypothesis that the impedance response of the symmetric lithium cells was due to the electrolyte and not to the reaction on the lithium metal surface. The cell consisted of PEO–LiTFSI electrolyte

Table 4–1: Summary of the experimental design. The number of sequential measurements is presented.

Group	Temperature (°C)	Time (hour)	25	60	65	70	75	80	85	90	100
1	NA-ATi	15		6							
		48		6							
	NA-BTi	15		6							
		48		6							
	NA-CTi	15		6							
		48		6							
	NA-DTi	15		6							
		48		6							
2	UF-ATe							8			
	UF-BTe			8	6	7	6	6	6	6	
	UF-CTe			6	6	12	6	6	6	6	
	UF-FTe			6	6	6	6	6	6	6	
3	UF-DTr					24					
	UF-ETr			22							
4	NA-AB							6		6	6
	NA-BB		6					6		6	6

sandwiched between two steel electrodes. The cells was exposed to an increasing temperature range varying from 80°C to 100°C in 10°C intervals. Six sequential impedance spectra obtained at the open–circuit potential were collected per set. The frequency range of the measurements varied from 65 kHz to 0.003 Hz. Table 4–1 summarizes the experiments design.

4.3 Measurement Model Analysis

The measurement model analysis was used in this work to test the quality of the impedance data. The analysis consists of identifying the error structure of the measurements and then using that error structure to determine whether the data conform to the Kramers-Kronig assumptions. To determine the error structure of the measurements, a Voigt model was fitted to the experimental data. Voigt elements in series with the solution resistance, *i.e.,*

$$Z = R_0 + \sum \frac{R_k}{1 + j\omega\tau_k} \tag{4.1}$$

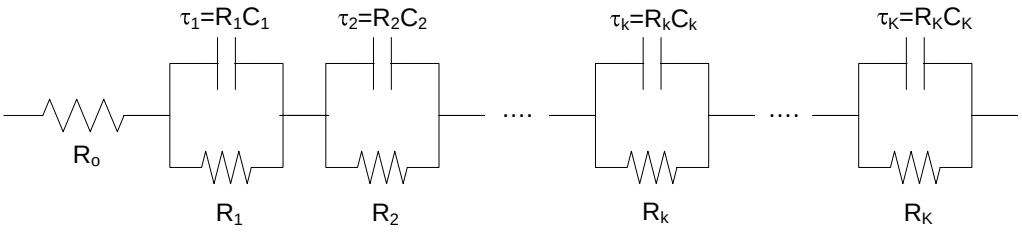

Figure 4–3: Schematic representation of a Voigt circuit used as a measurement model.

were added as shown in Figure 4–3. With a sufficient number of parameters, the Voigt model is able to provide a statistically significant fit to a broad variety of impedance spectra.[64,65] However, the model should not be associated with the set of deterministic or theoretical parameters for a given system.

The use of the measurement model for analysis of the error structure requires replicate measurements of the impedance response using the same measurement frequencies for each replicate. Most electrochemical systems of practical importance are nonstationary and the resulting trending biases direct calculation of statistical quantities such as mean and variance. To eliminate the contribution of the drift from scan to scan, the measurement model was regressed to each scan individually. For the system to be consistent with the Kramers-Kronig relations, it has to evolve sufficiently slowly that the change during one complete scan is insignificant.

4.3.1 Steady State Experiments at Constant Temperature

The impedance response and the model obtained using the measurement model technique of Cell NA–ATi are shown in Figure 4–4. Two data sets are presented in this figure, one was obtained approximately 15 hours after the cell preparation and the other was obtained approximately 48 hours after the cell preparation. The first ten points at high frequency were eliminated because those points were corrupted by instrument artifact effects and were not consistent with the Kramers-Kronig relations. The model agreed well with the experimental data.

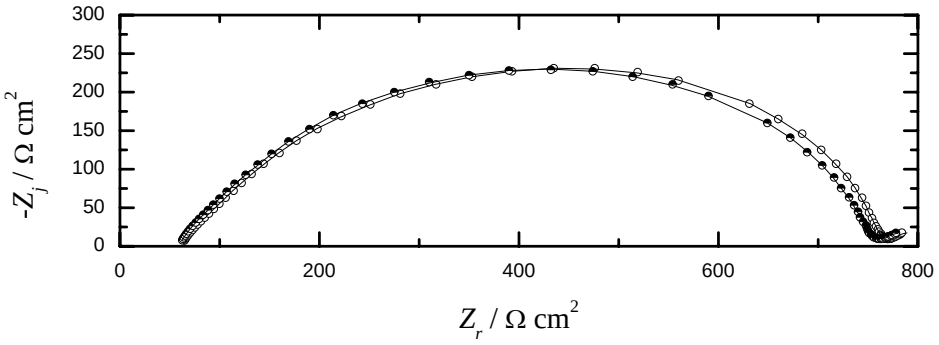

Figure 4–4: Measurement model prediction of impedance data for Cell NA–ATi. The open symbols represent measurements taken 15 hours after their preparation. The half-full symbols represent measurements taken approximately 48 hours after the cell preparation. The solid line represents the measurement model fit.

The error structures for the two data sets are shown in Figure 4–5. These plots show the error structure for the real and imaginary part of the impedance, as well as the error structure model. The error structure model was calculated to be

$$\sigma = 0.001035 Z_j + 0.000467(Z_r - 50.1038) \tag{4.2}$$

This model was calculated using the error structures of the four cells.

For the measurements taken 15 hours after the cell preparation, the standard deviations of the real and imaginary part of the impedance at low frequencies were not equal, Figure 4–5(a). This lack of equality of standard deviation for the real and imaginary parts of the impedance suggests that the data were influenced by non-stationary behavior. The standard deviation of the real and imaginary part of the impedance was equal for the measurements taken 48 hours after the cell preparation, Figure 4–5(b).

The second part of this analysis was to assess for the Kramers-Kronig consistency. A Voigt element model was fitted to the imaginary part of the impedance. The experimentally determined error structure was used to weight the model. When an adequate description was obtained, the model was used to predict the real part of the spectrum. From the estimated variance of the model parameters, a

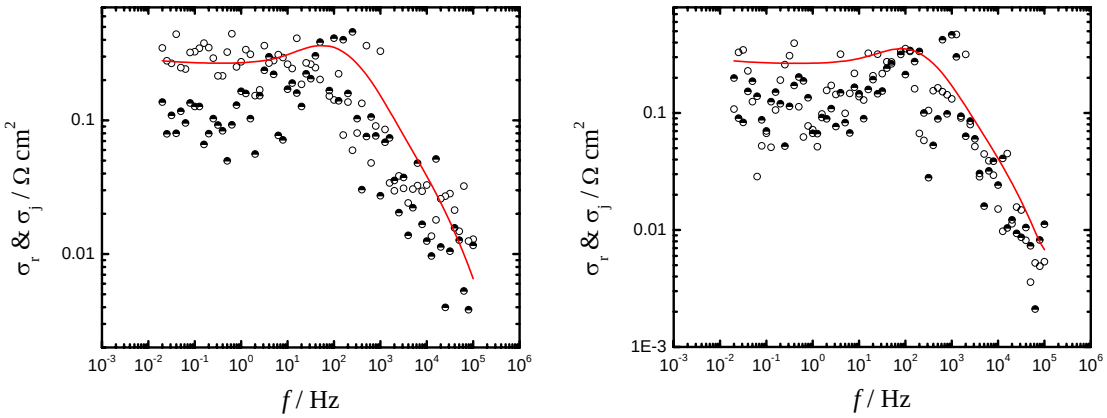

Figure 4–5: Error structure for Cell NA–ATi measurements taken 15 and 48 hours after their preparation, respectively. The open symbols represent the real part of the impedance. The half-full symbols represent imaginary part of the impedance. The solid line represents the error structure model fit.

95–percent confidence interval was found for the model predictions. If the predicted data are within the 95–percent confidence interval, the system can be regarded as being stationary during the course of the experiment. If a significant portion of the predicted data falls outside the 95–percent confidence interval, the system is likely to be non-stationary.[36–39,41,66] Otherwise, if any data point falls outside the 95–percent confidence interval it will be eliminated form the data set. Only the portions of the spectra that are consistent with the Kramers-Kronig relations were used for further analyses.

The results for the Kramers-Kronig consistency check are shown in Figures 4–6 and 4–7. The model predicted every data point within the 95% confidence interval which means that, within the error structure of the measurement, all data can be said to be consistent with Kramers-Kronig relations.

4.3.2 Steady State Experiments at Increasing Temperatures

The same procedure was followed for the steady state experiments where the temperature was increased sequentially. The temperature range studied varied from 60°C to 85°C. Temperatures above 85°C were not analyzed because the behavior

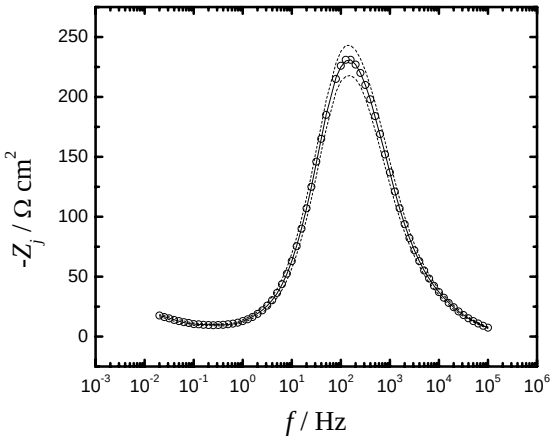

(a)

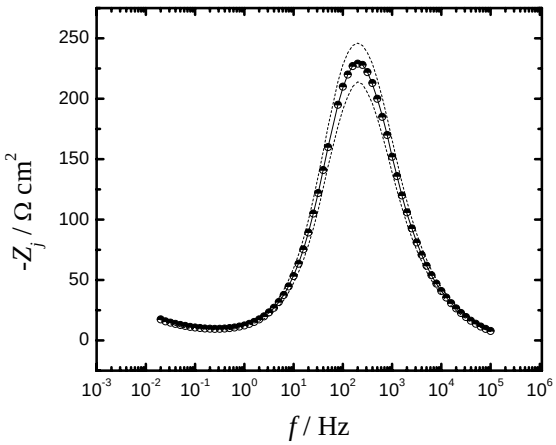

(b)

Figure 4–6: Measurement model fit of the imaginary part of the impedance data for Cell NA–ATi. The open symbols represent measurements taken 15 hours after their preparation. The half-full symbols represent measurements taken approximately 48 hours after the cell preparation. The solid line represents the measurement model fit and the dashed lines represent the 95.4% confidence interval.

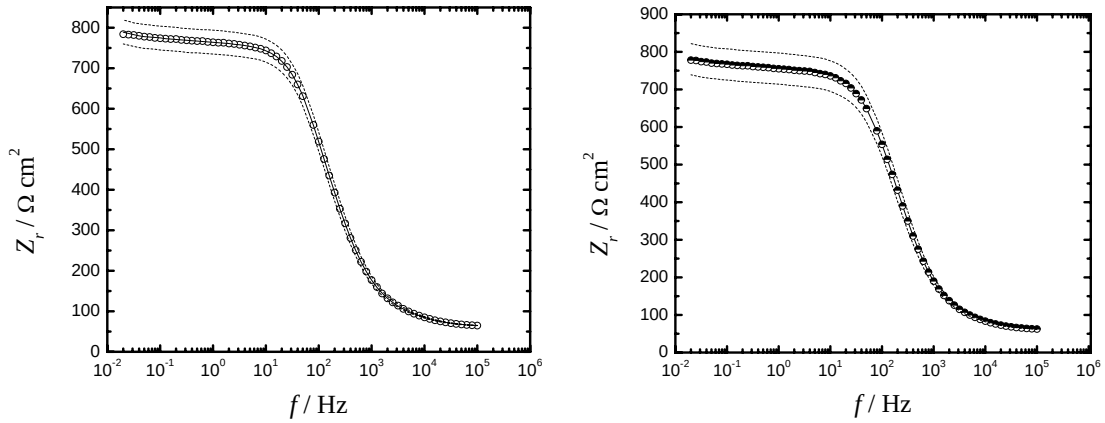

Figure 4–7: Measurement model prediction of the real part of the impedance data for Cell NA–ATi. The open symbols represent measurements taken 15 hours after their preparation. The half-full symbols represent measurements taken approximately 48 hours after the cell preparation. The solid line represents the measurement model prediction and the dashed lines represent the 95.4% confidence interval.

Table 4–2: Error structure models determined for Cell UF-CTe. This cell was exposed to a temperature range varying from 60°C to 85°C.

Temperature (°C)	Error Structure Model
60	$\sigma = 8.7422\text{E}{-4}\lvert Z_r\rvert$
65	$\sigma = 1.4348\text{E}{-3}\lvert Z_j\rvert + 1.1404\text{E}{-3}\lvert Z_r\rvert + 1.1541\text{E}{-5}\lvert Z\rvert^2/R_m$
70	$\sigma = 9.2728\text{E}{-4}\lvert Z_r\rvert + 2.8481\text{E}{-2}$
75	$\sigma = 5.0172\text{E}{-4}\lvert Z_j\rvert + 6.0620\text{E}{-4}\lvert Z_r\rvert$
80	$\sigma = 1.1159\text{E}{-3}\lvert Z_j\rvert + 3.5791\text{E}{-4}\lvert Z_r\rvert$
85	$\sigma = 7.6544\text{E}{-3}\lvert Z_r\rvert$

of the cells was not stable at those temperatures. The error structures for cell UF–CTe are shown in Figure 4–8. These plots show the error structure for the real and imaginary part of the impedance, as well as the error structure model. A good agreement between the model and the experimental data for the 60°C was not possible, however the real and imaginary errors were equal. The error structure models for the six data sets are presented in Table 4–2. These models were calculated using the error structures of the six replicates measured at each temperature. It was not possible to obtain a single model for all the temperatures.

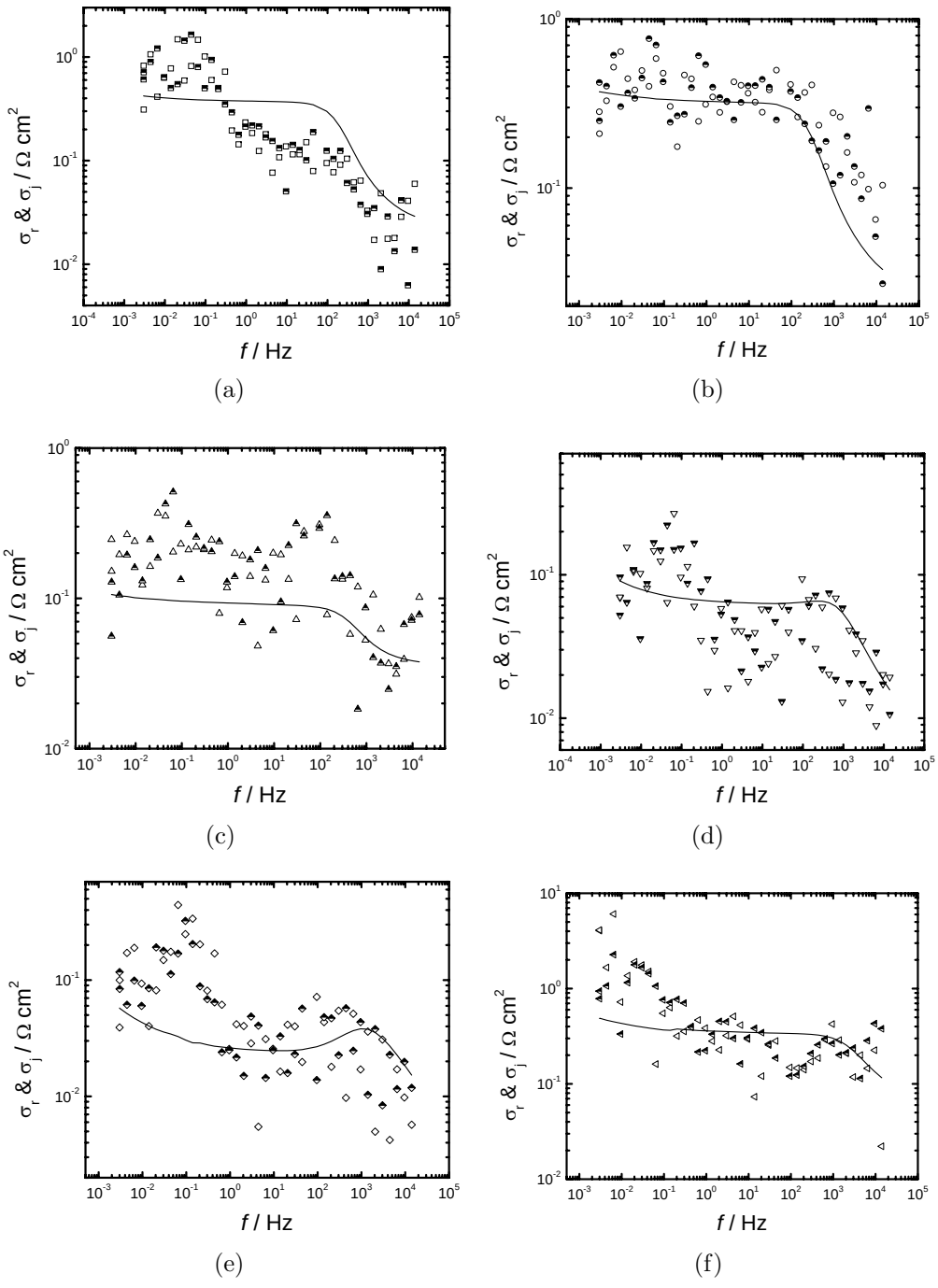

Figure 4–8: Error structure for Cell UF–CTe measurements (a)60°C (b)65°C (c)70°C (d)75°C (e)80°C (f)85°C. The open symbols represent the real part of the impedance. The half-full symbols represent imaginary part of the impedance. The solid line represents the error structure model fit.

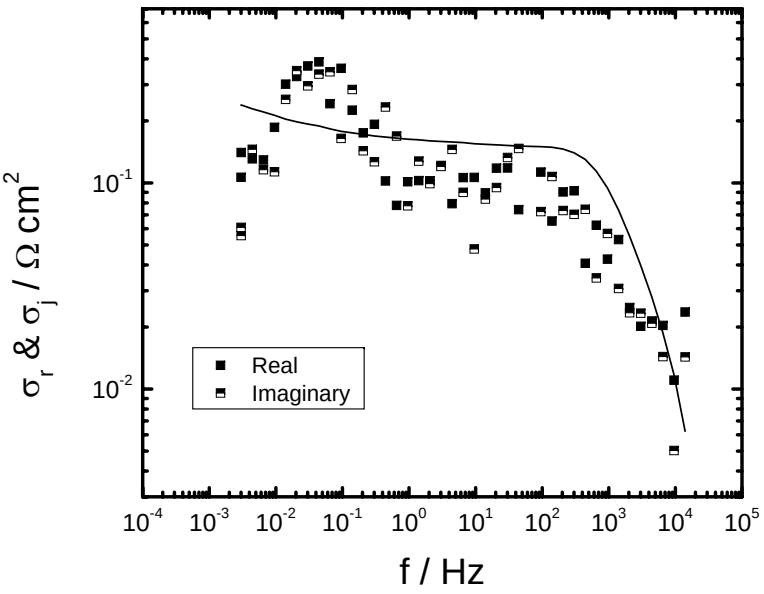

Figure 4–9: Error structure for Cell NA–ATi measurements taken 15 and 48 hours after their preparation, respectively. The open symbols represent the real part of the impedance. The half-full symbols represent imaginary part of the impedance. The solid line represents the error structure model fit.

All data points in the set were consistent with Kramers-Kronig relations. The same procedure was repeated for Cells UF–BTe and UF–FTe.

4.3.3 Transient Experiments at Constant Temperature

This analysis was very important for the transient experiments. The analysis helped us identify which portions of the spectra were consistent with the Kramers-Kronig relations and could be used to identify meaningful parameters as functions of time. This analysis also helped identify how much time was needed to reach steady state conditions. The error structures for cell UF–DTi are shown in Figure 4–9. This plot shows the error structure for the real and imaginary part of the impedance, as well as the error structure model. The error structure model was calculated to be

$$\sigma = 0.00058896 Z_j + 0.0016651(Z_r - 29.00) \tag{4.3}$$

This model was calculated using the error structures of the ten of the twenty–four measurements.

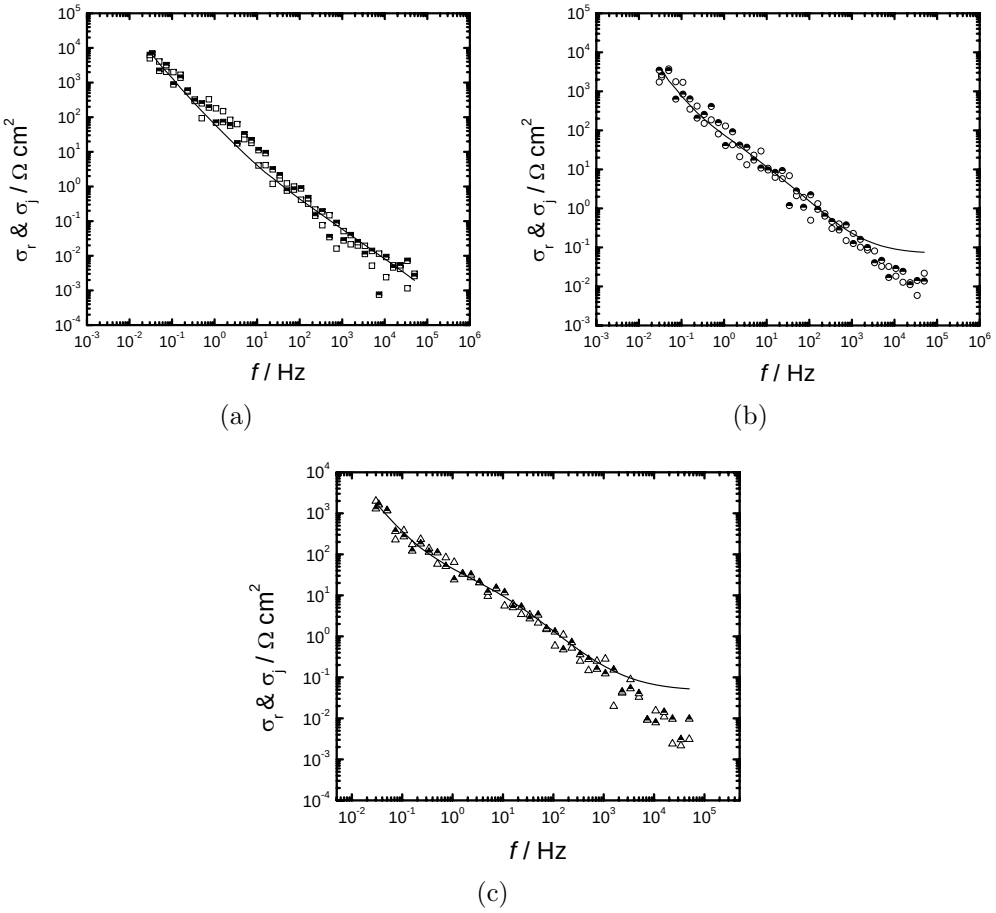

Figure 4–10: Error structure for Cell NA–AB measurements (a)80°C (b)90°C (c)100°C. The open symbols represent the real part of the impedance. The half-full symbols represent imaginary part of the impedance. The solid line represents the error structure model fit.

4.3.4 Blocking Electrodes

This analysis was also done for the blocking electrode measurements. The error structure models for cell NA–AB are shown in Figure 4–10 and in Table 4–3. These models were calculated using the error structures of the six replicates measured at each temperature.

This procedure was repeated for every data set. Data point found to be inconsistent with the Kramers–Kronig relations were not considered for further analysis.

Table 4–3: Error structure models determined for Cell NA–AB. This cell was exposed to a temperature range varying from 80°C to 100°C at 10°C intervals.

Temperature (°C)	Error Structure Model
80	$\sigma = 3.6053\text{E}{-4}\|Z_j\| + 1.7754\text{E}{-7}\|Z\|^2/R_m$
90	$\sigma = 4.5841\text{E}{-3}\|Z_r\| + 1.9697\text{E}{-7}\|Z\|^2/R_m$
100	$\sigma = 4.3598\text{E}{-3}\|Z_r\| + 1.8417\text{E}{-7}\|Z\|^2/R_m$

CHAPTER 5
EXPERIMENTAL RESULTS AND PRELIMINARY ANALYSIS

Bode plots and complex-impedance-plane plots are the typical graphical representations when a specific model is not postulated. However, additional plots, like IR-corrected Bode plots, log-log plots of the imaginary component of the impedance, and effective capacitance plots can provide guidance for the development of appropriate physical models.

Equivalent circuit models had been published in the literature that provide adequate fits to the impedance data. For example, R. Bouchet, S. Lascaud, and M. Rosso developed an equivalent circuit for the Li|PEO-LiTFSI system, as shown in Figure 5–1.[63] Their work was focused on the evolution of the impedance spectra of symmetric cells, Li|PEO-LiTFSI|Li, with aging time at 90°C. In their experimental results, they distinguish four frequency domains,

1. $f > 10^5$ Hz: corresponds to the bulk of the electrolyte. This part of the spectra was perturbed by high frequency inductive effects due to connections.
2. 10^5–10^2 Hz: attributed to the formation of a surface layer.
3. 10^2–10.1 Hz: not very reproducible.

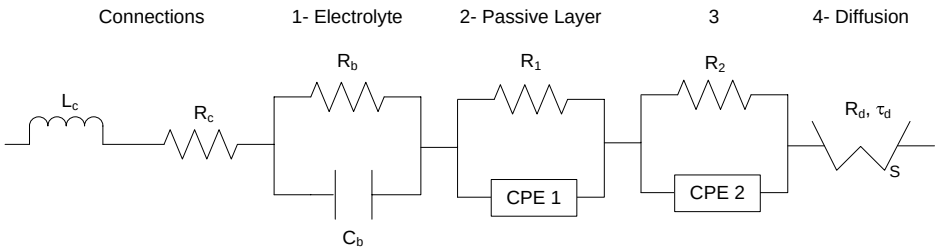

Figure 5–1: Equivalent circuit model used to fit the impedance data obtained from the Li|PEO-LiTFSI system. Figure reproduced from: R. Bouchet, S. Lascaud, and M. Rosso. An EIS Study of the Anode Li|PEO-LiTFSI of a Li Polymer Battery. Journal of Electrochemical Society. Vol. 150, No. 10, pp.A1385–A1389, 2003.

4. 10.1–$10^{-}4$ Hz: Warburg impedance characteristic of the transport of charged particles.

The proposed equivalent circuit assumed that the phenomena corresponding to the four frequency domains are in series. The authors claimed that the proposed model can reproduce his experimental data.

The graphical analysis presented in this section can help accept or reject models like the one proposed by R. Bouchet, S. Lascaud, and M. Rosso. In this section we use graphical analyses to obtain an understanding of the physics of the system.

5.1 Steady State Experiments at Constant Temperature

The traditional Nyquist representation of the impedance data obtained from Cell NA–ATi are shown in Figure 3–4 and 3–6. The measurements were made approximately 15 and 48 hours after the cell preparation. The six impedance replicates at each time are presented in this plot. The electrolyte resistance value obtained from this plot is 62.0 Ω–cm^2 for the first data set and 59.7 Ω–cm^2 for the second. The shape of the Nyquist plot indicates that the system have characteristic time constants distributed over a wide–range of time scales.

The alternate real and imaginary representations are presented in Figure 3–7. The slopes at intermediate and high frequency were calculated for the imaginary representation. The slopes at intermediate and high frequency were in good agreement for the six replicates. These slopes have the value of $\pm(1-\alpha)$, and departure from ± 1 provides indication of distributed processes. A reduction in the values of α at intermediate frequency and an increase in the values of α at high frequency were evident for the measurements taken 48 hours after the cell preparation. A line with average slope of 0.74 ± 0.0086 was fitted to the intermediate frequency for the first data set and a line with average slope 0.70 ± 0.0117 was fitted for the second data set. A line with average slope -0.62 ± 0.0081

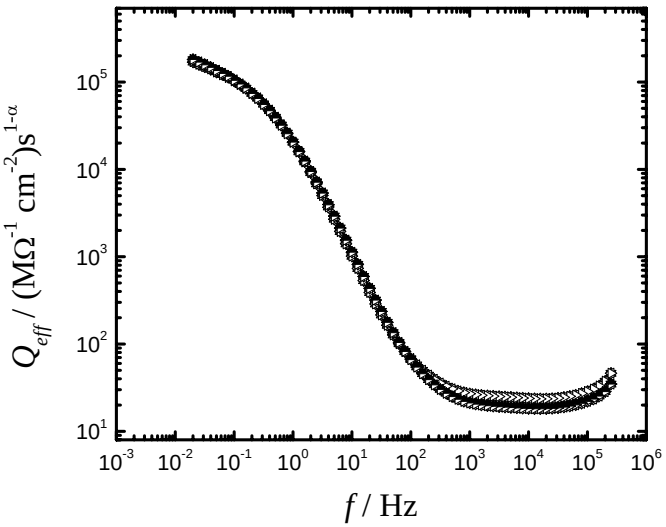

Figure 5–2: Effective CPE coefficient defined by equation (5.1) for Cell NA–ATi. The open symbols represent measurements taken approximately 15 hours after the cell preparation. The half–full symbols represent measurements taken approximately 48 hours after the cell preparation.

was fitted to the first data set at high frequency and a line with average slope -0.64 ± 0.0091 was fitted to the second data set. The difference in these two slopes indicates that more than one capacitive time constant can be distinguished in the system. The value of α can be used to obtain an apparent constant phase element (CPE) coefficient Q_{eff}

$$Q_{\text{eff}} = \frac{cos(\frac{\alpha\pi}{2})}{-Z_j(f) * (2\pi f)^{1-\alpha}} \tag{5.1}$$

The resulting values of the Q_{eff} are presented in Figure 5–2. The absence of a clearly identifiable asymptote may be attributed to high–frequency instrumental artifacts. The last ten points at high frequency were disregarded because it is believed that they were corrupted by such instrumental artifacts. The value for the CPE coefficient provided in Table 5–2 represents the average over the values for the remaining 10 highest frequencies.

The value of α can also be used to find the solution resistance R_e used in

$$\phi^* = tan^{-1}(\frac{Z_j}{Z_r - R_e}) \tag{5.2}$$

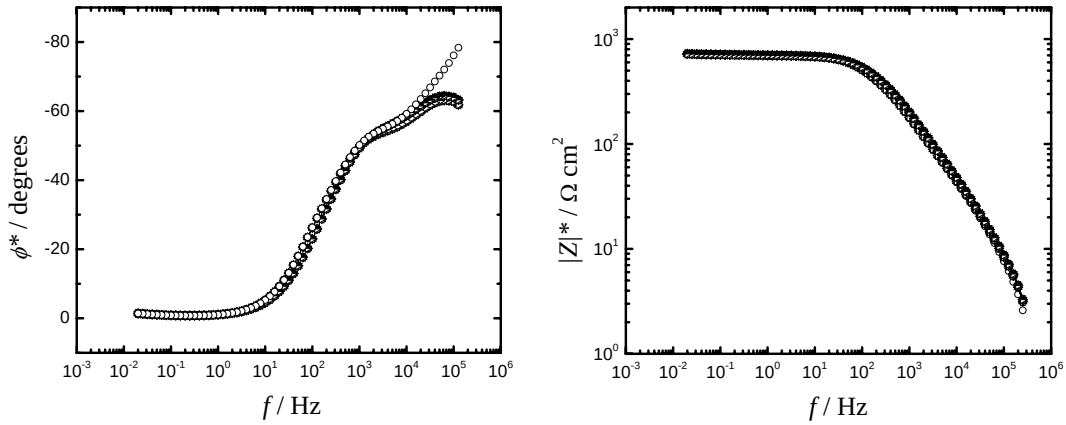

Figure 5–3: IR-corrected Bode plots for Cell NA–ATi; a) phase angle, b) modulus. The open symbols represent measurements taken approximately 15 hours after the cell preparation. The half–full symbols represent measurements taken approximately 48 hours after the cell preparation.

to yield the expected asymptotic value for adjusted phase angle given by

$$\phi^*(\infty) = -90(1-\alpha) \tag{5.3}$$

The electrolyte resistance can also be used to obtain the adjusted magnitude of the impedance as shown in

$$|Z|^* = \sqrt{(Z_r - R_{e,est})^2 + (Z_j)^2} \tag{5.4}$$

The IR–corrected phase angle and magnitude as a function of frequency are presented in Figure 5–3. The value of the electrolyte resistance obtained from this method was approximately 61.2 ± 0.841 Ω–cm^2 for the first data set and approximately 58.6 ± 0.011 Ω–cm^2 for the second. These values are in good agreement with the ones obtained from the Nyquist plot. Also, the high-frequency slope in the magnitude of the impedance plot was equal to the slope used to calculate the α value.

Table 5–1: Average α values obtained using graphical techniques at the intermediate frequency range for Cell NA–ATi through NA–DTi. Six replicates were used to calculate the average parameters

Measurement Time / h	15	48
NA–ATi	0.26 ± 0.009	0.30 ± 0.012
NA–BTi	$0.35 - 0.31$	0.37 ± 0.0002
NA–CTi	0.28 ± 0.004	0.39 ± 0.0002
NA–DTi	0.31 ± 0.007	$0.38 - 0.36$

Table 5–2: Average values of the parameters obtained using graphical techniques at the high frequency range for Cell NA–ATi trough NA–DTi. Six replicates were used to calculate the average parameters

	Measurement Time / h	15	48
NA–ATi	α / dimensionless	0.38 ± 0.008	0.36 ± 0.009
	Q_{eff} / $M\Omega^{-1}$ cm^{-2} $s^{1-\alpha}$	24.8 ± 0.801	18.9 ± 0.010
	R_e / Ω cm^2	61.2 ± 0.841	58.6 ± 0.011
NA–BTi	α / dimensionless	0.37 ± 0.011	0.35 ± 0.002
	Q_{eff} / $M\Omega^{-1}$ cm^{-2} $s^{1-\alpha}$	22.6 ± 1.581	17.8 ± 0.452
	R_e / Ω cm^2	61.7 ± 0.048	59.8 ± 0.021
NA–CTi	α / dimensionless	0.42 ± 0.017	0.39 ± 0.006
	Q_{eff} / $M\Omega^{-1}$ cm^{-2} $s^{1-\alpha}$	27.6 ± 0.079	27.6 ± 0.833
	R_e / Ω cm^2	49.2 ± 0.019	44.2 ± 0.036
NA–DTi	α / dimensionless	0.35 ± 0.007	0.36 ± 0.003
	Q_{eff} / $M\Omega^{-1}$ cm^{-2} $s^{1-\alpha}$	$27.7 - 23.9$	20.0 ± 0.875
	R_e / Ω cm^2	41.8 ± 0.016	45.6 ± 0.018

The same procedure was applied to Cells NA–BTi through NA–DTi. A summary of the parameters obtained from Cells NA–ATi through NA–DTi are presented in Tables 5–1 and 5–2.

In general, the average result of the α value for the high frequency range was 0.37 ± 0.005 and 0.33 ± 0.040 for the intermediate frequency range. More variability was observed in the value of α at intermediate frequency than at high frequency. Also, the value of the effective capacitance, for the four cells, decreased with time.

5.2 Steady State Experiments at Increasing Temperatures

Nyquist and Bode representations of the impedance data obtained from Cell UF–CTe are shown in Figures 5–4 and 5–5, respectively. The temperature range

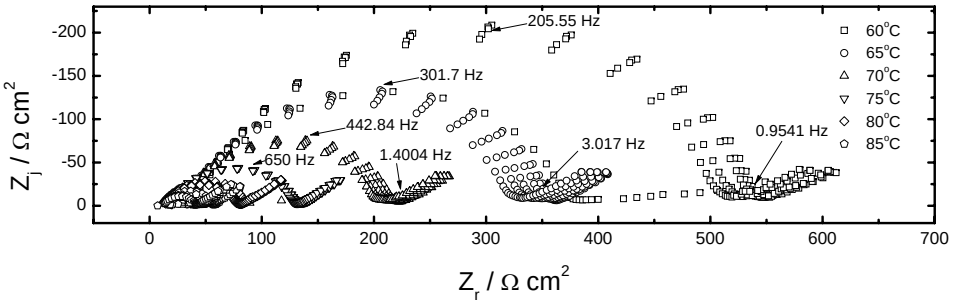

Figure 5–4: Impedance-plane or Nyquist representation of impedance data for Cell UF–CTe with temperature as a parameter. Six replicates of each measurement are presented for each temperature.

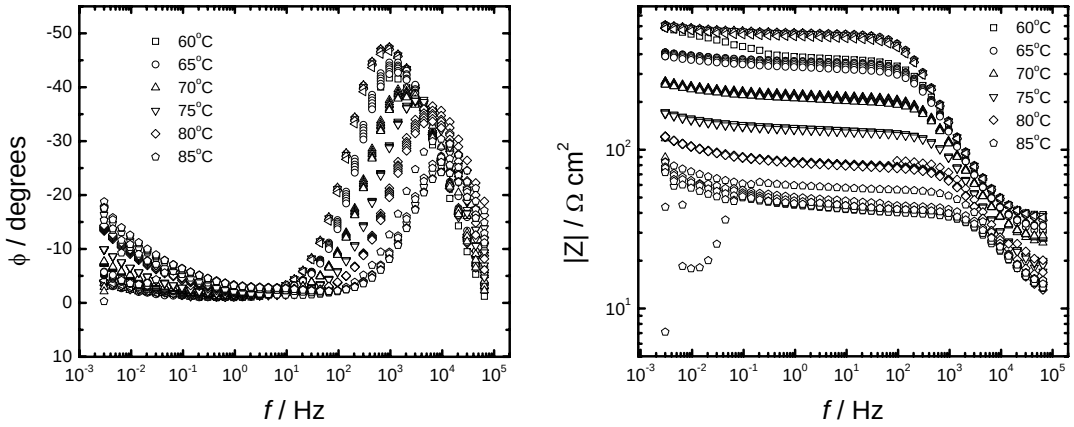

(a) (b)

Figure 5–5: Bode Representation of impedance data for phase angle and magnitude for Cell UF–CTe, respectively, with temperature as a parameter. Six replicates of each measurement are presented for each temperature.

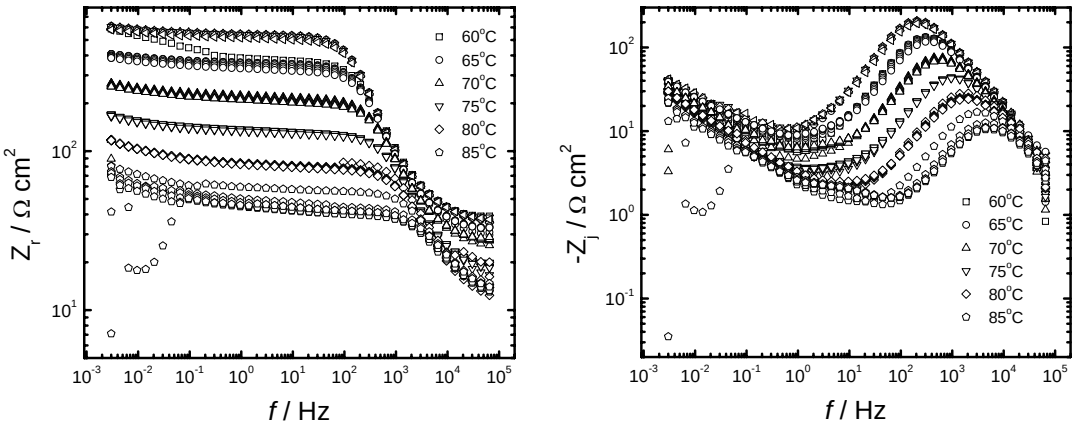

(a) (b)

Figure 5–6: Plots of the imaginary and real part of the impedance as functions of frequency for Cell UF–CTe with temperature as a parameter. Six replicates of each measurement are presented for each temperature.

Table 5–3: Average values of the low frequency tail slopes from cells UF–BTe, UF–CTe, and UF–FTe. Six replicates were used to calculate the average parameters.

Temp. / °C	UF–BTe	UF–CTe	UF–FTe
60	0.333 ± 0.01	0.298 ± 0.01	0.296 ± 0.01
65	0.351 ± 0.02	0.321 ± 0.02	0.337 ± 0.02
70	0.396 ± 0.13	0.342 ± 0.13	0.351 ± 0.13
75	0.391 ± 0.01	0.411 ± 0.01	0.399 ± 0.01
80	0.389 ± 0.01	0.387 ± 0.01	0.343 ± 0.01
85	0.408 ± 0.02	0.338 ± 0.02	0.388 ± 0.02

analyzed was 60°C to 85°C in intervals of 5°C. Six impedance replicates at each temperature are presented in this plot. The Nyquist plot represents a system with characteristic time constant distributed over a wide-range of time scales.

The real and imaginary representations are presented in Figure 5–6. The slope of the low frequency tail increased with temperature from a value of 0.298 ± 0.01 at 60°C, to 0.411 ± 0.01 at 75°C, and decreased to 0.338 ± 0.02 at 85°C. A similar behavior was observed in cells UF–BTe and UF–FTe. The average values of the low frequency tail slopes are presented in Figure 5–7 and Table 5–3. The average slopes of the imaginary representation at intermediate decreased with increasing temperature as shown in Figure 5–8. At high frequencies, the average sloped of

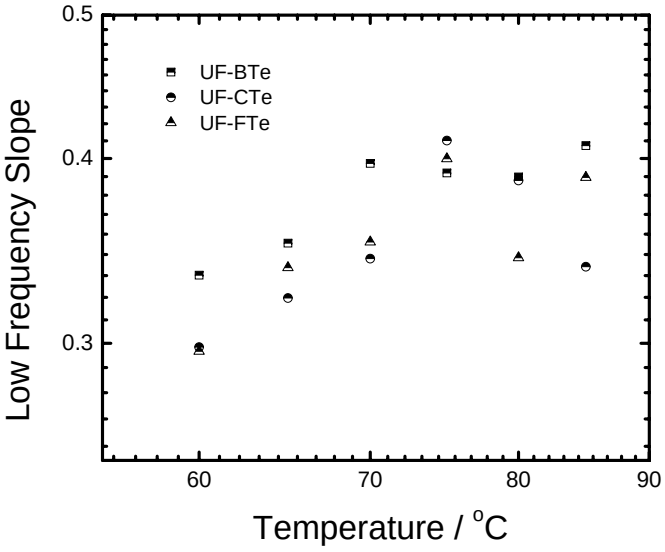

Figure 5–7: Average values of the low frequency tail slopes from cells UF–BTe, UF–CTe, and UF–FTe. Six replicates were used to calculate the average parameters.

Table 5–4: Slopes obtained using graphical techniques at the intermediate frequency range from cells UF–BTe, UF–CTe, and UF–FTe. Six replicates were used to calculate the average parameters

Temp. / °C	UF–BTe	UF–CTe	UF–FTe
60	0.826 ± 0.006	0.759 ± 0.020	0.626 ± 0.072
65	0.835 ± 0.003	0.747 ± 0.031	0.663 ± 0.036
70	0.780 ± 0.018	0.720 ± 0.033	0.707 ± 0.019
75	0.786 ± 0.018	0.711 ± 0.016	0.693 ± 0.022
80	0.772 ± 0.003	0.712 ± 0.028	0.622 ± 0.017
85	0.737 ± 0.011	0.677 ± 0.035	0.611 ± 0.070

the imaginary representation remain constant until a temperature of 75°C was reached and then decreased as shown in Figure 5–9. The average results obtained for all the cells are presented in Tables 5–4 and 5–5. The slope of the imaginary representation at high frequency range varies from -0.69 ± 0.05 to -0.74 ± 0.01, which corresponds to α values ranging from 0.31 to 0.26. The difference in the slope at intermediate and high frequency was smaller in these experiments.

The value of Q_{eff} at high frequency was calculated and the resulting values are presented in Figure 5–10. The five highest frequencies points were disregarded

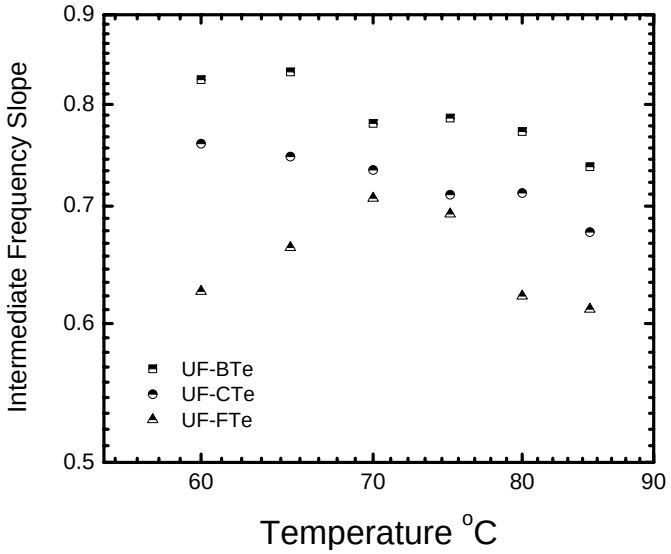

Figure 5–8: Average values of the intermediate frequency tail slopes from cells UF–BTe, UF–CTe, and UF–FTe. Six replicates were used to calculate the average parameters.

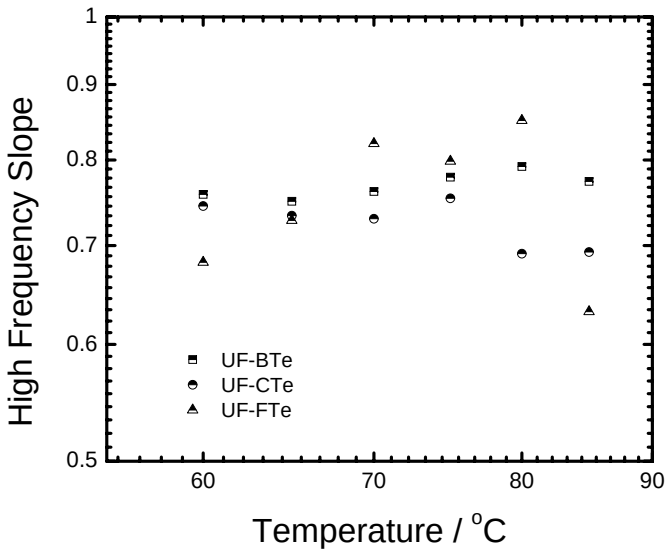

Figure 5–9: Average values of the high frequency tail slopes from cells UF–BTe, UF–CTe, and UF–FTe. Six replicates were used to calculate the average parameters.

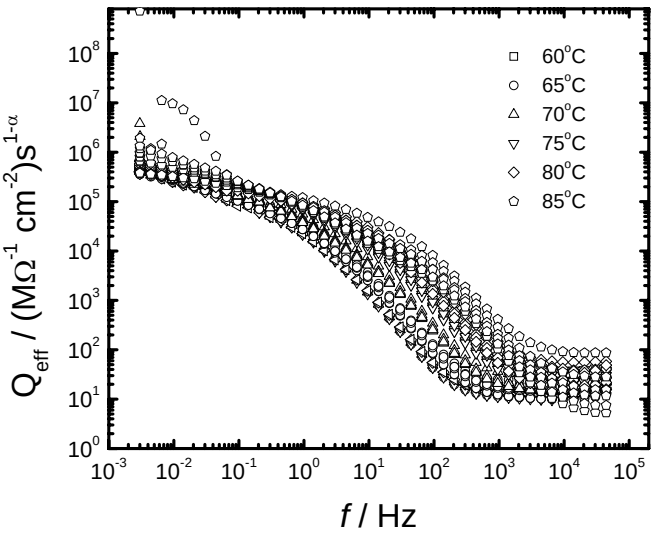

Figure 5–10: Effective CPE coefficient defined by equation (5.1) for Cell UF–CTe. Six replicates of each measurement are presented for each temperature.

because they were believed to be corrupted by instrument artifacts. The values for the apparent CPE coefficient provided in Table 5–5 represents the average over the values for the remaining 5 highest frequencies. The value of Q_{eff} seems to reach a maximum around 75°C. There is also more variability in this value as the temperature increased. We were not able to calculate a meaningful average value of Q_{eff} for cell UF–FTe.

The solution resistance R_e, the corrected phase angle, and the corrected impedance magnitude were calculated. The IR–corrected phase angle and magnitude are presented in Figure 5–11. The slope of the high frequency asymptote has a value of $1 - \alpha$. The values for the electrolyte resistance are provided in Table 5–5. These values are in good agreement with the values obtained using the impedance plane representation.

5.3 Transient Experiments at Constant Temperature

Impedance-plane and Bode representations obtained from Cell UF–DTr are shown in Figures 5–12 and 5–13, respectively. The temperature was held constant at 70°C throughout the experiment. Impedance spectra were taken every 30

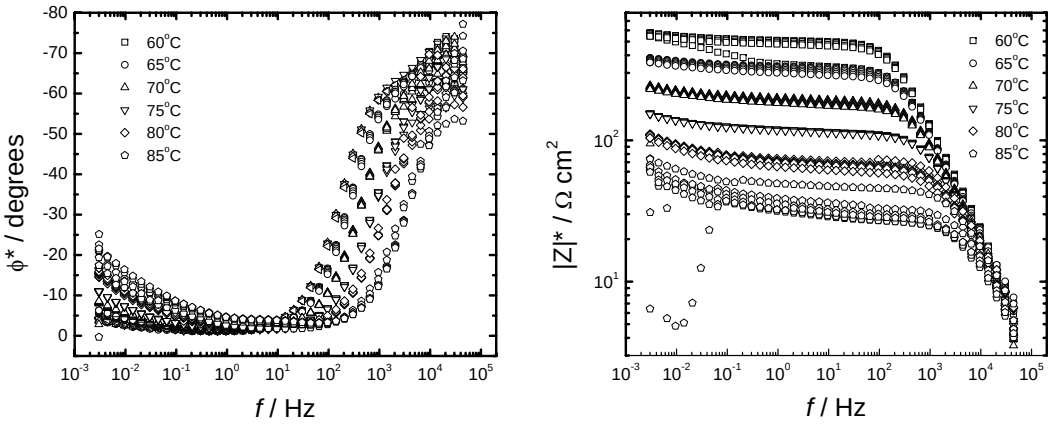

(a) (b)

Figure 5–11: IR-corrected Bode plots for Cell UF–CTe; (a) phase angle, (b) modulus. Six replicates of each measurement are presented for each temperature.

Table 5–5: Average values of the parameters obtained using graphical techniques at the high frequency range from cells UF–BTe, UF–CTe, and UF–FTe. Six replicates were used to calculate the average parameters

Temp. / °C		UF–BTe	UF–CTe	UF–FTe
60	α	0.24 ± 0.01	0.26 ± 0.01	0.32 ± 0.01
	Q_{eff} / $\text{M}\Omega^{-1}$ $\text{cm}^{-2}\text{s}^{1-\alpha}$	11.60 ± 1.15	12.98 ± 1.54	24.70 ± 2.05
	R_e / Ω cm^2	37.18 ± 2.55	37.35 ± 1.22	50.38 ± 1.23
65	α	0.25 ± 0.02	0.27 ± 0.04	0.27 ± 0.05
	Q_{eff} / $\text{M}\Omega^{-1}$ $\text{cm}^{-2}\text{s}^{1-\alpha}$	14.06 ± 2.23	16.69 ± 5.33	21.69 ± 11.76
	R_e / Ω cm^2	30.34 ± 0.67	32.25 ± 1.60	38.96 ± 1.80
70	α	0.24 ± 0.1	0.27 ± 0.03	0.18 ± 0.10
	Q_{eff} / $\text{M}\Omega^{-1}$ $\text{cm}^{-2}\text{s}^{1-\alpha}$	13.27 ± 1.87	19.43 ± 4.94	15.27 ± 20.94
	R_e / Ω cm^2	24.29 ± 1.05	27.77 ± 1.11	32.60 ± 3.57
75	α	0.22 ± 0.01	0.31 ± 0.02	0.20 ± 0.01
	Q_{eff} / $\text{M}\Omega^{-1}$ $\text{cm}^{-2}\text{s}^{1-\alpha}$	11.78 ± 1.20	29.09 ± 6.74	23.30 ± 26.85
	R_e / Ω cm^2	20.04 ± 1.22	18.85 ± 0.97	26.21 ± 1.53
80	α	0.21 ± 0.01	0.31 ± 0.05	0.15 ± 0.04
	Q_{eff} / $\text{M}\Omega^{-1}$ $\text{cm}^{-2}\text{s}^{1-\alpha}$	10.02 ± 1.22	32.90 ± 15.72	10.81 ± 4.16
	R_e / Ω cm^2	13.16 ± 0.50	15.15 ± 2.69	24.64 ± 1.23
85	α	0.26 ± 0.01	0.25 ± 0.10	0.37 ± 0.03
	Q_{eff} / $\text{M}\Omega^{-1}$ $\text{cm}^{-2}\text{s}^{1-\alpha}$	13.68 ± 1.34	26.09 ± 30.94	222.12 ± 126.0
	R_e / Ω cm^2	11.14 ± 0.36	14.16 ± 0.78	19.40 ± 2.08

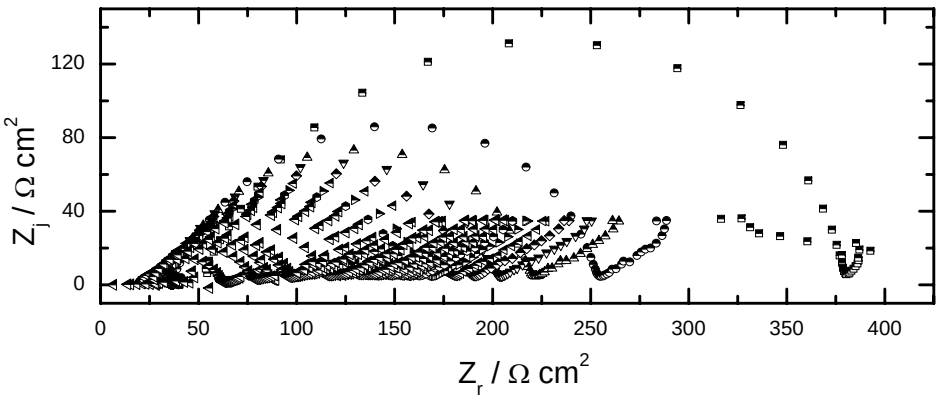

Figure 5–12: Impedance-plane or Nyquist representation of impedance data for Cell UF–DTr with temperature as a parameter. Impedance spectra were taken every 30 seconds for 48 hours, it took approximately two hours to complete one spectrum.

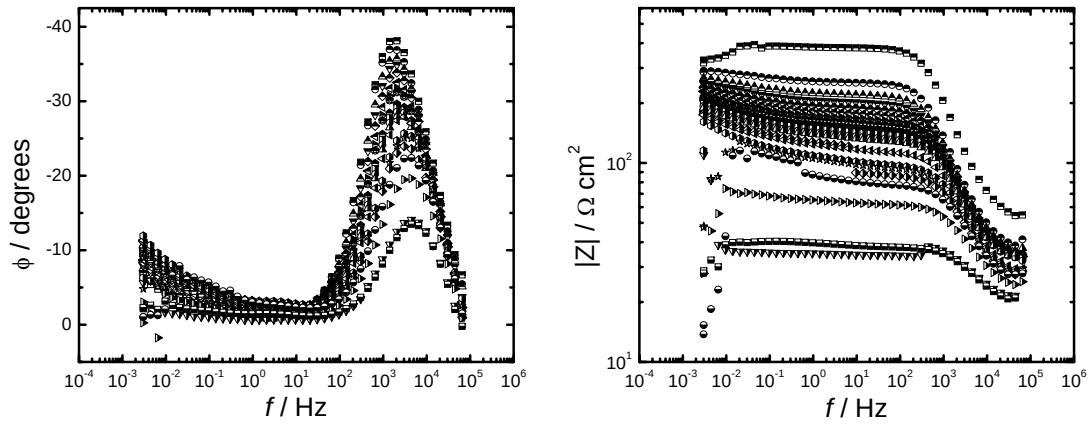

(a) (b)

Figure 5–13: Bode Representation of impedance data for phase angle and magnitude for Cell UF–DTr, respectively. Impedance spectra were taken every 30 seconds for 48 hours, it took approximately two hours to complete one spectrum.

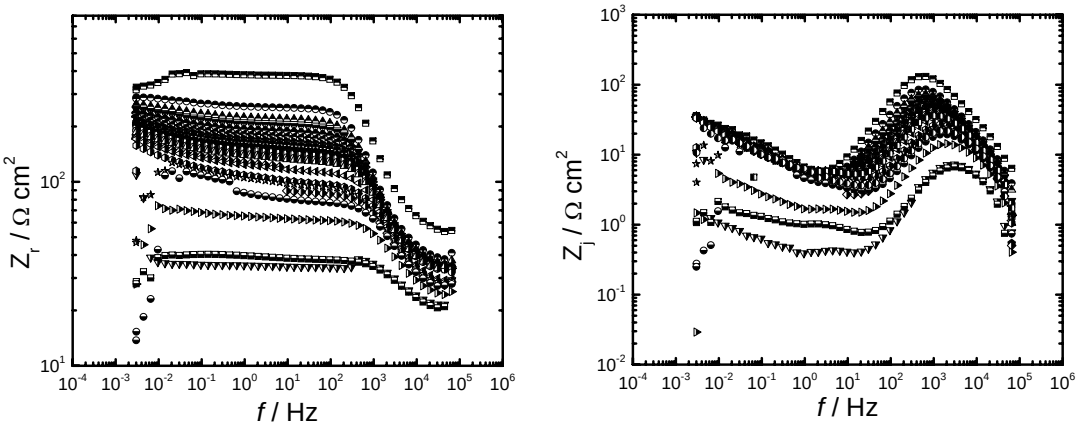

(a) (b)

Figure 5–14: Plots of the imaginary and real part of the impedance as functions of frequency for Cell UF–DTr. Impedance spectra were taken every 30 seconds for 48 hours, it took approximately two hours to complete one spectrum.

seconds for 48 hours, it took approximately two hours to complete one spectrum. The Nyquist plot reveals a depressed semicircle.

The real and imaginary representations are presented in Figure 5–14. The slope of the low frequency tail decreased with time from a value of 0.35 ± 0.02 to 0.24 ± 0.01. However, the low frequency tail slopes for cell UF–ETr varied randomly from 0.38 ± 0.04 to 0.30 ± 0.03. This discrepancy can be attributed to the fact that the melting point of the electrolyte is approximately 60°C, thus there is more instability in the system at that temperature. The average values of the low frequency tail slopes are presented in Table 5–6. The slopes of the imaginary representation at intermediate frequencies decrease with time and the slope at high frequencies oscillate with time between -0.74 and -0.79, which correspond to α values ranging from 0.26 to 0.21. The average results obtained from Cell UF–DTr and UF–ETr are presented in Table 5–7 and 5–8. In this experiment the slope at intermediate and high frequency were different, suggesting that more than one CPE are affecting the system. This result is in agreement with previous experiments.

Table 5–6: Values of the low frequency tail slopes from Cell UF–DTr and UF–ETr.

No.	UF–DTr	UF–ETr
2	0.35 ± 0.02	0.35 ± 0.02
3	0.33 ± 0.02	0.37 ± 0.04
4	0.33 ± 0.02	0.35 ± 0.02
5	0.33 ± 0.01	0.37 ± 0.02
6	0.31 ± 0.01	0.32 ± 0.04
7	0.32 ± 0.01	0.36 ± 0.03
8	0.31 ± 0.01	0.38 ± 0.04
9	0.30 ± 0.01	0.34 ± 0.03
10	0.28 ± 0.01	0.30 ± 0.03
19	0.24 ± 0.01	0.36 ± 0.06

Table 5–7: Values of the low and intermediate frequency tail slopes obtained from Cell UF–DTr and UF–ETr.

No.	UF–DTr	UF–ETr
2	0.83 ± 0.01	0.79 ± 0.01
3	0.82 ± 0.01	0.74 ± 0.01
4	0.81 ± 0.01	0.72 ± 0.01
5	0.81 ± 0.01	0.69 ± 0.02
6	0.79 ± 0.01	0.67 ± 0.02
7	0.79 ± 0.01	0.65 ± 0.03
8	0.77 ± 0.02	0.64 ± 0.03
9	0.78 ± 0.01	0.62 ± 0.03
10	0.77 ± 0.01	0.61 ± 0.03
19	0.72 ± 0.02	0.42 ± 0.05

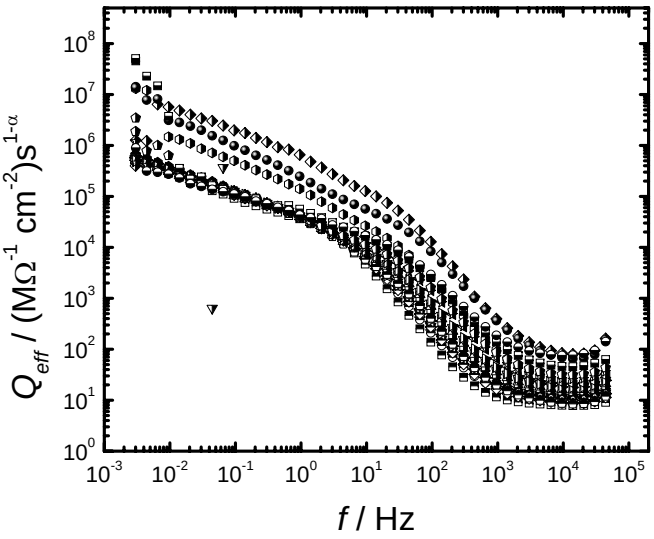

Figure 5–15: Effective CPE coefficient defined by equation (5.1) for Cell UF–DTr.

The value of Q_{eff} at high frequency was calculated and the resulting values are presented in Figure 5–15. The value for the apparent CPE coefficient provided in Table 5–8 represents the average over the highest frequencies values.

The solution resistance R_e, the corrected phase angle, and the corrected impedance magnitude were calculated. The IR–corrected phase angle and magnitude are presented in Figure 5–16. The slope of the high frequency asymptote has a value of $1 - \alpha$. The values for the electrolyte resistance are provided in Table 5–8. These values are in good agreement with the values obtained using the impedance plane representation.

5.4 Conclusions

The plots presented here provide useful guides to model development. The difference in the slopes at intermediate and high frequencies in the plots of the imaginary component of the impedance suggest that more than one capacitive time constant can be identified in the system. The high-frequency capacitive loop can be attributed to a dielectric behavior of the electrolyte or to reactions at the lithium metal surface. This means that an equivalent circuit such as the one proposed by

Table 5–8: Average values of the parameters obtained using graphical techniques at the high frequency range for Cell UF–DTr.

No.		UF–DTr	UF–ETr
2	α	0.26	0.32
	Q_{eff} / $\text{M}\Omega^{-1}$ $\text{cm}^{-2}\text{s}^{1-\alpha}$	12.52	21.39
	R_e / Ω cm^2	35.48	60.24
3	α	0.26	0.30
	Q_{eff} / $\text{M}\Omega^{-1}$ $\text{cm}^{-2}\text{s}^{1-\alpha}$	13.95	20.62
	R_e / Ω cm^2	33.36	68.65
4	α	0.24	0.29
	Q_{eff} / $\text{M}\Omega^{-1}$ $\text{cm}^{-2}\text{s}^{1-\alpha}$	12.01	23.16
	R_e / Ω cm^2	32.90	60.61
5	α	0.21	0.29
	Q_{eff} / $\text{M}\Omega^{-1}$ $\text{cm}^{-2}\text{s}^{1-\alpha}$	9.40	24.90
	R_e / Ω cm^2	33.05	59.66
6	α	0.23	0.29
	Q_{eff} / $\text{M}\Omega^{-1}$ $\text{cm}^{-2}\text{s}^{1-\alpha}$	11.80	31.89
	R_e / Ω cm^2	33.43	63.53
7	α	0.22	0.30
	Q_{eff} / $\text{M}\Omega^{-1}$ $\text{cm}^{-2}\text{s}^{1-\alpha}$	10.87	23.74
	R_e / Ω cm^2	33.23	56.37
8	α	0.22	0.29
	Q_{eff} / $\text{M}\Omega^{-1}$ $\text{cm}^{-2}\text{s}^{1-\alpha}$	11.25	26.59
	R_e / Ω cm^2	32.60	57.14
9	α	0.23	0.30
	Q_{eff} / $\text{M}\Omega^{-1}$ $\text{cm}^{-2}\text{s}^{1-\alpha}$	13.08	23.86
	R_e / Ω cm^2	31.80	60.56
10	α	0.19	0.31
	Q_{eff} / $\text{M}\Omega^{-1}$ $\text{cm}^{-2}\text{s}^{1-\alpha}$	9.42	25.76
	R_e / Ω cm^2	33.43	54.57
19	α	0.29	0.30
	Q_{eff} / $\text{M}\Omega^{-1}$ $\text{cm}^{-2}\text{s}^{1-\alpha}$	28.05	39.37
	R_e / Ω cm^2	26.59	56.12

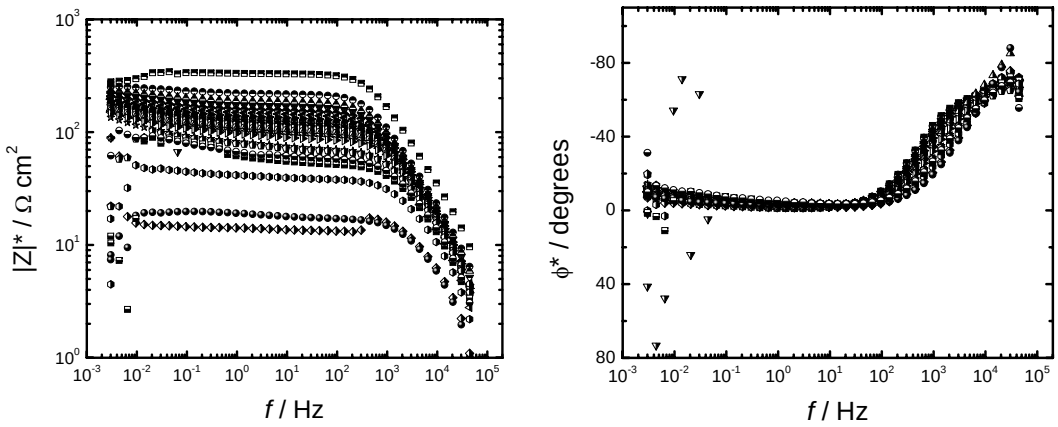

(a) (b)

Figure 5–16: IR-corrected Bode plots for Cell UF–DTr; a) phase angle, b) modulus.

Bouchet *et al.* may describe the system correctly if the capacity loop is attributed to a dielectric behavior of the electrolyte.

The decrease of the impedance response with time is consistent with dissolution of native oxide layers on the lithium surface, as proposed in the literature. The results showed that the time required for complete dissolution of the oxide layers were on the order of several days. As the temperature of the cells was increased the impedance response decreased. This result is consistent with either hypothesis, the high-frequency capacitive loop is due to reactions at the lithium metal surface or due to a dielectric behavior of the electrolyte.

CHAPTER 6
BLOCKING ELECTRODE ANALYSIS

The impedance data presented in Chapter 5 were obtained using two lithium electrodes in a symmetric configuration. To explore the hypothesis that the high-frequency capacitive loop seen in the impedance spectra were associated with the dielectric response of the electrolyte, a second set of experiments was performed using stainless steel electrodes, again in a symmetric configuration.

6.1 Experimental Results

Impedance measurements were obtained at four different temperatures. The results obtained at 25°C, 80°C, 90°C, and 100°C are presented in Figure 6–1 with temperature as a parameter. The results indicate that the steel electrodes acted as blocking electrodes with a local capacity dispersion. The local capacity dispersion can be caused by roughness on the electrode surface.

At low frequencies, the impedance response of the steel electrodes can be expressed as

$$Z(f) = R_e + \frac{1}{(j2\pi f)^{\alpha} Q} \tag{6.1}$$

where the parameters α and Q are constants. When $\alpha = 1$, Q represents the capacitance of the double layer. When $\alpha \neq 1$, the system shows behavior that has been attributed to surface heterogeneity. At high frequencies, the data show a dispersion that may be associated with a non-uniform current and potential distribution.

6.2 Graphical Analysis

Huang *et al.*[67] developed a mathematical model for a blocking disk electrode embedded in an infinite insulating plane. The mathematical model involves solving

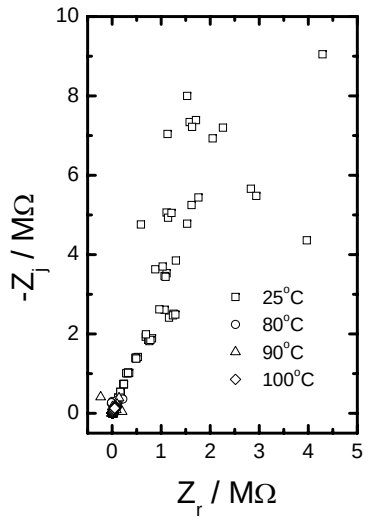

Figure 6–1: Complex impedance plane or Nyquist representation for the response of a 430 Stainless Steel disk in PEO/LiTSFI electrolyte with concentration as a parameter. Six replicates of each measurement are presented for each temperature.

Laplace's equation for potential in the frequency domain. Their work provides a guide for analysis of impedance data that is similar to the one explained in Chapter 5.

The real and imaginary representations are presented in Figure 6–2 as functions of temperature. The difference in the response between the experiments done at 25°C and the ones done at 80°C, 90°C, and 100°C can be attributed to the change in conductivity associated with the melting point of the electrolyte, approximately 60°C.

A value for the solution conductivity was extracted from the real part of the impedance following

$$\kappa = \left[4r_0 \lim_{f \to \infty} Z_r \right]^{-1} \tag{6.2}$$

The real parts of the impedance corresponding to the values obtained from equation (6.2) are presented in Figure 6–2(a) as dashed lines. The resulting values for conductivity are presented in Table 6–1.

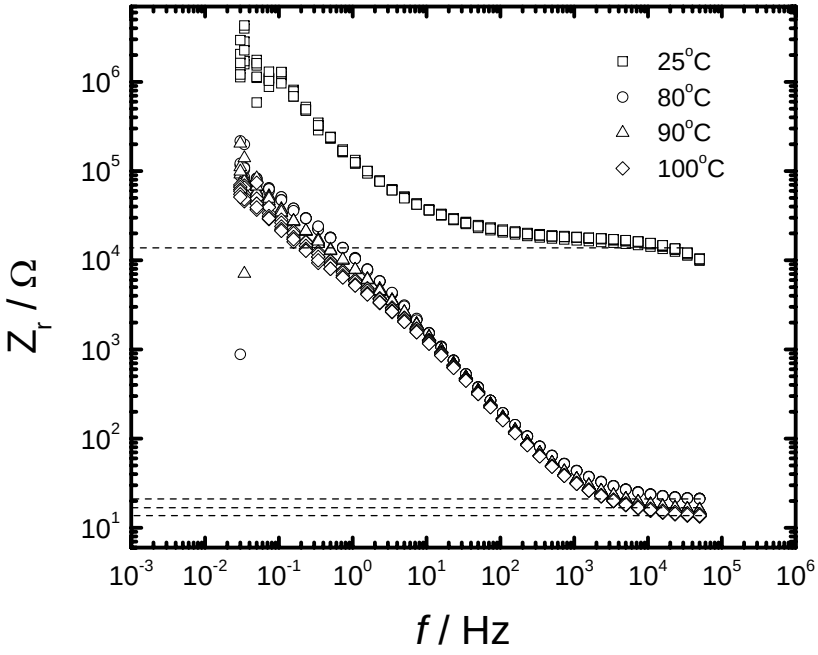

(a)

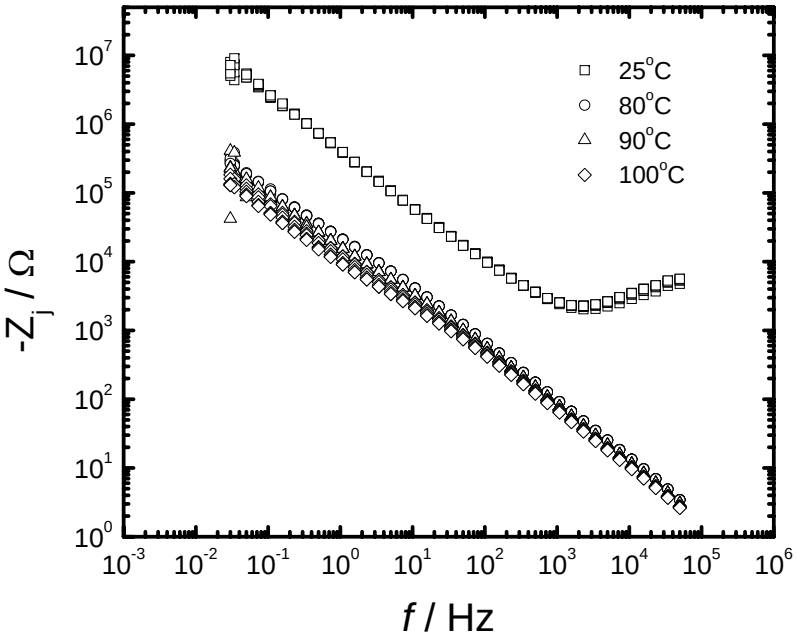

(b)

Figure 6–2: Plots of the imaginary and real part of the impedance as functions of frequency for Cell NA-BB with temperature as a parameter. Six replicates of each measurement are presented for each temperature.

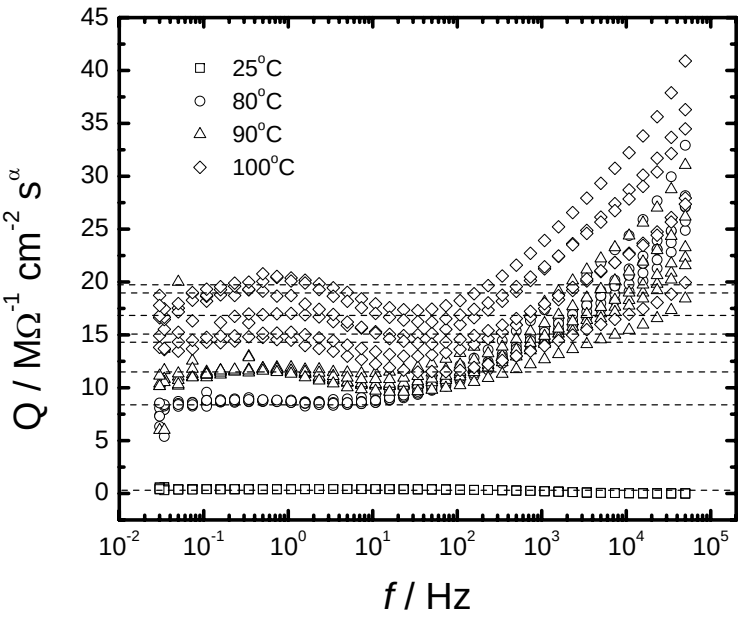

Figure 6–3: Effective CPE coefficient defined by equation (6.3) for Cell NA-BB. Six replicates of each measurement are presented for each temperature.

At low frequencies, the slope of the imaginary part of the impedance has a value of $-\alpha$. The values of α obtained from Figure 6–2(b) are also presented in Table 6–1.

For a blocking electrode, the value of Q can be obtained from the low-frequency asymptote where the current distribution associated with the electrode geometry does not influence the impedance response. The value of Q was calculated using

$$Q = -\frac{sin(\alpha\pi/2)}{Z_j(2\pi f)^\alpha} \tag{6.3}$$

and the resulting values are presented in Figure 6–3. The extracted values for Q are marked by dashed lines in Figure 6–3 and are reported in Table 6–1. As the temperature increases, the values for Q also increase. At 100°C the values for Q increased with time.

Table 6–1: Parameter values extracted from Figures 6–2 and 6–3 for Cell NA-BB.

Temp. / °C	α	$Q/\mathrm{M\Omega^{-1}cm^{-2}s^{\alpha}}$	$\kappa/\mathrm{mho\ cm^{-1}}$
25	0.824 ± 0.003	0.40 ± 0.0166	$2.97 \times 10^{-05} \pm 9.089 \times 10^{-07}$
80	0.704 ± 0.008	8.45 ± 0.132	$0.018 \pm 8.534 \times 10^{-05}$
90	0.728 ± 0.014	11.4 ± 0.617	$0.025 \pm 1.011 \times 10^{-04}$
100	0.749	14.3	0.027
	0.721	14.8	0.028
	0.701	16.8	0.028
	0.726	18.9	0.026
	0.693	19.3	0.026
	0.708	19.3	0.027

6.3 Comparison to Disk Electrode

The dimensionless imaginary part of the impedance $Z_j \kappa r_0$ is presented in Figure 6–4 as a function of dimensionless frequency

$$K = \frac{Q\omega^{\alpha} r_0}{\kappa} \tag{6.4}$$

The results presented in Figure 6–4 can be compared to the results obtained by Huang *et al.*[67] shown in Figure 6–5 for different values of α. A superposition of the data is evident in both Figures 6–4 and 6–5 at low frequency. This superposition is typical of blocking electrodes. The slope at low frequency has a value of -1 because the influence of the CPE parameter α is incorporated in the definition of the dimensionless frequency in equation (6.4).

A change in the slope from a value of -1 appears in Figure 6–4 at frequencies higher than $K = 6 \times 10^{-3}$. A similar change in slope appears in Figure 6–5 at frequencies $K > 1$. For the disk electrode, the change in slope at frequencies $K > 1$ is due to the non-uniform current distribution associated with the disk geometry. The geometry of the coin cells used for the present work is significantly different than that of a disk electrode with a counterelectrode infinitely far away. There is a potential for a non-uniform current distribution in the button cell, but the

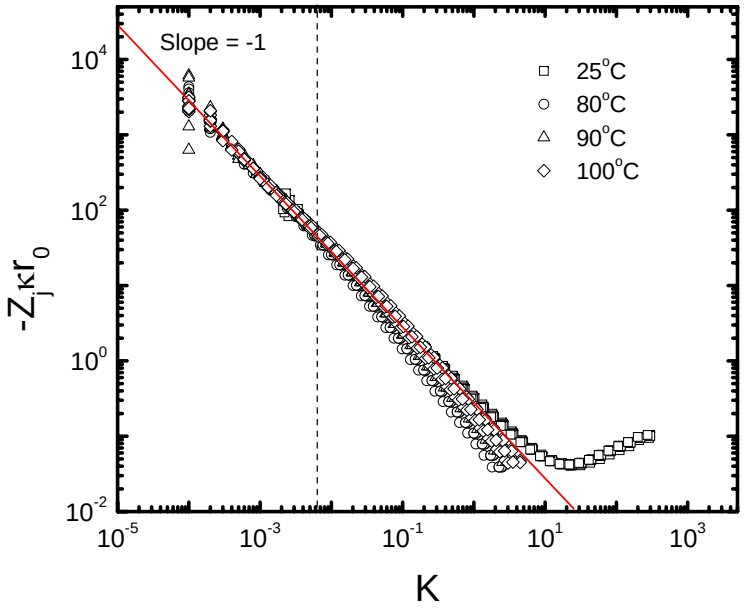

Figure 6–4: Dimensionless analysis for the impedance response of a stainless steel disk in PEO/LiTFSI electrolytes with temperature as a parameter.

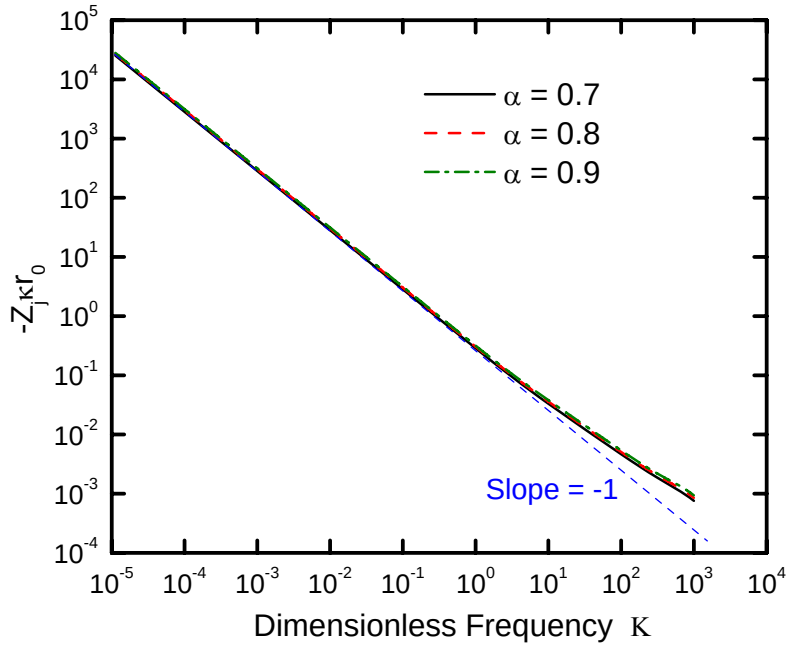

Figure 6–5: Dimensionless imaginary part of the impedance as a function of dimensionless frequency for a disk electrode with local capacitance dispersion. Theoretical result derived by Huang *et al.* .

geometry of the electrode-insulator interface is not well defined. The change of slope at $K = 6 \times 10^{-3}$ may be associated with a non-uniform current distribution.

6.4 Conclusions

The impedance response of the symmetric button cell with steel electrodes was that of a blocking electrode with local CPE behavior associated with a capacity dispersion. The high-frequency capacitive loop seen in the results of the symmetric lithium cell were not evident in the results from the cell with steel electrodes. Thus, the high-frequency capacitive loop seen in the impedance spectra of Chapter 5 are not associated with the dielectric response of the electrolyte. These loops must be described instead by a model that takes into account the reactions at the lithium electrode.

When conductivity κ and the CPE parameters Q and α are taken into account, the imaginary impedance responses for all the data collected with the symmetric stainless steel cell are superposed at low frequencies. This result was seen even when the low-temperature 25°C data were included, for which the electrolyte was solid and the conductivity was three orders of magnitude lower than for the melted electrolyte. This superposition provides evidence that the system behavior is indeed that of a blocking electrode and that no Faradaic reaction needed to be considered. At high frequencies, when the contribution of the non-uniform current distribution is more important, the experimental results deviated from the theoretical behavior. However, this deviation was anticipated since the geometry of the experimental system differs from the geometry of the system used to develop the theoretical results.

CHAPTER 7
MODEL DEVELOPMENT

The results presented in Chapter 6 demonstrated that the high-frequency capacity loop observed in the experimental results were due to reactions at the lithium electrodes. The electric circuit model proposed by Bouchet *et al.* does not describe the system correctly because he attributed the capacity loop to a dielectric behavior of the electrolyte. Still he was able to fit adequately his experimental data. This is the limitation of the electric circuits, more than one circuit network can be constructed which would provide equivalent statistically valid fits; and each of these models can arise from extremely different interpretations. Physico-chemical models are more efficient for interpretation of the physical properties and the kinetic processes of the system. However, the physico-chemical models have the disadvantage that they cannot be easily regressed to the experimental data. In the present work we developed a model that take into account the physics and chemistry of the system and can be use for regression analysis.

To develop such model it was necessary to have complimentary supporting information concerning the physics and chemistry of the system. Microscope images, scanning electron microscope (SEM) micrographs and information published in the literature were used to guide the model development.

7.1 Chemistry

It is well accepted in the literature that the reaction mechanism for the lithium electrodes is extremely complex and must be represented by a large number of reactions.[10,68,69] The electrolyte composition and the presence of additives and contaminants affect the mechanisms of transport. According to Aurbach and

Table 7–1: Reaction mechanisms of common lithium battery contaminants. Water was the only contaminant considered in this work.

Contaminant	Reaction Mechanisms
CO_2	$CO_2 + e^- + Li^+ \rightarrow CO_2Li$ $CO_2Li + CO_2 \rightarrow O{=}C\text{-}OCO_2Li$ $O{=}C\text{-}OCO_2Li + e^- + Li \rightarrow CO\uparrow + Li_2CO_3\downarrow$ $2LiOH\downarrow + CO_2 \rightarrow Li_2CO_3\downarrow$ $Li_2O\downarrow + CO_2 \rightarrow Li_2CO_3\downarrow$
H_2O	$H_2O + e^- + Li^+ \rightarrow LiOH + 1/2H_2$ $LiOH + Li^+ + e^- \rightarrow Li_2O + 1/2H_2$ $H + e^- + Li^+ \rightarrow LiH$
N_2	$N_2 + 6e^- + 6Li^+ \rightarrow 2Li_3N$
O_2	$O_2 + e^- + Li^+ \rightarrow LiO_2$ $LiO_2 + e^- + Li^+ \rightarrow Li_2O_2$ $Li_2O_2 + 2e^- + 2Li^+ \rightarrow 2Li_2O$
HF	$HF + e^- + Li^+ \rightarrow LiF + 1/2H_2$

Table reproduced from: G.Nazri and G. Pistoia, "Lithium Batteries: Science and Technology", (Norwell,MA: Kluwer Academic Publishers, 2004).

Schechter[10] the possible reactions between Li^+ and the LiTFSI salt are

$$LiN(SO_2CF_3)_2 + ne^- + nLi^+ \rightarrow Li_3N + Li_2S_2O_4 + LiF + C_2F_xLi_y \tag{7.1}$$

and

$$LiN(SO_2CF_3)_2 + 2e^- + 2Li^+ \rightarrow Li_2NSO_2CF_3 + CF_3SO_2Li \tag{7.2}$$

and the common contaminants present in this type of cell include CO_2, H_2O, N_2, O_2, and HF.[10,68,69] The reaction mechanisms of the common contaminants are summarized in Table 7–1.

As the exact composition, size and distribution of the particles that composed the SEI (see Section 2.2.4) are unknown, a simplified system was used. The reactions considered for the simplified system were the oxidation/reduction reaction of lithium,

$$Li \rightleftarrows Li^+ + e^- \tag{7.3}$$

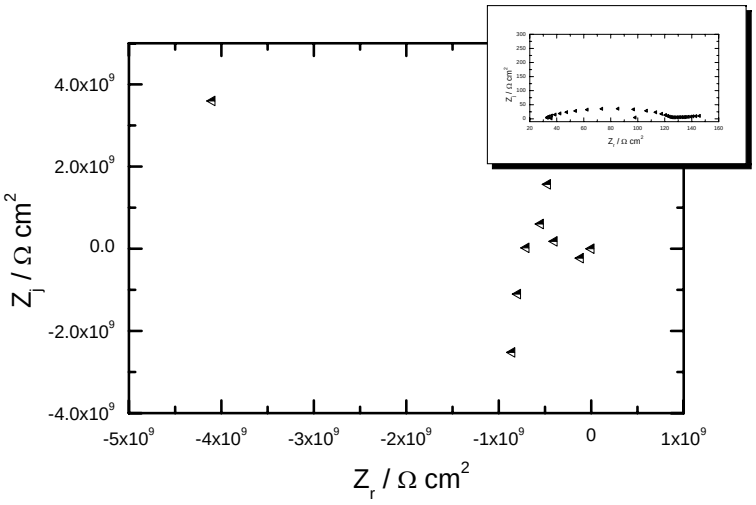

Figure 7–1: Impedance-plane or Nyquist representation of impedance data for Cell UF-DTr. Very large impedance at low frequencies can be observed suggesting that a disconnection of the system which may be attributed to gas evolution.

and the reactions due to the presence of water as a contaminant,

$$H_2O + e^- + Li^+ \rightarrow LiOH + 1/2H_2 \tag{7.4}$$

$$LiOH + Li^+ + e^- \rightarrow Li_2O + 1/2H_2 \tag{7.5}$$

It has been reported in the literature that these cells contain traces of water and the formation of LiOH is expected at the lithium interface, which support the selection of equations (7.4) and (7.5) as part of the proposed reaction mechanism.[70] Also, the impedance data and broken seals provided evidence of gas evolution. An impedance spectrum of cell UF-DTr taken approximately 14 hours after the experiment started is presented in Figure 7–1. The impedance response of the cell was as expected for a system with distributed time constants, as shown in the insert. However, a large impedance was observed at low frequencies. This is usually attributed to a disconnection of the system, which may be associated with gas evolution. This behavior was observed in more than one cell.

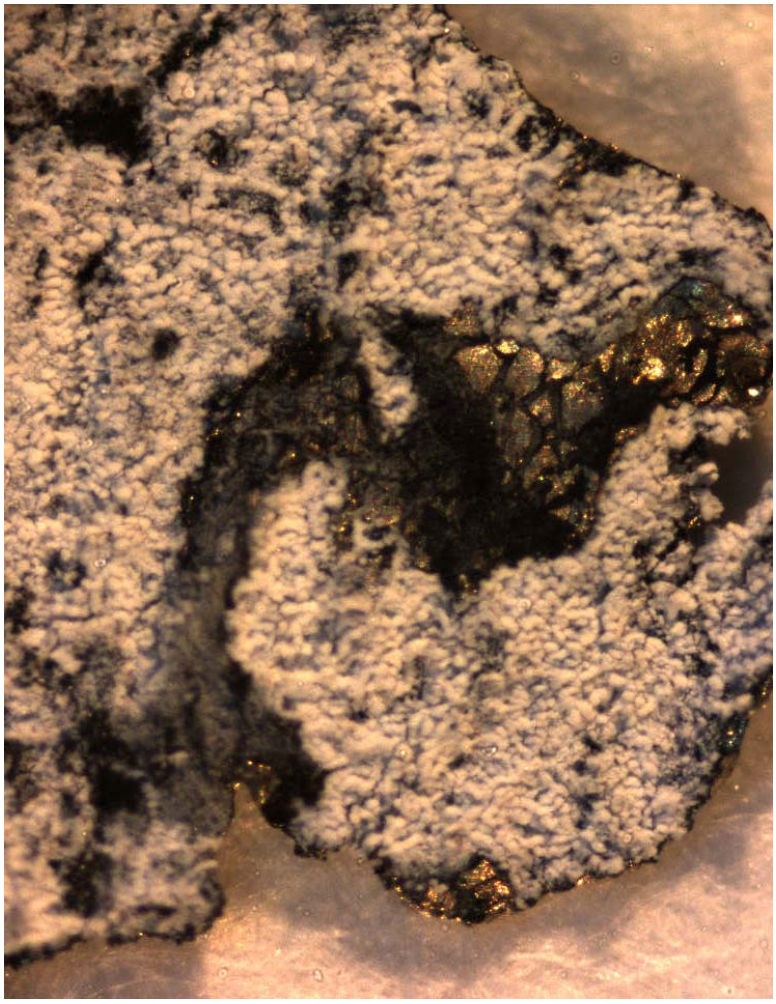

Figure 7–2: Cell UF-ATe lithium electrode surface. The surface of the electrode was almost completely covered with a white to blue oxide layer.

7.2 Physics

The formation of passivating films on the lithium surface has been reported extensively in the literature.[10,18–20] Peled was the first to introduce and name the SEI.[18,19] According to Peled, the SEI is a heterogenous film, consisting of a mosaic of numerous individual particles of different chemical composition being in partial contact with each other at the grain boundaries, as explained in Section 2.2.4.

Some of the cells used in this research were opened after the experiments. Microscopic images of cells UF-ATe and UF-BTe are presented in Figures 7–2 and 7–3. A white to blue oxide layer was observed on the lithium surface. Cell UF-ATe

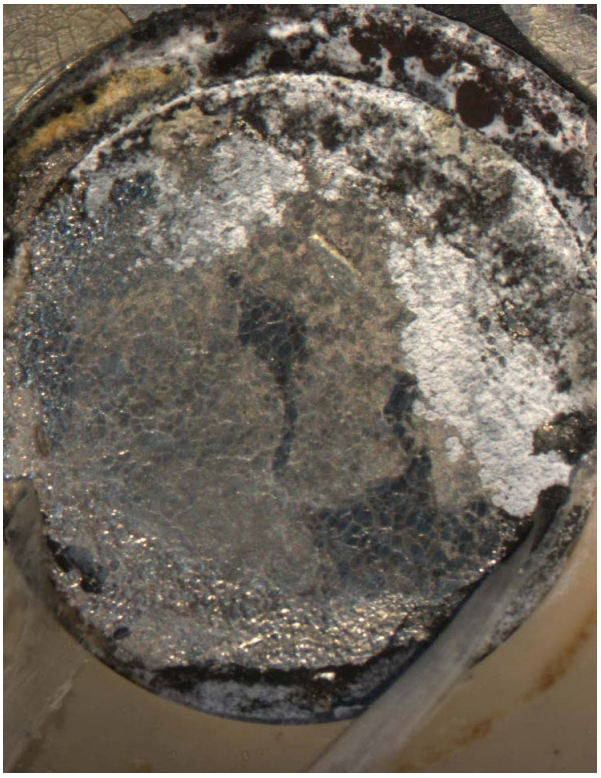

(a)

(b)

Figure 7–3: Cell UF-BTe lithium electrode surface. The edges of the electrode were covered with a white to blue oxide layer, while the inner surface kept a much brighter metallic lustre.

was almost completely covered with the layer, while in cell UF-BTe, the oxide layer was observed in the perimeter of the cells, as shown in Figure 7–2 and 7–3(a), respectively. For most of the cells, the oxide layer was more evident on the lithium edge than inside the battery. This behavior has been reported in the literature[70] and is evidence of a non-uniform current distribution.

SEM micrographs were taken to get an understanding of the structure of this layer. The layer is an heterogenous film that appears to be a mosaic of individual particles, as shown in Figures 7–4 and 7–5. Unfortunately, it was not possible to determine the composition of the layer.

Several options were considered as possible mechanisms of transport. All of the mechanisms considered take into account the presence of the passivating films at the electrodes surface, as described in the literature.[10,18–20] According to Naudin *et al.* ,[29] commercial lithium foils have a native layer that is composed of approximately 10–100 nm Li_2O inside layer and 1–20 nm of Li_2CO_3/LiOH outside layer, as shown in Figure 7–6.

The first mechanism is presented in Figure 7–7. In this model, the only reaction taking place at the electrode surface is the oxidation/reduction reaction of Li. The LiOH and Li_2O formation reactions take place on the surface of the passivating layer.

On the second mechanism it was assumed that the lithium oxidation/reduction reaction take place at the lithium metal surface only, but the LiOH and Li_2O formation reactions can take place in both the lithium metal surface and the oxide layer surface. A schematic diagram of the system is shown in Figure 7–8.

7.3 Model Development

The procedure explained in Section 3.5 was used to develop the impedance response model. In this section the model for the mechanisms shown in Figure 7–8

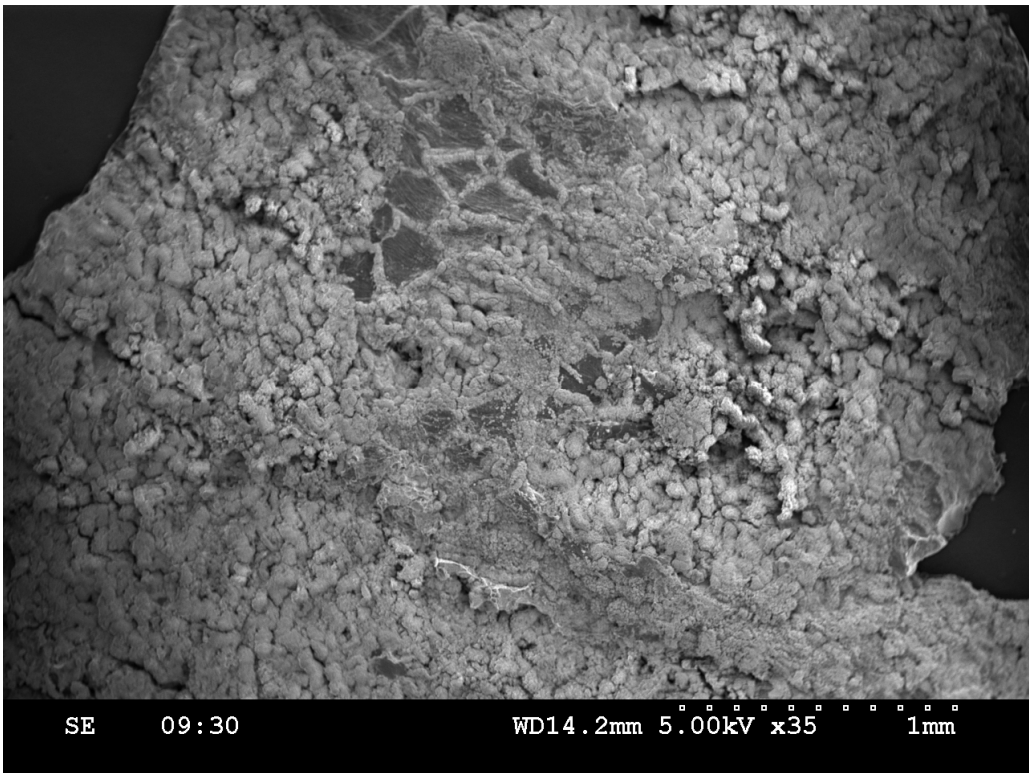

(a)

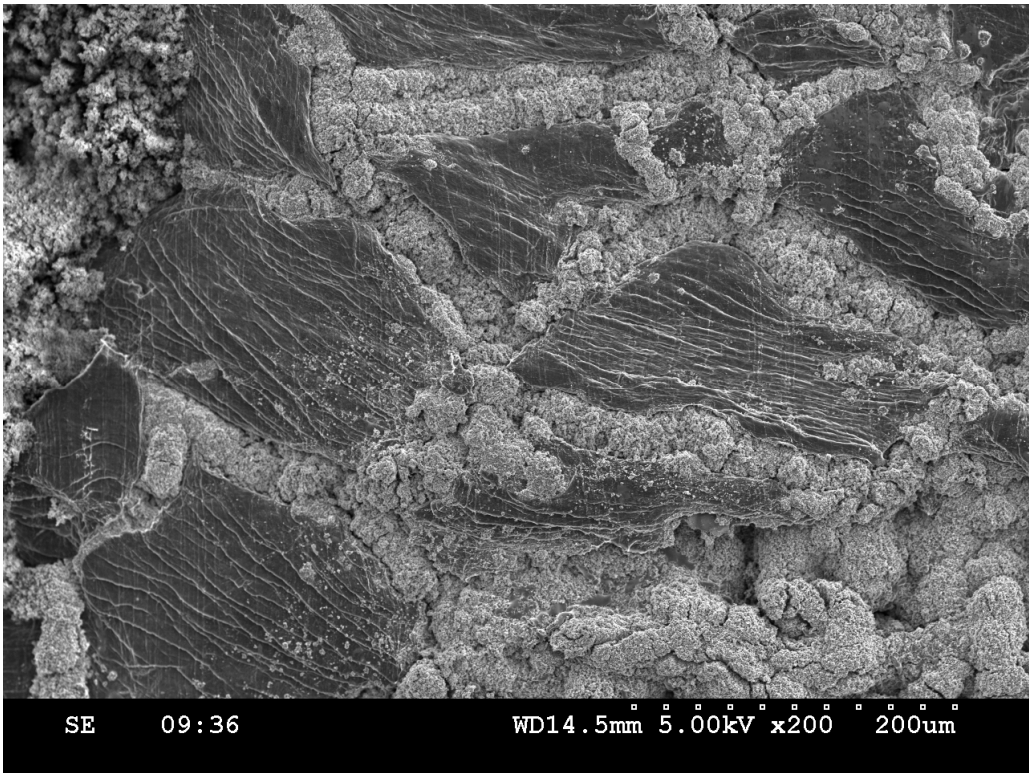

(b)

Figure 7–4: Scanning electron micrographs of Cell UF-ATe lithium electrode surface. (a) Magnification = 35. (b) Magnification = 200.

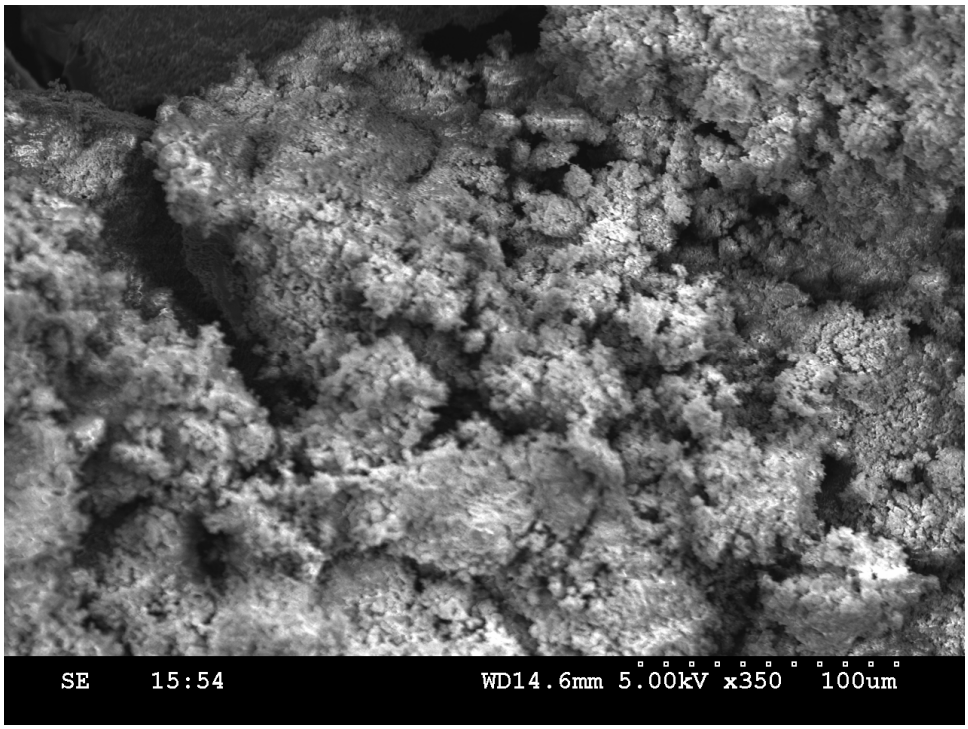

Figure 7–5: Scanning electron micrographs of Cell UF-BTe lithium electrode surface. Magnification = 350.

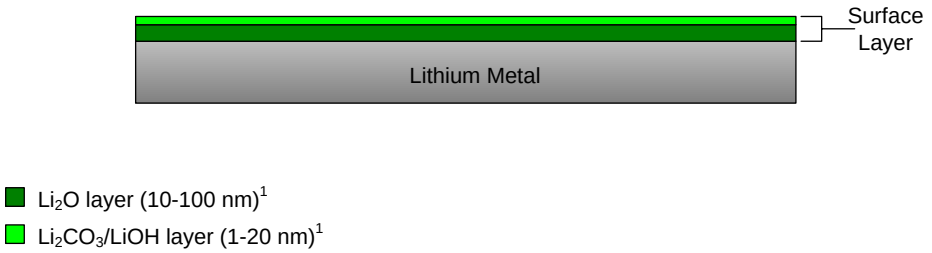

Figure 7–6: Commercial lithium foil native layer composition, as described by Naudin *et al.*[29]

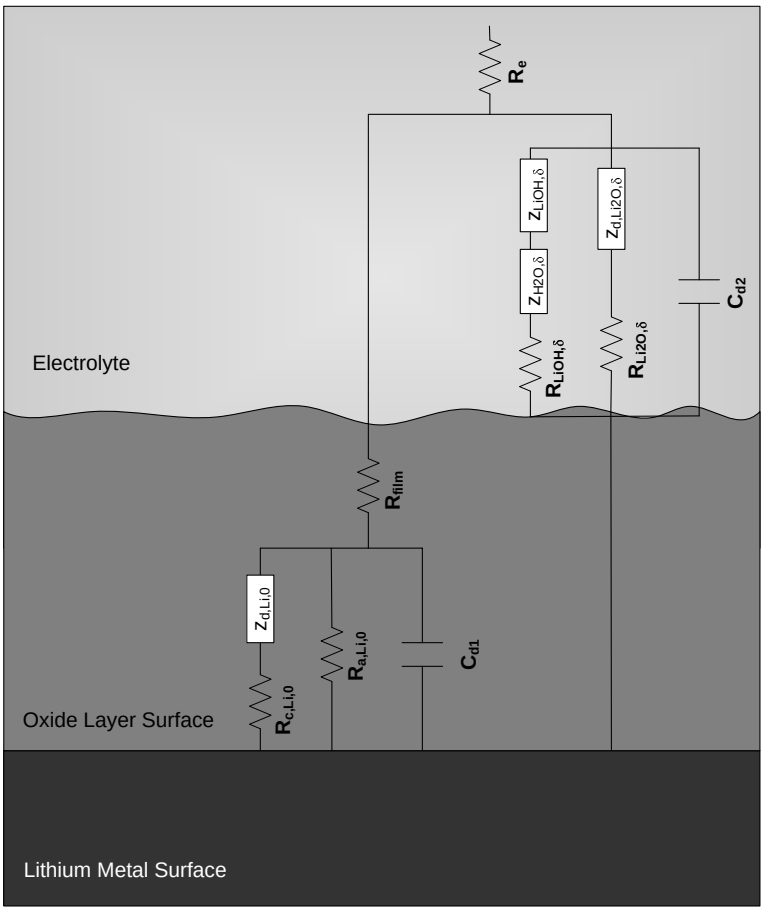

Figure 7–7: Schematic of the simplified system. Two surfaces were identified in which the reactions take place. The lithium oxidation/reduction reaction take place at the lithium metal surface and the LiOH and Li_2O formation reactions take place in the oxide layer surface.

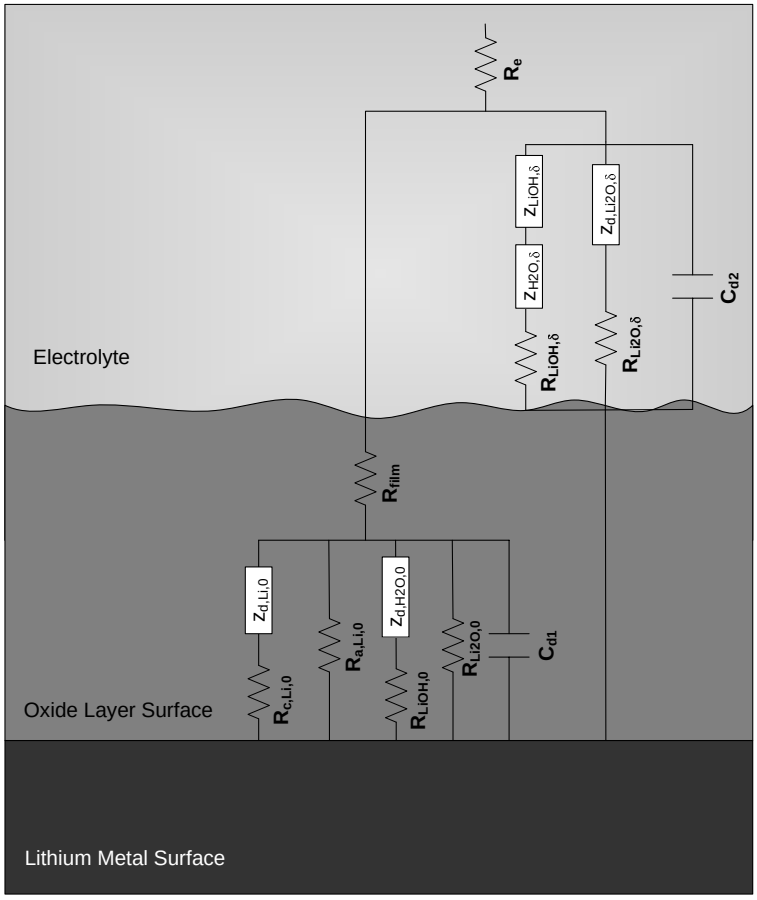

Figure 7–8: Schematic of the simplified system. Two surfaces were identified in which the reactions take place. The lithium oxidation/reduction reaction take place at the lithium metal surface only, but the LiOH and Li_2O formation reactions can take place in both the lithium metal surface and the oxide layer surface.

is explained in detail. Only the final expression for the mechanism shown in Figure 7–7 is presented.

7.3.1 Steady State

The equation for the faradaic current density, $i_{i,f}$, can be expressed in terms of a steady time-independent value and an oscillating value for each of the three reactions considered in the system. The steady state values are

$$\bar{i}_{a,\mathrm{Li},0} = Fk_{a,\mathrm{Li},0}\exp(b_{a,\mathrm{Li},0}(V - V_{\mathrm{Li}})) \tag{7.6}$$

and

$$\bar{i}_{c,\mathrm{Li},0} = -Fk_{c,\mathrm{Li},0}\bar{c}_{\mathrm{Li}^+,\mathrm{Li},0}\exp(-b_{c,\mathrm{Li},0}(V - V_{\mathrm{Li},0})) \tag{7.7}$$

for the lithium oxidation/reduction reaction taking place at the electrode surface. When LiOH and the Li_2O are formed in the lithium metal the steady state current contributions are

$$\bar{i}_{\mathrm{LiOH},0} = -Fk_{c,\mathrm{LiOH},0}\bar{c}_{\mathrm{H_2O},0}\exp(-b_{c,\mathrm{LiOH},0}(V - V_{\mathrm{LiOH},0})) \tag{7.8}$$

and

$$\bar{i}_{\mathrm{Li_2O},0} = -Fk_{c,\mathrm{Li_2O},0}\exp(-b_{c,\mathrm{Li_2O},0}(V - V_{\mathrm{Li_2O},0})) \tag{7.9}$$

The steady state currents at the oxide layer surface are

$$\bar{i}_{\mathrm{LiOH},\delta} = -Fk_{c,\mathrm{LiOH},\delta}\bar{c}_{\mathrm{Li}^+,\mathrm{LiOH},\delta}\bar{c}_{\mathrm{H_2O},\delta}\exp(-b_{c,\mathrm{LiOH},\delta}(V - V_{\mathrm{LiOH},\delta})) \tag{7.10}$$

and

$$\bar{i}_{\mathrm{Li_2O},\delta} = -Fk_{c,\mathrm{Li_2O},\delta}\bar{c}_{\mathrm{Li}^+,\mathrm{Li_2O},\delta}\exp(-b_{c,\mathrm{Li_2O},\delta}(V - V_{\mathrm{Li_2O},\delta})) \tag{7.11}$$

for the LiOH and Li_2O formation reactions, respectively. The subscript 0 and δ represent the lithium metal surface and the oxide layer surface, respectively. Notice that the diffusion of lithium for the reactions that involve water is considered when

the reactions take place in the oxide layer but is not considered when the reactions take place in the lithium metal surface.

7.3.2 Sinusoidal Steady State

The oscillating component of the current was derived using,

$$\widetilde{i}_{i,f} = \left(\frac{\partial f}{\partial V}\right)_{c_i,\theta_k} \widetilde{V} + \sum \left(\frac{\partial f}{\partial c_{i,0}}\right)_{V,c_{j\neq i},\theta_k} \widetilde{c}_{i,0} + \sum \left(\frac{\partial f}{\partial \theta_k}\right)_{V,c_i,\theta_{l\neq k}} \widetilde{\theta}_k \tag{7.12}$$

where $\tilde{V}$ is potential, $\tilde{c}_{i,0}$ is concentration and $\tilde{\theta}_k$ is surface coverage. In this model the surface coverage was assumed to be constant, so the current is only dependent on potential and concentration of lithium and water. Solving equation (7.12) with respect to each of the steady–state current contributions would give the oscillating current contributions of the reactions considered in the system. These expressions are

$$\widetilde{i}_{a,\mathrm{Li},0} = R^{-1}_{a,\mathrm{Li},0}\widetilde{V} \tag{7.13}$$

where,

$$R^{-1}_{a,\mathrm{Li},0} = Fb_{a,\mathrm{Li},0}k_{a,\mathrm{Li},0}\exp(b_{a,\mathrm{Li},0}(V - V_{\mathrm{Li},0})) \tag{7.14}$$

and

$$\widetilde{i}_{c,\mathrm{Li},0} = R^{-1}_{c,\mathrm{Li},0}\widetilde{V} + (-Fk_{c,\mathrm{Li},0}\exp(-b_{c,\mathrm{Li},0}(V - V_{\mathrm{Li},0}))\widetilde{c}_{\mathrm{Li^+},\mathrm{Li},0} \tag{7.15}$$

where,

$$R^{-1}_{c,\mathrm{Li},0} = Fb_{c,\mathrm{Li},0}k_{c,\mathrm{Li},0}\bar{c}_{\mathrm{Li^+},\mathrm{Li},0}\exp(-b_{c,\mathrm{Li},0}(V - V_{\mathrm{Li},0})) \tag{7.16}$$

for the lithium oxidation/reduction reaction taking place at the electrode surface. The oscillating current contributions of the LiOH and Li_2O formation reactions in the lithium metal are

$$\widetilde{i}_{\mathrm{LiOH},0} = R^{-1}_{\mathrm{LiOH},0}\widetilde{V} + (-Fk_{c,\mathrm{LiOH},0}\exp(-b_{c,\mathrm{LiOH},0}(V - V_{\mathrm{LiOH},0})))\widetilde{c}_{\mathrm{H_2O},0} \tag{7.17}$$

where,

$$R^{-1}_{\mathrm{LiOH},0} = Fb_{c,\mathrm{LiOH},0}k_{c,\mathrm{LiOH},0}\bar{c}_{\mathrm{H_2O},0}\exp(-b_{c,\mathrm{LiOH},0}(V - V_{\mathrm{LiOH},0})) \tag{7.18}$$

and

$$\widetilde{i}_{\mathrm{Li_2O},0} = R^{-1}_{\mathrm{Li_2O},0}\widetilde{V} \tag{7.19}$$

where,

$$R^{-1}_{\mathrm{Li_2O},0} = Fb_{c,\mathrm{Li_2O},0}k_{c,\mathrm{Li_2O},0}\exp(-b_{c,\mathrm{Li_2O},0}(V - V_{\mathrm{Li_2O},0})). \tag{7.20}$$

When the reactions occur in the oxide layer, the oscillating current contributions are

$$\begin{aligned}\widetilde{i}_{\mathrm{LiOH},\delta} = R^{-1}_{\mathrm{LiOH},\delta}\widetilde{V} &+ (-Fk_{c,\mathrm{LiOH},\delta}\overline{c}_{\mathrm{H_2O},\delta}\exp(-b_{c,\mathrm{LiOH},\delta}(V - V_{\mathrm{LiOH},\delta})))\widetilde{c}_{\mathrm{Li^+},\mathrm{LiOH},\delta} \\ &+ (-Fk_{c,\mathrm{LiOH},\delta}\overline{c}_{\mathrm{Li^+},\mathrm{LiOH},\delta}\exp(-b_{c,\mathrm{LiOH},\delta}(V - V_{\mathrm{LiOH},\delta})))\widetilde{c}_{\mathrm{H_2O},\delta}\end{aligned} \tag{7.21}$$

where,

$$R^{-1}_{\mathrm{LiOH},\delta} = Fb_{c,\mathrm{LiOH},\delta}k_{c,\mathrm{LiOH},\delta}\overline{c}_{\mathrm{Li^+},\mathrm{LiOH},\delta}\overline{c}_{\mathrm{H_2O},\delta}\exp(-b_{c,\mathrm{LiOH},\delta}(V - V_{\mathrm{LiOH},\delta})) \tag{7.22}$$

and

$$\widetilde{i}_{\mathrm{Li_2O},\delta} = R^{-1}_{\mathrm{Li_2O},\delta}\widetilde{V} + (-Fk_{c,\mathrm{Li_2O},\delta}\exp(-b_{c,\mathrm{Li_2O},\delta}(V - V_{\mathrm{Li_2O},\delta})))\widetilde{c}_{\mathrm{Li^+},\mathrm{Li_2O},\delta} \tag{7.23}$$

where,

$$R^{-1}_{\mathrm{Li_2O},\delta} = Fb_{c,\mathrm{Li_2O},\delta}k_{c,\mathrm{Li_2O},\delta}\overline{c}_{\mathrm{Li^+},\mathrm{Li_2O},\delta}\exp(-b_{c,\mathrm{Li_2O},\delta}(V - V_{\mathrm{Li_2O},\delta})) \tag{7.24}$$

7.3.3 Mass Transfer

A second equation was needed to correlate concentration of lithium and water to the corresponding current contributions

$$\overline{i_i} = -n_iFD_i\left.\frac{d\overline{c_i}}{dy}\right|_{y=0} \tag{7.25}$$

This equation can be expressed in terms of the oscillating contributions as

$$\widetilde{i_i} = -n_iFD_i\left.\frac{d\widetilde{c_i}}{dy}\right|_{y=0} \tag{7.26}$$

It is convenient to write equation (7.26) in terms of the dimensionless solution to the appropriate diffusion or convective equation

$$\widetilde{i_i} = -n_i F D_i \frac{\widetilde{C}_{i,0}}{\delta_i} \widetilde{\theta}_i'(0) \tag{7.27}$$

where $\theta_i = \widetilde{c_i}/\widetilde{c}_{i,0}$. θ_i was evaluated assuming diffusion through an infinite layer as

$$\frac{1}{\widetilde{\theta}_i'(0)} = -\frac{1}{\sqrt{j\frac{\omega}{D_i}}} \tag{7.28}$$

The definition of θ_i was then substituted into equation (7.27) to obtain the relationship between concentration and current,

$$\widetilde{i_i} = n_i F D_i \frac{\widetilde{c}_{i,0}}{\delta_i} \sqrt{j\frac{\omega}{D_i}} \tag{7.29}$$

The final current expression as a function of potential for the reactions that take place in the lithium metal surface are

$$\widetilde{i}_{a,\mathrm{Li},0} = {R_{a,\mathrm{Li},0}}^{-1} \widetilde{V} \tag{7.30}$$

and

$$\widetilde{i}_{c,\mathrm{Li},0} = (R_{c,\mathrm{Li},0} + z_{d,\mathrm{Li},0})^{-1} \widetilde{V} \tag{7.31}$$

where,

$$z_{d,\mathrm{Li},0} = \frac{R_{a,\mathrm{Li},0} k_{c,\mathrm{LiOH},0} \exp(-b_{c,\mathrm{LiOH},0}(V - V_{\mathrm{Li},0}))\delta_{\mathrm{Li},0}}{D_{\mathrm{Li}^+}\sqrt{j\frac{\omega}{D_{\mathrm{Li}^+}}}} \tag{7.32}$$

for the lithium oxidation/reduction reaction and

$$\widetilde{i}_{\mathrm{LiOH},0} = (R_{\mathrm{LiOH},0} + z_{d,\mathrm{H_2O},0})^{-1} \widetilde{V} \tag{7.33}$$

where,

$$z_{d,\mathrm{H_2O},0} = \frac{R_{\mathrm{LiOH},0} k_{c,\mathrm{LiOH},0} \exp(-b_{c,\mathrm{LiOH},0}(V - V_{\mathrm{LiOH},0}))\delta_{\mathrm{H_2O}}}{D_{\mathrm{H_2O}}\sqrt{j\frac{\omega}{D_{\mathrm{H_2O}}}}} \tag{7.34}$$

and

$$\widetilde{i}_{\mathrm{Li_2O},0} = {R_{\mathrm{Li_2O},0}}^{-1}\widetilde{V} \tag{7.35}$$

for the LiOH and Li_2O formation reactions. For the reactions that take place in the oxide layer surface the final current was expressed as

$$\widetilde{i}_{\mathrm{LiOH},\delta} = (R_{\mathrm{LiOH},\delta} + z_{d,\mathrm{H_2O},\delta} + z_{\mathrm{Li},\delta_2})^{-1}\widetilde{V} \tag{7.36}$$

where

$$z_{\mathrm{H_2O},\delta} = \frac{R_{\mathrm{LiOH},\delta}k_{c,\mathrm{LiOH},\delta}\overline{c}_{\mathrm{Li^+},\mathrm{LiOH},\delta}\exp(-b_{c,\mathrm{LiOH},\delta}(V - V_{\mathrm{LiOH},\delta}))\delta_{\mathrm{H_2O},\delta}}{D_{\mathrm{H_2O}}\sqrt{j\frac{\omega}{D_{\mathrm{H_2O}}}}} \tag{7.37}$$

and

$$z_{\mathrm{Li},\delta_2} = \frac{R_{\mathrm{LiOH},\delta}k_{c,\mathrm{LiOH},\delta}\overline{c}_{\mathrm{H_2O},\mathrm{LiOH},\delta}\exp(-b_{c,\mathrm{LiOH},\delta}(V - V_{\mathrm{LiOH},\delta}))\delta_{\mathrm{Li^+},\delta_2}}{D_{\mathrm{Li^+}}\sqrt{j\frac{\omega}{D_{\mathrm{Li^+}}}}} \tag{7.38}$$

for the LiOH formation reactions and for the Li_2O formation reactions the final current was expressed as

$$\widetilde{i}_{\mathrm{Li_2O},\delta} = (R_{\mathrm{Li_2O},\delta} + z_{d,\mathrm{Li},\delta_3})^{-1}\widetilde{V} \tag{7.39}$$

where

$$z_{d,\mathrm{Li},\delta_3} = \frac{R_{\mathrm{Li_2O},\delta}k_{c,\mathrm{Li_2O},\delta}\exp(-b_{c,\mathrm{Li_2O},\delta}(V - V_{\mathrm{Li_2O},\delta}))\delta_{\mathrm{Li^+},\delta_3}}{D_{\mathrm{Li^+}}\sqrt{j\frac{\omega}{D_{\mathrm{Li^+}}}}} \tag{7.40}$$

The total current density was expressed in terms of the faradaic and charging currents as

$$\widetilde{i_i} = \widetilde{i}_{i,f} + j\omega C_d\widetilde{V} \tag{7.41}$$

where the faradaic current $\widetilde{i_f}$ for the reaction taking place in the lithium surface is given by

$$\widetilde{i}_{0,f} = \widetilde{i}_{\mathrm{a,Li},0} + \widetilde{i}_{\mathrm{c,Li},0} + \widetilde{i}_{\mathrm{LiOH},0} + \widetilde{i}_{\mathrm{Li_2O},0}, \tag{7.42}$$

$\widetilde{i_f}$ for the reaction taking place in the oxide layer surface is given by

$$\widetilde{i}_{\delta,f} = \widetilde{i}_{\mathrm{LiOH},\delta} + \widetilde{i}_{\mathrm{Li_2O},\delta}, \tag{7.43}$$

and C_d is the double layer capacitance.

7.3.4 Impedance Expressions

The difference between the potential measured at the surface and the potential measured some distance away is given by

$$\widetilde{U} = \widetilde{i}R_e + \widetilde{V} \tag{7.44}$$

Using equation (7.44) the impedance for the lithium surface and the oxide layer were calculated as

$$Z = \frac{\widetilde{U}}{\widetilde{i}} \tag{7.45}$$

where the impedance of the lithium surface was calculated to be

$$Z_0 = R_{eq} + \frac{1}{(R_0)^{-1} + (R_{\mathrm{c,Li},0} + z_{\mathrm{d,Li},0})^{-1} + (R_{\mathrm{LiOH},0} + z_{\mathrm{d,H_2O},0})^{-1} + j\omega C_{d1}} \tag{7.46}$$

where

$$R_0^{-1} = {R_{\mathrm{a,Li},0}}^{-1} + R_{\mathrm{Li_2O},0} \tag{7.47}$$

and the impedance of the oxide layer surface was calculated to be

$$Z_\delta = R_e + \frac{1}{(R_{\mathrm{LiOH},\delta} + z_{\mathrm{d,H_2O},\delta} + z_{\mathrm{d,Li},\delta_2})^{-1} + (R_{\mathrm{Li_2O},\delta} + z_{\mathrm{d,Li},\delta_3})^{-1} + j\omega C_{d2}} \tag{7.48}$$

The electrolyte resistance term in the Z_0 was replaced by an equivalent resistance that correspond to

$$R_{eq} = (R_e + R_{film}) \tag{7.49}$$

where R_{film} is the resistance across the oxide layer. The impedance of the lithium surface for the system presented in Figure 7–7 was calculated to be

$$Z_0 = R_e + \frac{1}{(R_{\mathrm{a,Li},0})^{-1} + (R_{\mathrm{c,Li},0} + z_{\mathrm{d,Li},0})^{-1} + j\omega C_{d1}} \tag{7.50}$$

and the impedance of the oxide layer surface was calculated to be

$$Z_\delta = R_e + \frac{1}{(R_{\mathrm{LiOH},\delta} + z_{\mathrm{d,H_2O},\delta} + z_{\mathrm{d,Li},\delta_2})^{-1} + (R_{\mathrm{Li_2O},\delta} + z_{\mathrm{d,Li},\delta_3})^{-1} + j\omega C_{d2}} \tag{7.51}$$

The overall impedance for both systems was finally calculated to be

$$Z_T = \frac{1}{Z_0^{-1} + Z_\delta^{-1}} \tag{7.52}$$

7.4 Results

In this section results of cell UF-BTe exposed at 80°C are presented and the results are compared to the models. The object of this comparison was to show that the model developed can describe qualitatively the features seen in the experimental data. The modelled results were calculated using Matlab. The parameters used in each model are presented in Table 7–2.

The traditional Nyquist or impedance–plane representation is presented in Figure 7–9 for the experimental data and the models. All plots indicate that the system have characteristic time constants distributed over a wide–range of time scales. Also, in the plots a low frequency tail is observed. However, in Figure 7–9(a) a smooth transition and a lower slope are observed between the high frequency capacitive loop and the low frequency tail, whereas in Figures 7–9(b) and 7–9(c) a sharp transition and a steeper slope are observed.

The imaginary representation is shown in Figure 7–10 for the experimental data and the models. The general behavior of both plots is similar. However, the slope of the graph at high frequency in Figure 7–10(a) is -0.7653, while for Figures 7–10(b) and 7–10(c) is -1. This difference is explained due to a distribution of time constants in the experimental system. This distribution is also evident in the non-uniform coverage of the cells surface films.

The real representation is shown in Figure 7–11 for the experimental data and the models. The general behavior of both plots is similar.

Table 7–2: Summary of the parameters used to calculate the impedance response of the models presented in Section 7.

Parameter	Model 1	Model 2
D_{Li}	10^{-9}	10^{-9}
D_{H2O}	10^{-10}	10^{-10}
$k_{c,Li,0}$	100	100
$k_{a,Li,0}$	0.001	0.001
$k_{c,LiOH,0}$		100
$k_{c,Li2O,0}$		100
$k_{c,LiOH,\delta}$	100	100
$k_{c,Li2O,\delta}$	100	100
$b_{c,Li,0}$	19.7	19.7
$b_{a,Li,0}$	0.197	0.197
$b_{c,LiOH,0}$		19.7
$b_{c,Li2O,0}$		19.7
$b_{c,LiOH,\delta}$	19.7	19.7
$b_{c,Li2O,\delta}$	19.7	19.7
V	0.8	0.8
$V_{Li,0}$	0.1	0.1
$V_{LiOH,0}$		0.01
$V_{Li2O,0}$		0.01
$V_{LiOH,\delta}$	0.01	0.01
$V_{Li2O,\delta}$	0.01	0.01
$c_{Li+,Li,0}$	0.1	0.1
$c_{H2O,0}$		0.01
$c_{H2O,\delta}$	0.01	0.01
$c_{Li+,LiOH,\delta}$	0.03	0.03
$c_{Li+,Li2O,\delta}$	0.03	0.03
$R_{a,Li,0}$	300	300
$R_{c,Li,0}$	200	200
$R_{LiOH,0}$		150
$R_{Li2O,0}$		150
$R_{LiOH,\delta}$	150	300
$R_{Li2O,\delta}$	150	200
R_e	20	20
R_{eq}	140	180
$\delta_{Li,0}$		1
$\delta_{H2O,0}$		1
$\delta_{Li+,\delta 2}$	1	1
$\delta_{H2O,\delta}$	1	1
$\delta_{Li+,\delta 3}$	0.5	0.5
C_{d1}	0.000001	0.000001
C_{d2}	0.000001	0.000001

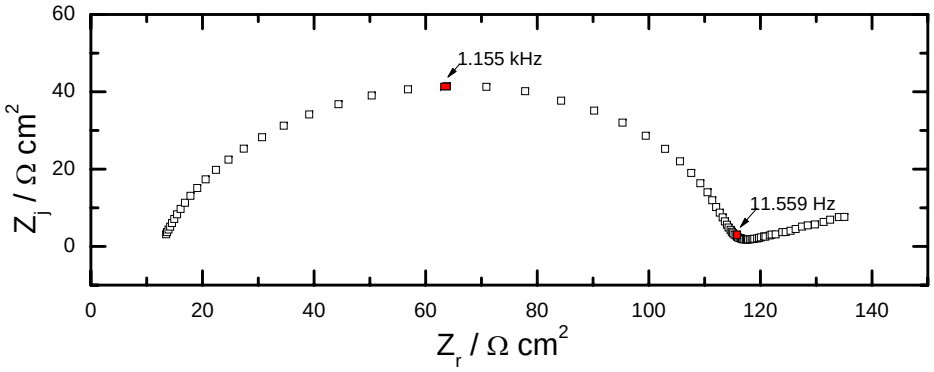

(a)

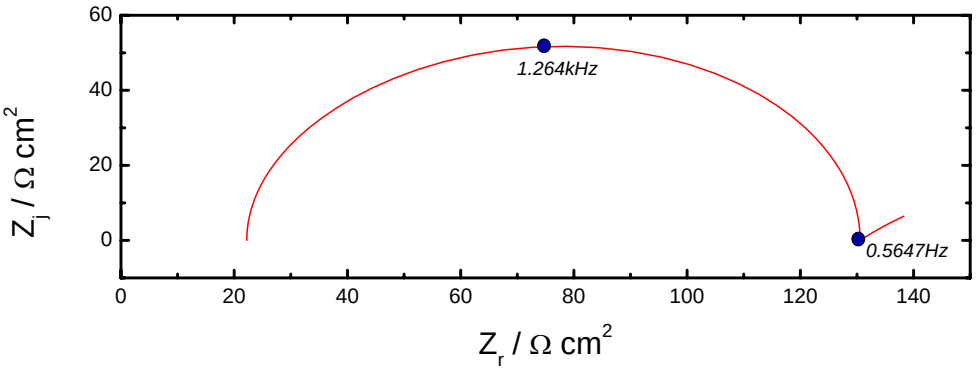

(b)

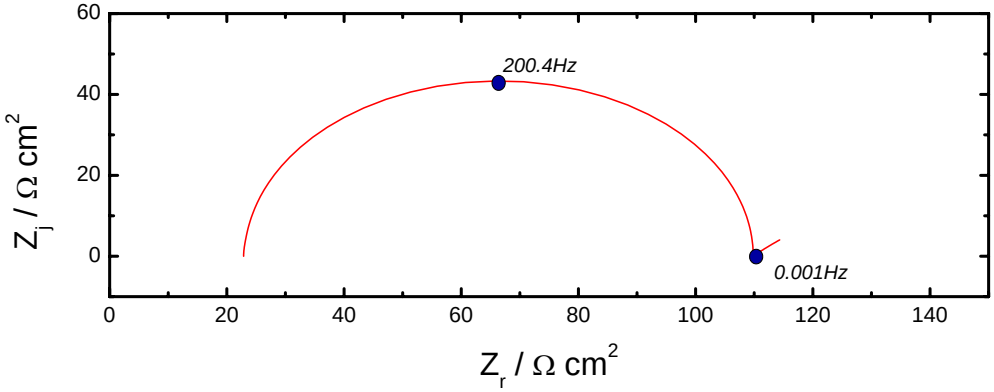

(c)

Figure 7–9: Impedance–plane or Nyquist representation of impedance data of a symmetric cell. (a) Experimental Result. (b) Model 1. (c) Model 2.

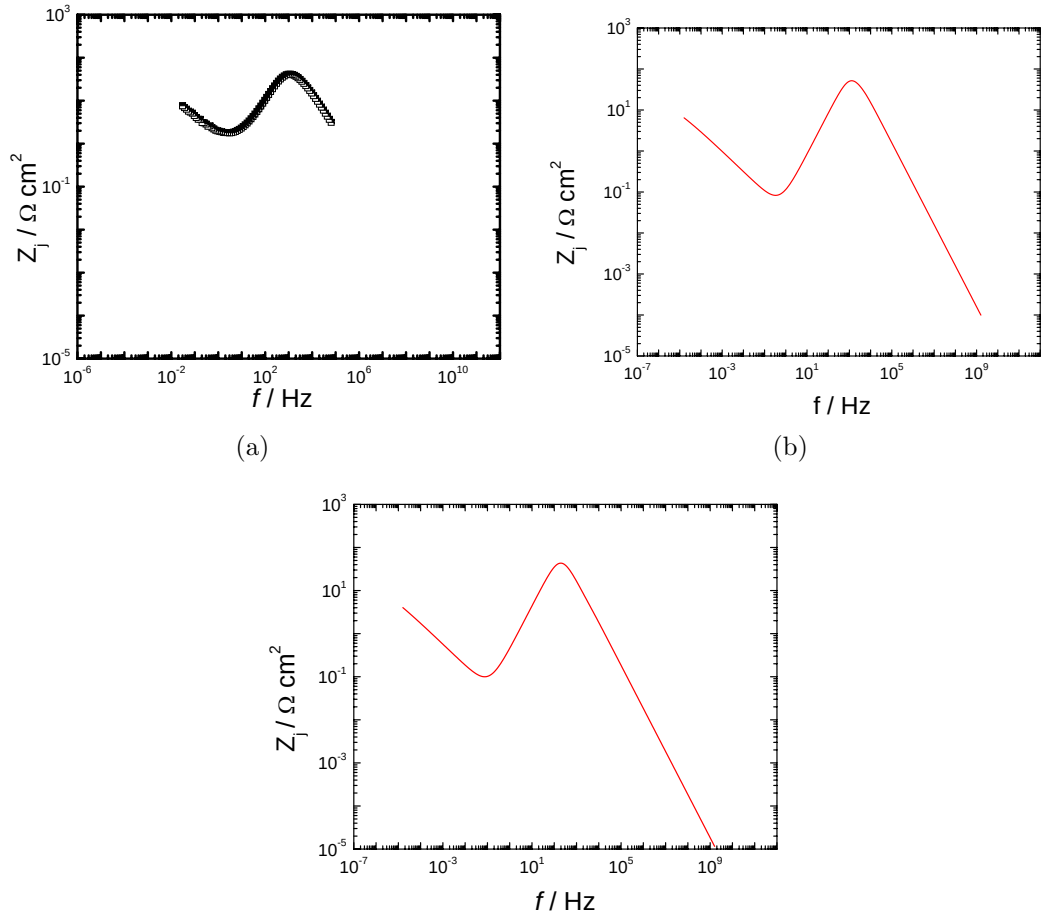

Figure 7–10: Imaginary plots of impedance data of a symmetric cell. (a) Experimental Result. (b) Model 1. (c) Model 2.

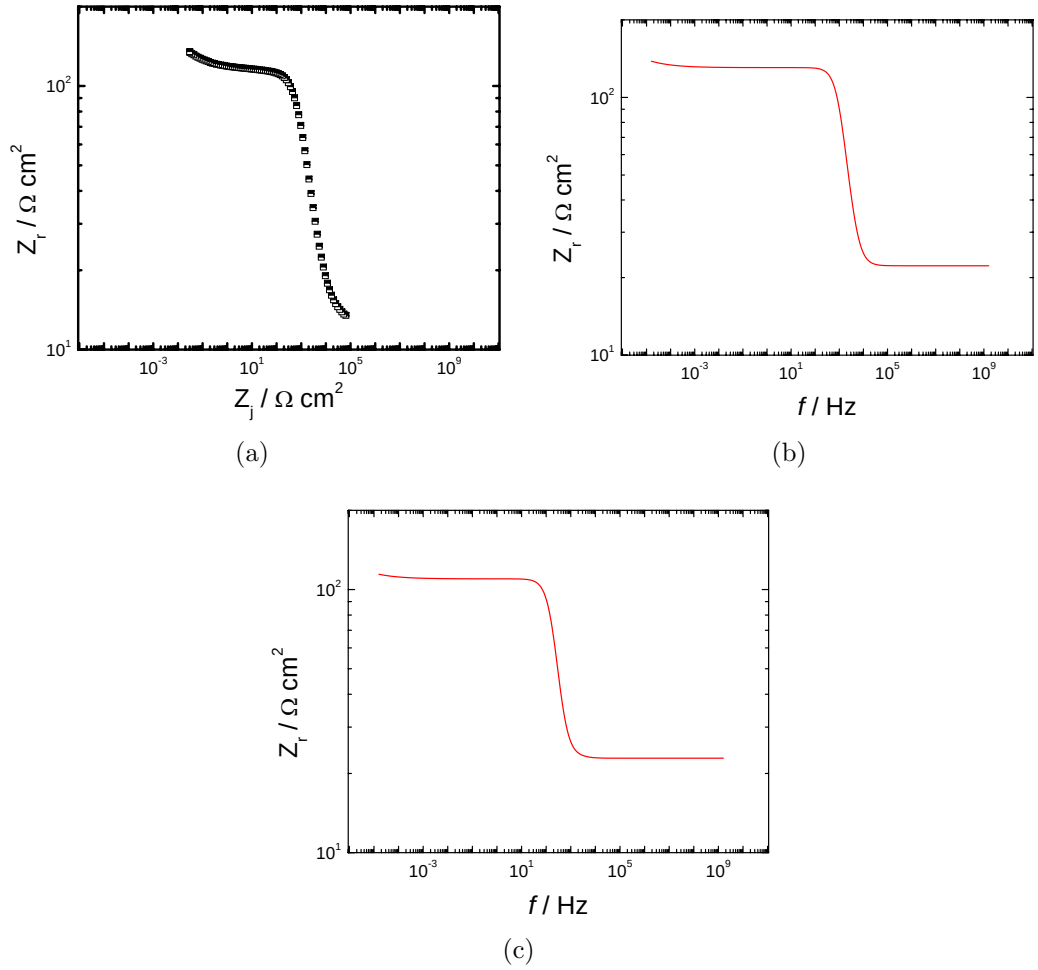

Figure 7–11: Imaginary representation of impedance data of a symmetric cell. (a) Experimental Result. (b) Model 1. (c) Model 2.

7.5 Conclusions

Two models were developed that are able to describe qualitatively the behavior observed in the experiments. The selection of the reactions mechanism used to developed those models was supported by independent observations. The impedance data and broken seals in the cells provided evidence of hydrogen evolution. Microscopic and Scanning Electron Microscope (SEM) micrographs provided evidence of the formation of solid films on the lithium surface. This is consistent with the formation of LiOH and LiO_2. Also, the micrographs showed that the film formed at perimeter of the cell which provides evidence of non-uniform current distribution.

Both models provided evidence that the distribution of time constants observed in the high-frequency capacitive loop is due to reactions at the lithium electrode. None of the modelled results allow for the identification of more than one capacitive time constants. It is necessary to account for the distributed reactivity evident in the experimental data. The distribution of RC time constants should be explored before a rigorous regression of the models is done.

CHAPTER 8
CONCLUSIONS

Electrochemical impedance spectroscopy experiments and models were used to facilitate an in-depth understanding of the physical processes that control symmetric lithium coin cells.

8.1 Experiments

Preliminary graphical analysis of the experiments performed on symmetric lithium coin cells provided useful guides to model development. Nyquist and Bode representations, as well as, IR-corrected Bode plots, log-log plots of the imaginary component of the impedance, and effective capacitance plot were used. The slopes in the log-log plots of the imaginary component of the impedance are directly related to the apparent constant-phase-element coefficient α. The difference in the slopes at intermediate and high frequencies demonstrated that more than one capacitive time constant can be identified in the system.

A decrease of the impedance response with time was observed. This is consistent with dissolution of native oxide layers on the lithium surface, as proposed in the literature. The results showed that the time required for complete dissolution of the oxide layers was on the order of several days.

A high-frequency capacitive loop was observed in all the experimetal results. This loop can be attributed to a dielectric behavior of the electrolyte or to reactions at the lithium metal surface. As the temperature of the cells was increased the impedance response decreased. This result is consistent with either hypothesis, that the high-frequency capacitive loop is due to reactions at the lithium metal surface or that the loop is due to a dielectric behavior of the electrolyte.

The impedance response of the symmetric stainless steel cells was consistent with a blocking electrode at low frequencies, and at high frequencies, the behavior was consistent with non-uniform current distribution. The high-frequency capacitive loop seen in the results of the symmetric lithium cell were not evident in the results from the cell with steel electrodes. Thus, the high-frequency capacitive loop seen in the impedance spectra of Chapter 5 is not associated with the dielectric response of the electrolyte. This loop must be described instead by a model that takes into account the reactions at the lithium electrode.

8.2 Model

Two models that take into account the physics and chemistry of the system and that are suitable for regression analysis were developed. Both models were able to qualitatively describe the behavior of observed in the experiments.

The selection of the reactions mechanism used to developed those models was supported by independent observations. The impedance data and broken seals in the cells provide evidence of hydrogen evolution. Microscopic and Scanning Electron Microscope (SEM) micrographs provided evidence of the formation of solid films on the lithium surface, this is consistent with the formation of LiOH and LiO_2. Also, the micrographs showed that the film formed at perimeter of the cell which is evidence of non-uniform current distribution.

Both models provided evidence that the distribution of time constants observed in the high-frequency capacitive loop is due to reactions at the lithium electrode. None of the modelled results allow for the identification of more than one capacitive time constants. It is necessary to account for the distributed reactivity evident in the experimental data. The distribution of RC time constants should be explored before a rigorous regression of the models is done.

REFERENCES

[1] A. Hjelm, T. Eriksson, and G. Lindbergh, "Electrochemical investigation of $LiMn_2O_4$ cathodes in gel electrolyte at various temperatures," *Electrochimica Acta*, vol. 48, pp. 171–179, 2002.

[2] Y. Kim and E. Smotkin, "The effect of plasticizers on transport and electrochemical properties of PEO-based electrolytes for lithium rechargeable batteries," *Solid State Ionics*, vol. 149, pp. 29–37, 2002.

[3] P. Georen and G. Lindbergh, "Characterization and modelling of transport properties in lithium battery polymer electrolyte," *Electrochimica Acta*, vol. 41, pp. 577–587, 2001.

[4] J.M. Tarascon, S. Grugeon, M. Morcrette, S. Laruelle, P. Rozier, and P. Poizot, "New concepts for the search of better electrode materials for rechargeable lithium batteries," *Comptes Rendus Chimie*, vol. 8, pp. 9–15, 2005.

[5] M. Doyle, J. Meyers, and J. Newman, "Computer simulations of the impedance response of lithium rechargeable batteries," *Journal of the Electrochemical Society*, vol. 147(1), pp. 99–110, 2000.

[6] W. Bennet and M. Manzo, *Preliminary evaluations of polymer-based lithium battery electrolytes under development for the polymer energy rechargeable systems program*, 1st International Energy Conversion Engineering Conference,Portsmouth,VA, 2003.

[7] A. Pereira Chagas, "The 200 years of the electric pile," *Quimica Nova*, vol. 23(3), pp. 427–429, 2000.

[8] F. Decker, "Volta and the pile," *Electrochemistry Encyclopedia*, 2005, University of Rome "La Sapienza".

[9] "Battery and fuel cell," *Britannica Student Encyclopedia. Encyclopedia Britannica Premium*, 2005, http://www.britannica.com/ebi/article-197279. Acessed October 23, 2005.

[10] G. Nazri and G. Pistoia, *Lithium Batteries: Science and Technology*, Kluwer Academic Publishers, Norwell, MA, 2004.

[11] P. Gomadam, J. Weidner, R. Dougal, and R. White, "Mathematical modelling of lithium-ion and nickel battery systems," *Journal of Power Sources*, vol. 110, pp. 267–284, 2002.

[12] K. Jung, S. Pyun, and J. Lee, "An investigation of lithium transport through vanadium pentoxide xerogel film electrode by analyses of current transient and AC-impedance spectra," *Electrochimica Acta*, vol. 49, pp. 4371–4378, 2004.

[13] D. Aurbach, B. Markovsky, A. Shechter, Y. Ein-Eli, and H. Cohen, "A comparative study of synthetic graphite and Li electrodes in electrolyte solutions based on ethylene carbonate-dimetyl carbonate mixtures," *Journal of Electrochemical Society*, vol. 143(12), pp. 3809–3820, 1996.

[14] T.S. Ong and H. Yang, "Symmetrical cell for electrochemical AC impedance studies of lithium intercalation into graphite," *Electrochemical and Solid States Letters*, vol. 4(7), pp. A89–A92, 2001.

[15] S. Zang and P. Shi, "Electrochemical impedance study of lithium intercalation into MCMB electrode in a gel electrolyte," *Electrochimical Acta*, vol. 49, pp. 1475–1482, 2004.

[16] M. Itagaki, N. Kobari, S. Yotsuda, K. Watanabe, S. Kinoshita, and M. Ue, "In situ electrochemical impedance spectroscopy to investigate negative electrode of lithium-ion rechargeable batteries," *Journal of Power Sources*, vol. 135, pp. 255–261, 2004.

[17] A. Hjelm and G. Lindbergh, "Experimental and theoretical analysis of $LiMn_2O_4$ cathodes for use in rechargeable lithium batteries by electrochemical impedance spectroscopy (EIS)," *Electrochimica Acta*, vol. 47, pp. 1747–1759, 2002.

[18] A. Lisowska-Oleksiak, "The interface between lithium and poly(ethylene-oxide)," *Solid State Ionics*, vol. 119, pp. 205–209, 1999.

[19] E. Peled, D. Golodnitsky, G.Ardel, and V. Eshkenazy, "The SEI model-application to lithium-polymer electrolyte batteries," *Solid State Ionics*, vol. 40(13), pp. 2197–2204, 1995.

[20] P. Novak, F. Joho, R. Imhof, J. Panitz, and O. Haas, "In situ investigation of the interactions between graphite and electrolyte solutions," *Journal of Power Sources*, vol. 81-82, pp. 212–216, 1999.

[21] D. Pletcher and F.C. Walsh, *Industrial Electrochemistry*, Chapman and Hall Ltd., London, 2nd edition, 1990.

[22] M. Broussely, Ph. Biensan, F. Bonhomme, Ph. Blanchard, S. Herreyre, K. Nechev, and R.J. Staniewicz, "Main aging mechanisms in Li ion batteries," *Journal of Power Sources*, vol. 146, pp. 90–96, 2005.

[23] W. Gorecki, M. Jeannin, E. Belorizky, C. Roux, and M. Armand, "Physical properties of solid polymer electrolyte PEO(LiTFSI) complexes," *Journal of Physics*, vol. 7, pp. 6823–6832, 1995.

[24] G.B. Appetechi, S. Scaccia, and S. Passerini, "Investigation on the stability of the lithium-polymer electrolyte interface," *Journal of The Electrochemical Society*, vol. 147(12), pp. 4448–4452, 2000.

[25] K. Murata, S. Izuchi, and Y. Yoshiba, "An overview of the research and development of solid polymer electrolyte batteries," *Electrochimica Acta*, vol. 45, pp. 1501–1508, 2000.

[26] P. Goeren and G. Lindbergh, "Characterization and modelling of the transport properties in lithium battery gel electrolytes. Part I: The binary electrolyte PC/$LiClO_4$," *Electrochimica Acta*, vol. 49, pp. 3497–3505, 2004.

[27] I. Rey, J.C. Lassegues, J. Grondin, and L. Servant, "Infrared and Raman study of the PEO-LiTFSI polymer electrolyte," *Electrochimica Acta*, vol. 43(10-11), pp. 1505–1510, 1998.

[28] F.S. Fiory, F. Croce, A. D'Epifanio, S. Licoccia, B. Scrosati, and E. Traversa, "PEO based polymer electrolyte lithium-ion battery," *Journal of European Ceramic Society*, vol. 24, pp. 1385–1387, 2004.

[29] C. Naudin, J.L. Bruneel, M. Chami, B. Besbat, J. Grondin, J.C. Lessegues, and L. Servant, "Characterization of lithium surface by infrared and raman spectroscopy," *Journal of Power Sources*, vol. 124, pp. 518–525, 2003.

[30] R. Potts and R. Guy, Eds., *Mechanisms of Transdermal Drug Delivery. Drugs and the Pharmaceutical Sciences*, Mercel Dekker, Inc, New York, NY, 1997.

[31] J.R. Macdonald, Ed., *Impedance Spectroscopy. Emphasizing Solid Materials and Systems*, John Wiley and Sons, Inc., Hoboken, NJ, 1987.

[32] C. Grabrielli, "Identification of electrochemical processes by frequency response analysis," Solartron instrumentation group monograph 004-83, The Solartron Electronic Group Ltd., Farnborough, UK, 1984.

[33] H. Shih and T. Lo, "Electrochemical impedance spectroscopy for battery research and developments," Tech. Rep., Solartron Analytical, Farnborough, UK, 1996.

[34] Z. Stoynov and D. Vladikova, *Differential Impedance Analysis*, Marin Drinov Academic Publishing House, Sofia, Bulgaria, 2005.

[35] C. Gabrielli, "Use and applications of electrochemical impedance techniques," Tech. Rep., The Solartron Electronic Group Ltd., Farnborough, UK, 1990.

[36] P. Agarwal, M.E. Orazem, and L. Garcia-Rubio, "Application of measurement models to impedance spectroscopy," *Journal of the Electrochemical Society*, vol. 142(12), pp. 4159–4168, 1995.

[37] P. Agarwal, M.E. Orazem, and L. Garcia-Rubio, "Application of the Kramers-Kronig relations in electrochemical impedance spectroscopy," *Electrochemical Impedance: Analysis and Interpretation, ASTM STP 1188*, pp. 115–139, 1993.

[38] M. Durbah, M.E. Orazem, and L. Garcia-Rubio, "Spectroscopy applications of the Kramers-Kronig transforms: Implications for the error structure identification," *Journal of the Electrochemical Society*, vol. 144(1), pp. 48–55, 1997.

[39] M.E. Orazem, P. Shukla, and M. Membrino, "Extension of the measurement model approach for deconvolution of underlying distributioins for impedance measurements," *Electrochimica Acta*, vol. 47, pp. 2027–2034, 2002.

[40] S. Carson, M.E. Orazem, O. Crisalle, and L. Garcia-Rubio, "On the error strucuture of impedance measurements. simulation of FRA intrumentation," *Journal of Electrochemical Society*, vol. 150(10), pp. E477–E490, 2003.

[41] M.E. Orazem, "A systematic approach toward error structure identification for impedance spectroscopy," *Journal of Electroanalytical Chemistry*, vol. 572, pp. 317–327, 2004.

[42] H. Young, *University Physics*, Addison-Wesley Publishing Company, Reading, MA, 8th edition, 1992.

[43] S. Boctor, *Electric Circuit Analysis*, Prentice Hall, Englewood Cliffs, NJ, 2nd edition, 1992.

[44] M.E. Orazem, N. Pebere, and B. Tribollet, "A new look at graphical representation of impedance data," Paper presented at the 206th meeting of the Electrochemical Society, Honolulu, Hawaii, October 3-8, 2004.

[45] B. Bennett, "Intercalation experiments with MCMB carbon in PEO-based electrolyte," NASA Internal Report-211990, Cleveland, OH, 2003.

[46] J. Newman, K. Thomas, H. Hafezi, and D. Wheeler, "Modelling of lithium-ion batteries," *Journal of Power Sources*, vol. 119-121, pp. 838–843, 2003.

[47] C. Schmidt and P. Skarstad, "Development of an equivalent-circuit model for the lithium/iodine battery," *Journal of Power Sources*, vol. 65, pp. 121–128, 1997.

[48] J. Thevenin and R. Muller, "Impedance of lithium electrode in propylene carbonate electrolyte," *Journal of The Electrochemical Society*, vol. 134, pp. 273–280, 1987.

[49] M. Doyle, T. Fuller, and J. Newman, "The importance of the transference number in lithium/polymer cell," *Electrochimica Acta*, vol. 39, pp. 2073–2081, 1994.

[50] R. Spotnitz and J. Franklin, "Abuse behavior of high-power, lithium-ion cells," *Journal of Power Sources*, vol. 113, pp. 81–100, 2003.

[51] D. Aurbach, Y. Talyosef, B. Markovsky, E. Markevich, E. Zinigrad, L. Asraf, J. Gnanaraj, and H. Kim, "Design of electrolyte solutions of Li and Li-ion batteries: A review," *Electrochimica Acta*, vol. 50, pp. 247–254, 2004.

[52] P. Ramadass, B. Haran, R. White, and B. Popov, "Mathematical modelling of capacity fade of Li-ion cells," *Journal of Power Sources*, vol. 123, pp. 230–240, 2003.

[53] P. Nelson, I. Bloom, K. Amine, and G. Henriksen, "Design modelling of lithium-ion battery performance," *Journal of Power Sources*, vol. 110, pp. 237–244, 2002.

[54] B. Markovsky, A. Rodkin, Y. Cohen, O. Palchik, E. Levi, D. Aurbach, H. Kim, and M. Schmidt, "The study of the capacity fading process of Li-ion batteries: Major factors that play a role," *Journal of Power Sources*, vol. 119-121, pp. 504–510, 2003.

[55] B. Dixon and R. Morris, "Computational chemistry: Design and experimental verification of pre-designed heeropolymer electrolytes for rechargeable lithium batteries," *Journal of Power Sources*, vol. 119-121, pp. 856–858, 2003.

[56] A. Crespi, C. Schmidt, J. Norton, K. Chen, and P. Skarstad, "Modelling and characterization of the resistance of lithium/SVO batteries for implantable cardioverter defibrillators," *Journal of The Electrochemical Society*, vol. 148(1), pp. A30–A37, 2001.

[57] S. Buller, M. Thele, E. Karden, and R. De Doncker, "Impedance-based non-linear dynamic battery modelling for automotive applications," *Journal of Power Sources*, vol. 113, pp. 422–430, 2003.

[58] A. Salkind, P. Singh, A. Cannone, T. Atwater, X. Wang, and D. Reisner, "Impedance modelling of intermediate size lead-acid batteries," *Journal of Power Sources*, vol. 116, pp. 174–184, 2003.

[59] P. Notten, O. Ouwerkerk, A. Ledovskikh, H. Senoh, and C. Iwakura, "Hydride forming electrode materials seen from a kinetic perspective," *Journal of Alloys and Compounds*, vol. 356-357, pp. 759–763, 2003.

[60] E. Deiss, F. Holzer, and O. Hass, "Modelling of an electrically rechargeable alkaline Zn-Air battery," *Electrochimica Acta*, vol. 47, pp. 3995–4010, 2002.

[61] A. Ledovskikh, E. Verbitskiy, A. Ayeb, and P. Notten, "Modelling of rechargeable NiMH batteries," *Journal of Alloys and Compounds*, vol. 356-357, pp. 742–745, 2003.

[62] R. Marsh, S. Vukson, S. Surampudi, B. Ratnakumar, M. Smart, M. Manzo, and P. Dalton, "Li-ion batteries for aerospace applications," *Journal of Power Sources*, vol. 98, pp. 25–27, 2002.

[63] R. Bouchet, S. Lascaud, and M. Rosso, "An EIS study of the anode Li/PEO-LiTFSI of a Li polymer battery," *Journal of the Electrochemical Society*, vol. 150(10), pp. A1385–A1389, 2003.

[64] M.E. Orazem, "A systematic approach toward error structure identification for impedance spectroscopy," *Journal of Electroanalytical Chemistry*, vol. 572, pp. 317–327, 2004.

[65] M.E. Orazem, "Interpretation of impedance spectroscopy," Manuscript in preparation. Draft November 2005.

[66] M.E. Orazem, *User Manual for the Measurement Model Toolbox for Impedance Spectroscopy*, University of Florida, Chemical Engineering Department, Electrochemistry Laboratory, Gainesville, FL, 2000.

[67] V.M. Huang, V. Vivier, M.E. Orazem, N. Pebere, and B. Tribollet, "The impedance response of a blocking electrode with local CPE behavior," Manuscript in preparation. Draft April 2006.

[68] D. Aurbach, "Review of selected electrode-solution interactions which determine the performance of Li and Li-ion batteries," *Journal of Power Sources*, vol. 89, pp. 206–218, 2000.

[69] P. Arora, R.E. White, and M. Doyle, "Capacity fade mechanisms and side reactions in lithium-ion batteries," *Journal of the Electrochemical Society*, vol. 145, pp. 3647–3667, 1998.

[70] I. Rey, C. Lessegues, P. Baundry, and H. Majastre, "Study of a lithium battery by confocal Raman microspectrometry," *Electrochimica Acta*, vol. 43(10-11), pp. 1539–1544, 1998.

BIOGRAPHICAL SKETCH

Nelliann Perez-Garcia received the Bachelor of Science degree in chemical engineering from the University of Puerto Rico, Mayaguez Campus in May 1999. She began her graduate studies at the University of Florida in August 1999. In the year 2000 she joined Professor Mark E. Orazem's electrochemical engineering research group to pursue a Master of Science degree. Upon completion of the degree requirements in May 2003, Nelliann continued her graduate studies to pursue a Doctor of Philosophy degree. In January 2006 Nelliann began working for Lockwood Greene in Atlanta, Georgia, where she plans to continue her development as a chemical engineer.